# ABSTRACT

Title of dissertation: PRESSURE TUNING THE TOPOLOGY OF QUANTUM MATERIALS

I-Lin Liu
Doctor of Philosophy, 2019

Dissertation directed by: Professor Johnpierre Paglione
Chemical Physics Program

Topological materials have attracted great interest in condensed matter physics because of their potential applications for topological quantum computing. Transition metal dichalcogenides are very promising topological materials due to their novel topological properties. $T_d$-$MoTe_2$ has been highlighted as potential topological superconductor and type-II Weyl semimetal with Fermi arcs and Weyl nodes through density functional theory and angle-resolved photoemission spectroscopy studies. Recently, T'-$MoTe_2$ was proposed to support a higher-order topology via first principle calculations. Pressure plays a significant role in fine tuning the ground state between noncentrosymmetric $T_d$-$MoTe_2$ and T'-$MoTe_2$ preserved lattice inversion symmetry. The corresponding topology of their Fermi surfaces are thus associated with the structural transition, superconducting, and the band structure between T'-$MoTe_2$ and $T_d$-$MoTe_2$ under pressure.

This dissertation presents an experimental study of Shubnikov-de Haas oscillations, neutron scattering and first-principles calculations, demonstrating how

pressure tunes the band structure, superconducting transition temperature and the first-order structural transition in $MoTe_2$. Although results from angle-resolved photoemission spectroscopy and density functional theory have previously caused controversy, this work confirms the presence of nontrivial topology of higher-order topology in T'-$MoTe_2$ via the experimental determination of a nontrivial Berry's phase. Moreover, we discover a novel phase of topological matter, deemed a Topological Interface Network (TIN) that forms from a natural heterostructure of mixed $T_d$ and T' structural phases. This new electron structure exists at the interfaces between the domains of two topological structures. Such a novel state with superconductivity and its transition between breaking and conservation of lattice inversion symmetry raises the possibility of quantum phase transitions between different types of topological superconductors. This natural microstructure can be potentially useful in topological quantum computing.

# Pressure Tuning the Topology of Quantum Materials

by

I-Lin Liu

Dissertation submitted to the Faculty of the Graduate School of the
University of Maryland, College Park in partial fulfillment
of the requirements for the degree of
Doctor of Philosophy
2019

Advisory Committee:
Professor Johnpierre Paglione, Chair/Co-Advisor
Professor Nicholas P. Butch, Advisor
Professor Steven Anlage
Professor Efrain E. Rodriguez
Professor Ichiro Takeuchi

# Acknowledgments

First of all, I would like to express my sincere gratitude to my supervisor, Professor Nick Butch for giving me an opportunity to work on challenging and interesting projects. He is helpful and supportive of research discussion and shares his successful experiences and skills. It has been a pleasure to work with him.

I am grateful to my respected co-advisor, Professor Johnpierre Paglione. He encourages me thinking independently. He runs our group well, therefore, everyone helps and supports each other. Thanks are due to Professor Steven Anlage, Professor Efrain E. Rodriguez and Professor Ichiro Takeuchi for agreeing to serve on my thesis committee and for sparing their invaluable time reviewing the manuscript.

I would like to thank Professor Yasuyuki Nakajima. While he was a postdoc at UMD, he shared his best knowledge of pressure measurements and guided me through the world of topological materials. I really enjoyed discussing with him and discovered some ideas to solve difficulties in research. I appreciate Dr. Sheng Ran for his practical suggestions and ideas. He brings great joy to discover the reentrant SC, $UTe_2$, its novelties of $H_{c2}$ and $T_c$.

My group members have enriched my graduate life in many ways and deserve a special mention. Chris Eckberg machined stainless steel to build pressure tools and is helpful and patient to measurements. Daniel Campbell not only shares his broad opinions but also makes joyful conversations with everyone. Connor Roncaioli and RenXiong Wang always support me and listen to me. Trstin Metz is responsible for all cooperation. I never need to worry whether he might miss any detail. I really

appreciate all of your helps and company for the wonderful and happy time.

I would also like to acknowledge help and support from the staff members at NCNR. Colin Heikes, William D. Ratcliff, and Taner Yildirim share your ideas and discuss all possibilities of our study. Our weekly meeting trained me to well prepare every time and to absorb diverse and creative ideas. You opened a new door of topological materials to me and gave me a great chance working on a very interesting project.

My special thanks to Professor John Singleton, Dr. Neil Harrison, Dr. Marcelo Jaime and Dr. Fedor Balakirev. I am totally convinced by your passion to science and perpetual curiosities of physics. Your abundant knowledge and experiences keep our research move forward.

It is impossible to remember all, and I apologize to those I've inadvertently left out.

Lastly, thank you all!

# Foreword

In the course of my dissertation work, I have contributed to the following works, either published or currently under review. The results presented in this dissertation are published in *Phys. Rev. B* and *arXiv*, which are marked with asterisks in the list below:

1. * I-Lin Liu, *et al.*, 'Quantum oscillations from networked topological interfaces in a Weyl semimetal' arXiv:1905.02277 (2019).
2. Sheng Ran, I-Lin Liu, *et al.*, 'Extreme magnetic field-boosted superconductivity' arXiv:1905.06901 (2019). **Under review of** *NaturePhysics*.
3. Y. Nakajima, *et al.*, 'Planckian dissipation and scale invariance in a quantum-critical disordered pnictide', arXiv:1902.01034 (2019). **Under review of** *Science*.
4. Sheng Ran, *et al.*, 'Spontaneously Polarized Half-Gapped Superconductivity' arXiv:1811.11808 (2019), **Accepted by** *Science*.
5. J. G. Rau, L. S. Wu, *et al.*, 'Physical behavior of the breathing pyrochlore lattice $Ba_3Yb^2Zn_5O^{11}$ under applied magnetic fields 'Journal of Physics: Condensed Matter **30**, 455801 (2018).
6. Colin Heikes, I-Lin Liu, *et al.*, 'Mechanical control of crystal symmetry and superconductivity in Weyl semimetal $MoTe_2$' *Phys. Rev. Material* **2**, 074202 (2018).
7. Kefeng Wang, *et al.*, 'Dirac dispersion and non-trivial Berry's phase in three-dimensional semimetal $RhSb_3$.' arXiv:1703.04673 (2017).
8. * I-Lin Liu, *et al.*, "Pressure Tuning of Collapse of Helimagnetic Structure in $Au_2Mn$." *Phys. Rev. B* (2017).
9. R. L. Stillwell, I-Lin Liu, *et al.*, 'The Tricritical Point of the f-electron Antiferromagnet $USb_2$ Driven by High Magnetic Fields.' *Phys. Rev. B* **95**, 014414 (2017).

# Table of Contents

# List of Tables

# List of Figures

# List of Abbreviations

| | |
|---|---|
| AHE | Anomalous Hall effect |
| ARPES | Angle-Resolved Photoemission Spectroscopy |
| C | conical |
| DM | Dzyaloshinskii-Moriya |
| DSM | Dirac semimetals |
| FAN | fan-type structure |
| FFT | Fast Fourier Transform |
| FM | ferromagnetism |
| H | helical |
| $H_c$ | critical field |
| $H_{c2}$ | upper critical field |
| LSW | longitudinal spin wave |
| MCMC | Markov chain Monte Carlo |
| MR | magnetoresistance |
| OHE | ordinary Hall effect |
| SdH | Shubnikov de Haas |
| SOC | spin orbital coupling |
| SS | spiral spin |
| TI | topological insulator |
| TIN | topological interface network |
| TMDC | transition-metal dichalcogenide |
| TSW | transverse spin wave |
| WSM | Weyl semimetals |

# Chapter 1: Introduction

## 1.1 Topological materials

Modern physics is built upon the fruitful connections between low-energy condensed matter physics and high-energy particle physics [1]. The discoveries of massless fermions in graphene and the surface state of the topological insulator (TI) have led to several novel studies in Dirac fermions and the Dirac equation [2–4]. The Dirac equation in crystals, derived from Paul Dirac in 1928, describes the quantum mechanics of the electrons, suggesting three distinct particles: Dirac fermions, Weyl fermions, and Majorana fermions. The Weyl equation, proposed by Hermann Weyl in 1929, is based on the Dirac equation and associated with the massless fermion of chirality, known as Weyl fermions [4]. Weyl's equation is a relatively simple model of elementary particles, but no appropriate candidate had been found in high-energy physics experiments. In the last five years, Weyl fermions have been discovered in topological quantum materials with strong Spin-Orbit Coupling (SOC) that exists chiral anomalies in negative magnetoresistance (MR), Anomalous Hall Effect (AHE), Fermi arcs and Weyl nodes.

This has attracted great interests in topological materials such as Dirac semimetals (DSM), TI and Weyl semimetals (WSM) not only because of its novel nontrivial

physics properties but also their potential applications in topological quantum computers. One of the main problems for a quantum computer is the simulation of quantum systems [5]. It could be exponentially faster to consider some complicated questions on a quantum computer than a classical computer, such as many-body system, quantum Hamiltonian problems, or high temperature superconductivity. As another example, with exponentially larger Hilbert space, a quantum computer enables the solutions of lattice gauge theory and strongly interacting nuclear systems. However, the most difficult obstacle to build a functioning and reliable quantum computer is the systematic errors that accumulate from integrated quantum or classical computation. As a result, sufficiently fault tolerant and effective implementation of error corrections become critical [7]. Additionally, random systematic errors occur by those interactions between a quantum computer and environment. This error correction process itself could be noisy or cause more errors. Presently, such a threshold of the error corrections is below $10^4 \sim 10^6$ times to perform perfectly quantum calculations [6]. The birth of TI and topological superconductors come one step closer to some applications of topological quantum computer. Topological superconductors are predicted to host exotic Majorana states that obey non-Abelian statistics and can be used to implement a topological quantum computer [9]. Most of the proposed topological superconductors are realized in difficult-to-fabricate heterostructures at low temperature.

The topology of a TI originates from its inverted band structure, the SOC opens a full gap and band inversion results in the metallic surface state. The bulk states are insulating and its surface state is metallic on the surface in figure 1.1(b).

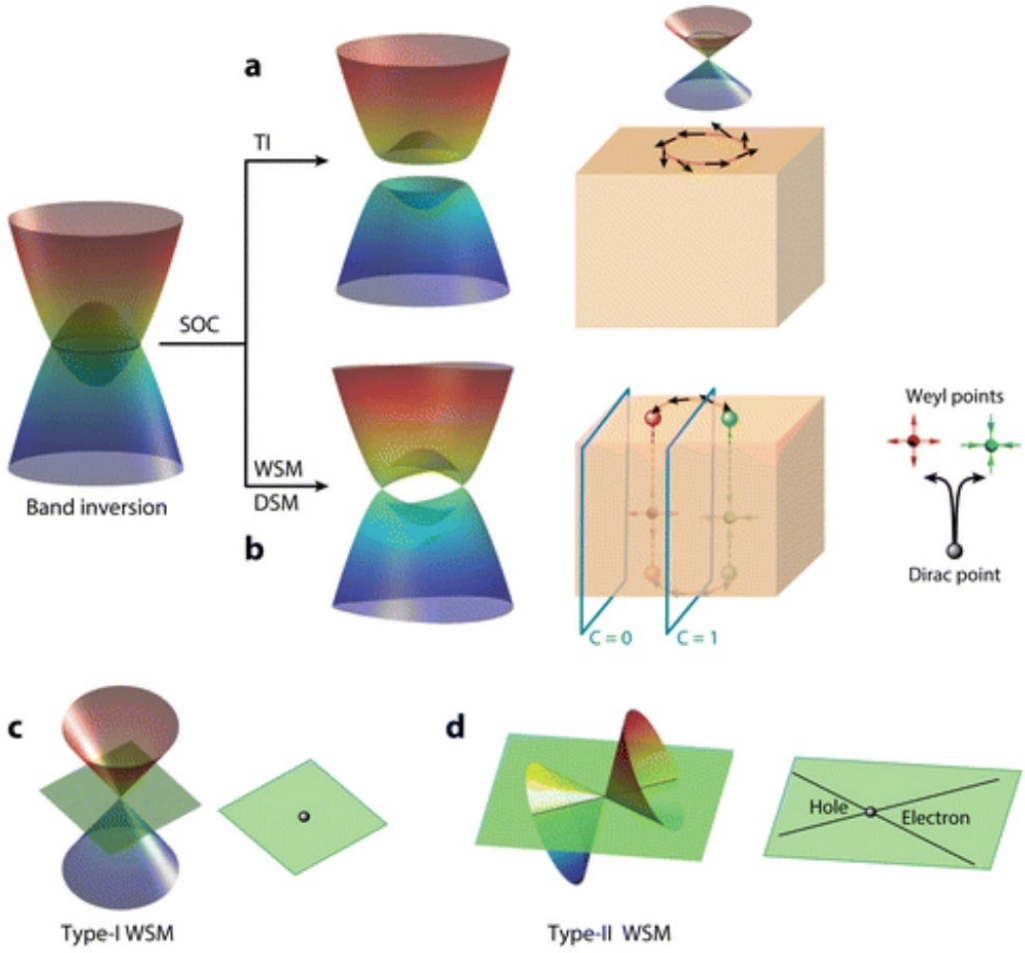


Figure 1.1: The Fermi surface of (a) Topological insulator with chiral symmetry, (b) DSM with Dirac point and WSM with pairs of Weyl nodes. (c) The point-like Fermi surface of type-I WSM and (d) tilted Fermi surface with touching point of electron and hole pockets. Adapted from [10–12].

Both DSM and WSM have similar origins of the inverted band structure and their bulk bands are gapped out by the SOC in 3D momentum space except at some isolating linearly crossing points, namely Dirac points/ Weyl points (Weyl nodes) [2,10], as a 3D analog of graphene. For WSM, this pair of Weyl nodes are like a sink and source of Fermi surface and its surface state appears as Fermi arcs between this pair of Weyl nodes. In a DSM, all bands are doubly degenerated, whereas in a WSM its band degeneracy is lifted due to the breaking of lattice inversion symmetry or time-reversal symmetry or both [27]. This dissertation will focus on two topics: (I) helimagnets, and (II) topological semimetals, and will concentrate on Spiral Spin (SS) materials, $Au_2Mn$ and type-II WSM candidate, $MoTe_2$.

## 1.2 Introduction to Helimagnets

Helimagnets have become popular materials to study spin textures such as skyrmions as well as antiskyrmions. Tuning SOC and the Dzyaloshinskii-Moriya interaction (DMI) [40,41] typically changes the helimanetic phases in a critical field ($H_c$), chemical composition and pressure. Topological properties ( e.g. stability of spin texture and the electronic control of skyrmion by varying bias voltage and current) have motivated researchers to further design novel applications. The helimagnetic phase diagrams in temperature and chemical composition share a similar pattern, with the SS/ helix phase at low magnetic field, distorted spiral magnetic structure in an intermediate magnetic field, and ferromagnetic phase at a higher magnetic field above some critical threshold. Spin-orbit interaction plays an impor-

tant role in the origin of novel magnetic states and phenomena such as giant MR, TIs, and skyrmions. By studying helimagnets as a function of tuning by magnetic field and pressure, we gain insight of the spin textures.

There are several kinds of modulated magnetic structures. Longitudinal spin wave (LSW) and transverse spin wave (TSW) structures were discovered in other materials [60, 62]. Figure 1.2 illustrates the basic types of long-periodic modulated structures, including the following: SS, Conical spin (C), Helical spin (H), LSW, TSW and fan-type structure (FAN) structures. In the SS structure, those arrows in the $xy$ plane indicate their orientations of the net magnetic moments (spins) of each plane, and their relative spin angle, the fixed phase difference between two neighboring planes, is always a constant. In particular, FAN is only induced in SS and distorted C with a magnetic field applied perpendicular to the $z$ axis. With a magnetic field parallel to $xy$ plane, FAN appears as its spins only distribute in a small fan area, and the corresponding spin angles depend on the relative strength of exchange coupling and magnetic field. This combination of a constant $z$ direction component of spin and SS in the $xy$ plane forms a C; the rotating spin plane tilts by a small angle with respect to the $z$-axis in H. Net spin moments in each layer only point in the longitudinal or transverse directions with periodic amplitudes in LSW and TSW magnetic structures.

The SS structure is a kind of magnetic superlattice with ferromagnetically coupled planes and net spins rotating in $xy$ plane. Its constant spiral spin angle indicates the offset angle between neighboring planes. The SS structure evenly spaces ferromagnetic layers with weaker, variable interlayer coupling. The exchange

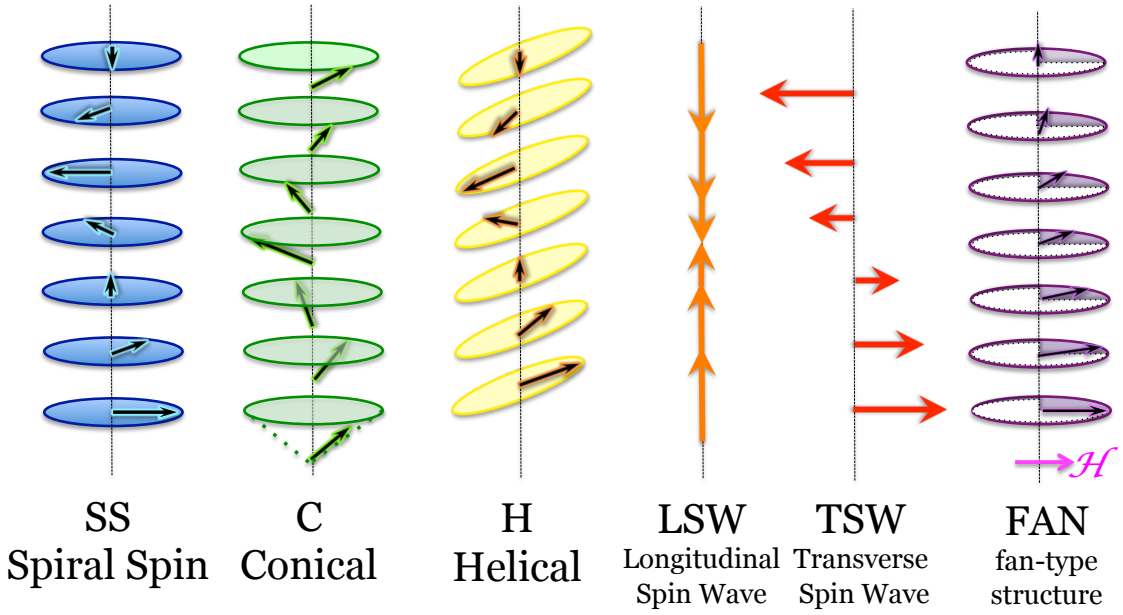


Figure 1.2: Typical modulated magnetic structures of crystals [60, 62].

coupling constant within each layer is $J_0$, between the first neighboring layer is $J_1$, between the second nearest neighboring layer is $J_2$, and so on. The net spin in the $n^{th}$ layer is oriented to a specific angle $\theta_n$ in $xy$ plane, and n, the number of layers, can approach infinity. The interaction energy can be expressed as

$$E = -S^2 \sum_n [J_0 + 2J_1 \cos(\theta_{n+1} - \theta_n) + 2J_2 \cos(\theta_{n+2} - \theta_n) + \cdots]. \tag{1.1}$$

One trivial solution to minimize interaction energy is given by $\theta_{n+1} - \theta_n = \phi$, where $\phi$ is the spin angle between first neighboring layers. Namely, we assumed that the interactions between each nearest neighboring layers and their corresponding spin angle $\phi$ between two nearest layers in the system are equivalent. Thus, we could simplify the energy as,

$$\begin{aligned} E &= -NS^2 J(\phi); \\ where \quad J(\phi) &= [J_0 + 2J_1 \cos\phi + 2J_2 \cos(2\phi) + \cdots]. \end{aligned} \tag{1.2}$$

These two special cases for spin structure, ferromagnetism (FM) and antiferromagnetism, occur when the $\phi$ is 0 or $\pi$, when all spins in their neighboring layers are parallel or antiparallel, respectively.

The helimagnetic phase diagrams in temperature and chemical composition share a similar pattern: SS/ helix phase at low field, conical; distorted spiral magnetic structure in intermediate field region; and ferromagnetic phase at higher field above the corresponding $H_c$. Spin-orbit interaction plays an important role in origin or emergence of novel magnetic states and phenomenon in giant MR materials, TI, and skyrmion. Skyrmion lattice is usually right below Neel temperature and $H_c$. Due to the skyrmion-spin structure, the related Topological Hall effect (THE) [42–45] explained well the large variances of Hall coefficient. Fine tuning the helimagnetic phase would possibly produce a skyrmion material.

$Au_2Mn$ was well known for its magnetic spiral structure [48]. These modulated magnetic models of $Au_2Mn$ have been discussed as the origin of helimagnets; their related modulated magnetic structures include ferromagnetic exchange energy, DM interaction, quadruple spin-spin coupling and spin angle $\phi$ of the in-plan net spin between neighboring layers [49,51]. The in-plane local ferromagnetic moment of Mn is 3.5 $\mu_B$ and spirals along the c-axis of the tetragonal lattice [49,50]. These conflicted reports in neutron diffraction motivate us to confirm whether the minimum of the spin angle, 47°, locates at 120 K or if its propagation vector maintains the constant value with spin angle, 45°, below 120 K [55]. Based on the pressure dependence of magnetization, the critical pressure ($P_c$) from spiral spin to ferromagnetism (SS-FM) transition is predicted to be above 20 kbar [57]. Building the SS-FM phase bound-

ary and critical pressure in temperature and pressure plane would allow us probe the variations of spin texture and competition of ferromagnetic exchange interaction and spin-orbit interaction.

We present measurements of the temperature and pressure dependence of the helical spin angle, and the pressure dependence of the $H_c$ of the SS-FM transition through magnetization and MR measurements. Pressure drives $Au_2Mn$ through a second-order phase transition, which agrees with recent band structure calculations using DFT within the Local Spin Density Approximation (LSDA) [52,53]. An anomalous magnetic peak in positive MR at low temperature and steplike magnetization tracks the SS-FM transition, and interestingly, in the pressure-induced FM phase, we did not see evidence of the expected AHE [46,47].

## 1.3 Anomalous Hall effect in intrinsic magnetic transition

The AHE is a quantum phenomenon, which originates from a quantum coherent band tuned by external electric field and the disorder potential. Weak localization is not well explained using traditional semiclassical Boltzmann transport theory. There are three distinct factors of AHE: intrinsic, skew scattering, and side-jump contributions. The intrinsic contribution is dependent only on the band structure of a perfect crystal and captured by the induced interband coherence from the anomalous velocity in the momentum-space Berry's phase related contribution. In many materials with strong SOC, the intrinsic contribution dominates the AHE. The skew scattering is due to the chiral features which obviously appear in the dis-

order scattering of ferromagnets and are proportional to the Bloch state transport lifetime. The Hall resistivity $\rho_H$ includes two components,

$$\rho_H = R_0 H + R_1 M(T, H). \tag{1.3}$$

Here, M(T,H) is the magnetization and $R_0$ and $R_1$ are defined as the ordinary and anomalous Hall coefficients [31]. The high conductivity region, good metal region, bad metal/hopping region are determined by the conductivity ( $\sigma_{xx}$) and the relationship between $\sigma_{xy}^{AH}$ and $\sigma_{xx}$. The Hall conductivity in the high purity region, $\sigma_{xx} > 0.5 \times 10^6\ (\Omega cm)^{-1}$ [32], is dominated by $\sigma_{xy}^{AH-skew} \sim \sigma_{xx}^1$. This region is very challenging for experimental study because it requires a large magnetic field for saturated magnetization $M$ to overcome the very large ordinary Hall effect (OHE). The coefficients of OHE and AHE, $R_0$ and $R_s$ tend to be the same order of magnitude [34]. Moreover, the $\sigma_{xy}^{skew}$ is proportional to linear scattering time $\tau$; the OHE one increases with nonlinear scattering time as $\tau^2$. Therefore, OHE dominates the whole Hall effect, so the AHE current might be unsolvable from OHE one. For the good metal region, $\sigma_{xx} \sim 10^4 - 10^6\ (\Omega cm)^{-1}$ and the Hall conductivity is not sensitive to the longitudinal conductivity. This implies that the intrinsic and side-jump, scattering independent mechanisms dominate. In the bad metal region, $\sigma_{xx} < 10^4\ (\Omega cm)^{-1}$, anomalous Hall conductivity decreases with decreasing longitudinal conductivity at a rate faster than linear [32, 33].

## 1.4 Weyl semimetals

The Weyl equation, published by Hermann Weyl in 1929, provides a model of elementary massless fermions of chirality in the Dirac equation. In high-energy particle physics, only neutrinos were present the possible chirality but found to be massive. Weyl fermions in WSM with linearly disperse bands and Weyl node terms were discovered within the last five years [4]. The physicist Conyers Herring considered that the electronic states without any particular symmetry have the same energy and crystal momentum. The Weyl equation describes that accidental touching points in band structure, referred as Wyel nodes in novel topological materials [2, 10]. The quantum mechanical wave function of the Weyl fermions acquires Berry's phase, geometric phase for the close loop in momentum space. The Berry's phase represents the magnetic monopoles in the real space associated with the source or sink of magnetic flux. The Weyl nodes in real space are related to chiral fermions and behave like the magnetic monopoles in momentum space. The Weyl fermions have been found in WSMs in terms of Fermi arcs and Weyl nodes corresponding the touching points in band structure by means of ab-initio calculation and Angle-Resolved Photoeemission Spectroscopy (ARPES) [2].

WSM exists in either breaking of time reversal or breaking of lattice inversion symmetry systems. The magnetic induced WSM has been found in half-Heusler GdPtBi, which has been verified as a WSM with breaking of time reversal symmetry [13]. The discovery of Weyl nodes and Fermi arcs in inversion-breaking single-crystal non-magnetic materials TaAs has been found as a WSM with the breaking

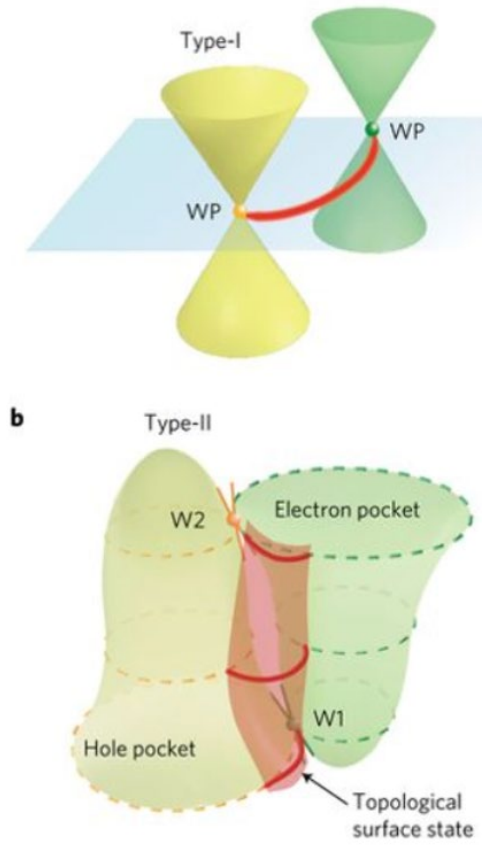


Figure 1.3: (a) Dispersion for type-I Weyl fermions near $E_F$. The Weyl points are labelled by yellow and green dots. (b) Type-II WSM with electron and hole pockets touching at two different energies. Adapted from [10–12].

of lattice inversion symmetry exists [14]. The WSM can be classified into type-I, which respects Lorentz symmetry, and type-II, which does not. Recently the layered transition-metal dichalcogenides (TMDC) $MoTe_2$ was predicted as the material candidate of type-II WSM [10] as shown in figure 1.3. Soon after these predictions, $MoTe_2$ has been verified as the first type-II WSM by ARPES experiments from several independent groups. In a type-I WSM, the Fermi surface shrinks to zero at the Weyl points as double Dirac cones when the Fermi energy is sufficiently close to the Weyl points. On another hand, due to the strong tilting of the Weyl cone in type-II WSM, these Weyl points locate at the touching points between electron and hole pockets in Fermi surface [10]. $WTe_2$ and $T_d$-$MoTe_2$ were proposed as type-II WSM and ARPES also showed their Weyl nodes and Fermi arcs, unlike some point-like Fermi surfaces in DSM and type-I WSM.

### 1.4.1 Degeneracy and chirality in Weyl semimetals

In WSM, these Weyl nodes are stable under the small perturbations and maintain the band degeneracy. This double degeneracy of the bands holds if symmetry operator $\tilde{\mathcal{T}} = \mathcal{T}\mathcal{P} = -1$, the multiple of the time reversal symmetry $\mathcal{T}$ and inversion symmetry $\mathcal{P}$, equals negative one. The Kramer degenerate ($\mathbf{k} \equiv -\mathbf{k}$) only shows at the time reversal invariant and breaking of crystal inversion symmetry. Generally, if only inversion symmetry is preserved, these bands usually are nondegenerate. We can expand the effective Hamiltonian of such nondegenerate bands as

$$H(\mathbf{k}) = f_0(\mathbf{k})\mathbb{1} + f_1(\mathbf{k})\sigma_x + f_2(\mathbf{k})\sigma_y + f_3(\mathbf{k})\sigma_z. \tag{1.4}$$

Here, $f_1, f_2$, and $f_3$ are the coefficients of the Pauli metrix along $x$, $y$ and $z$ in momentum spaces. While $f_1 = f_2 = f_3 = 0$, we could expect the touching points, Weyl nodes, without any specific tuning. The Weyl nodes cannot be removed by the small variations and will only vanish by the annihilation with the paired Weyl nodes. The natural Weyl nodes are usually close to the Fermi energy, so we could expect that $f_0(\mathbf{k})$ is close to zero. Therefore, Hamiltonian at $\mathbf{k} = \delta\mathbf{k} + \mathbf{k_0}$ becomes

$$H(\mathbf{k}) \sim f_0(\mathbf{k_0})\mathbb{1} + \mathbf{v_0} \cdot \delta\mathbf{k}\mathbb{1} + \sum_{a=x,y,z} \mathbf{v_a} \cdot \delta\mathbf{k}\sigma^a, \tag{1.5}$$

where $\mathbf{v}_\mu = \nabla_k f_\mu(\mathbf{k}|_{\mathbf{k}=\mathbf{k}_0})$ are the effective velocities which exist in the absence of additional symmetries.

The net chirality of Weyl nodes must be zero, which refers to the fact that the net Berry flux integrated Berry field $\mathcal{B}$ over all Brillouin zone must vanish. The Berry flux of the surface enclosing the point $\mathbf{k}_0$ is exactly $2\pi C$, where $C$ ( $C = sign(\mathbf{v}_x \cdot \mathbf{v}_y \times \mathbf{v}_z)$) is the chirality. The Weyl points behave as singularities in Berry curvature where Weyl points act as monopoles in the momentum space with a fixed chirality: Such a Weyl point can be a source (C = 1) or a sink ( C = −1) of its Berry curvature. These Weyl points always appear in pairs [16, 17]; otherwise, the Berry flux becomes divergent. The WSM requires the breaking of either the time-reversal symmetry or the lattice inversion symmetry. The integral of the band touching with $C = \pm 2$ corresponds to the double Weyl nodes, however, the integral of whole Weyl nodes in volume, the net Berry flux must vanish as

$$\sum_i \int_{\partial V_i} \mathcal{B}(\mathbf{k}) \cdot \delta S_k = -2\pi \sum_i C_i = 0. \tag{1.6}$$

### 1.4.2 Paring symmetry in Weyl semimetals

The Weyl nodes could be preserved either breaking of time reversal invariant or inversion symmetry. One scenario is that WSM preserves inversion symmetry, breaks time reversal symmetry and allows the minimal numbers of Weyl nodes, only two with the opposite chirality. Magnetic WSM has been expected as a good case that WSM breaks time reversal invariant $\mathcal{T}$. The magnetically ordered pyrocholres, $Eu_2Ir_2O_7$ and $Nd_2Ir_2O_7$ become insulating at low temperature and quadratic doubly degenerate bands, Weyl nodes, are predicted in the metallic phase above the magnetic ordering temperature [18–20]. $Pr_2Ir_2O_7$ has been found to have band touchings and stays at nonmagnetic metallic state at low temperature [21–23]. Particularly, $Mn_3Ge$ and $Mn_3Sn$, antiferromagnetisms with noncollinear spin order [24, 25] have a large anomalous Hall conductivity [26]. They are predicted as WSM with several Weyl nodes and trivial bands near Fermi level. The stronger SOC in $Mn_3Sn$ might lead the fewer Weyl nodes and the more annihilation of Weyl points [26].

On the other hand, Weyl nodes are allowed to break the lattice symmetry and to preserve the time reversal invariance. Those Weyl nodes locate at $\mathbf{k_0}$ and $-\mathbf{k_0}$ under time reversal symmetry, there must be another pair of Weyl nodes with opposite chirality to cancel the net charility. In this case, the total number of Weyl nodes must be the multiple of four. In conventional type-I WSM, Weyl nodes locate slightly below and above the Fermi surface. In type-II WSM, the Weyl cone with larger tilt angle from Fermi level [10] supports the surface Fermi arcs, which are the signatures of the type-II WSM sates. Band structure of TaAs has two mirror planes

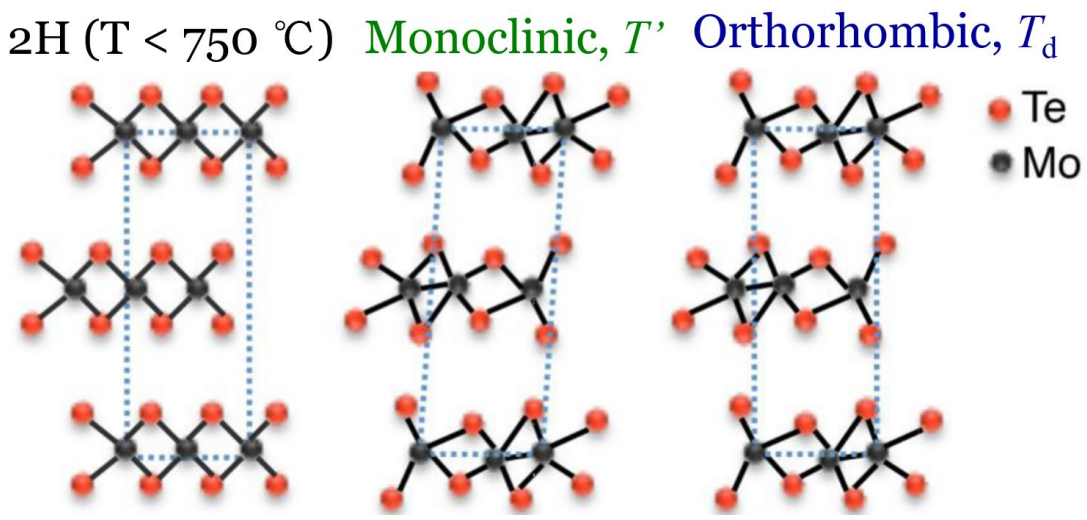


Figure 1.4: Crystal structure of hexagonal 2H-$MoTe_2$, monoclnic T'-$MoTe_2$ and orthorhombic $T_d$-$MoTe_2$ [60, 62].

$M_x$ and $M_y$, time reversal symmetry $\mathcal{T}$ and a rotation symmetry $C_4$. There are 24 Weyl nodes in the electronic structure of TaAs through ARPES [28, 29]. Large AHE and chiral anomaly have been discovered in TaAs. Recently, layered TMDCs, $WTe_2$ and $MoTe_2$, have been proposed as type-II WSM with larger tilted Weyl cones [10, 39]. For these Weyl materials, their electronic structures are sensitive to strain and pressure [78].

## 1.5 Introduction to $MoTe_2$

$MoTe_2$ is polymorphic with three different structures: hexagonal (2H-$MoTe_2$), monoclinic (T'-$MoTe_2$) and orthorhombic ($T_d$-$MoTe_2$) as shown in fig 1.5. 2H-$MoTe_2$ is famous for its semicondoctor properties and potential applications in spintronics. Such a metastable T' phase is quenched above 950 Celsius and could be strain-

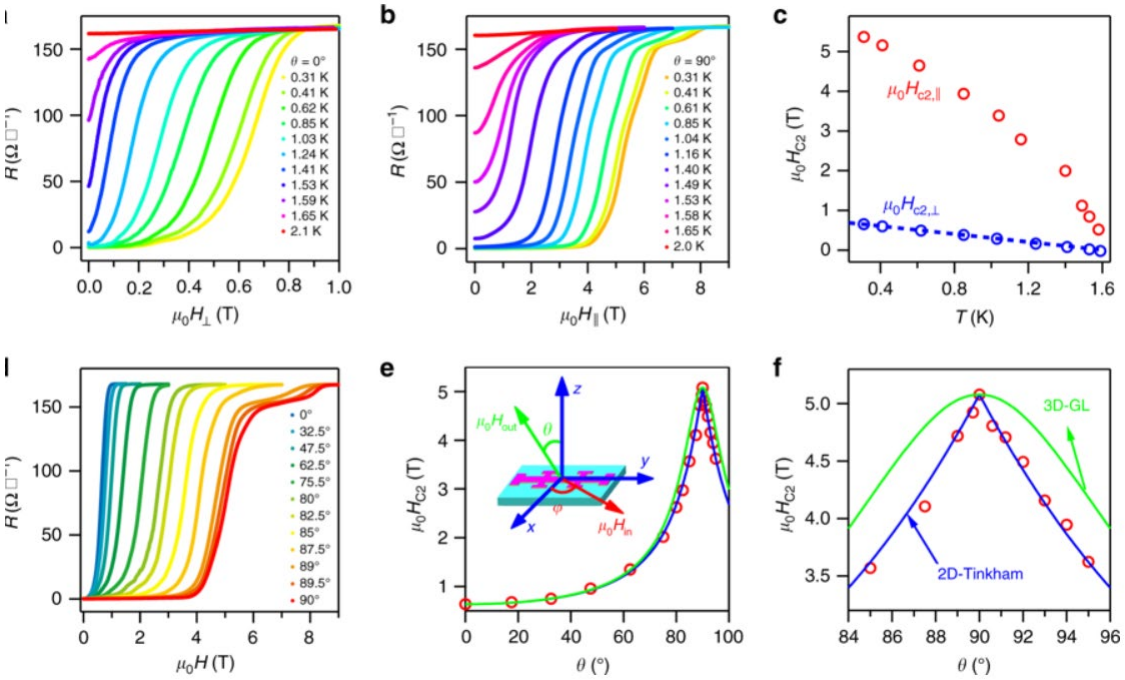


Figure 1.5: Superconducting resistive transition of the 8.6-nm-thick MoTe2 crystal in (a) perpendicular magnetic field and in (b) parallel magnetic field. (c) Temperature dependence of the upper $H_c$. The dashed line is fitting to the 2D Ginzburg-Landau theory. (d) Magnetic field dependence of the sheet resistance at T=0.3 K with different tilted angles $\theta$. (e) Angular dependence of the $H_{c2}$. The inset is a schematic drawing of the tilt experiment setup, where x, y, and z represent the crystallographic $b$, $a$, and $c$ axes. (f) The inset shows a zoom-in view of the region around $\theta = 90$ degree. The solid lines are the fitting with the 2D Tinkham formula (blue line) and the 3D anisotropic mass model (3D-GL) (green line), respectively. Adapted from [15]

induced from 2H-$MoTe_2$ [60, 62]. T'-$MoTe_2$ phase has a distorted CdI2 structure that crystallizes in the centrosymmetric space group $P2_1/m$. Its Mo atoms are coordinated by six Te atoms but shifted from the centre of the Te octahedra, resulting in the zigzag chains. Their bonding between the shifted Mo atoms corrugates the Te sheets and distorts the Te octahedra, causing the c axis to incline at an angle of 93.9. This structural phase transition from the high-temperature T' to the low-temperature $T_d$ phase with the noncentrosymmetric space group $P_{mn2_1}$ has been reported between 240 K to 260 K [30] . It is worth mentioning that $T_d$ phase shares the same in-plane crystal structure as the T' phase but has a vertical (90 degree) stacking. The type-II Weyl fermions are possible in the $T_d$ phase only where the inversion symmetry is broken.

Two-dimensional TMDCs with strong SOC possess many novel physics including topological phases, Ising superconductivity, and possible topological superconductivity. Due to the Ising SOC, monolayer 2H-$NbSe_2$ and gated 2H-$MoS_2$ with in-plane $H_{c2}$ far exceeding Pauli paramagnetic limit and were realized as Ising superconductiviity. The few-layer $T_d$-$MoTe_2$ also exhibits an in-plane $H_{c2}$ which goes beyond the Pauli paramagnetic limit as shown in figure 1.5. The in-plane $H_{c2}$ shows an emergent two-fold symmetry which is a result of an asymmetric SOC in $T_d$-$MoTe_2$ in the order of tens of $meV$ which may give rise to novel superconducting and spin transport properties. Such strong SOC will create strong triplet pairing correlations in the material and may affect the pairing symmetry as well. Due to its large magnitude, the SOC may also have effects on the spin transport of the system in

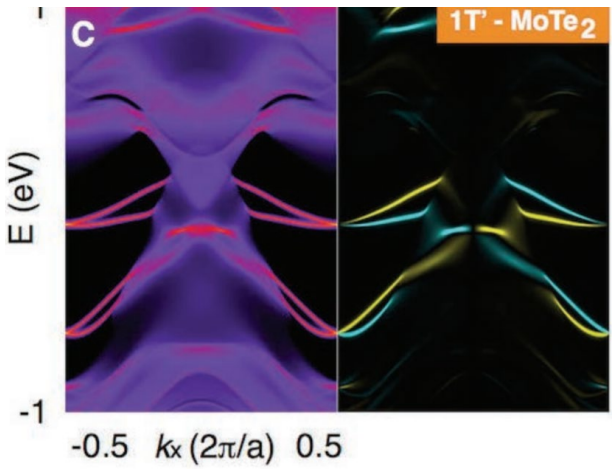


Figure 1.6: Electronic structure of helical edge states in 1T'-$MoTe_2$. The left subpanel shows the density of states while the right subpanel shows the corresponding spin polarization. These helical edge states are a manifestation of nontrivial topology, proposed for Quantum spin Hall effect through band structure calculation of monolayer-$MoTe_2$. Adapted from [68].

the normal states [68,69]. This new type of asymmetric SOC in $T_d$-$MoTe_2$ could be expected to promote further studies on the exotic superconducting and normal state phenomena in $T_d$-$MoTe_2$, and boost the possible applications in superconductivity in TMDCs.

### 1.5.1 Topological studies in $MoTe_2$

The monolayer-$MoTe_2$ has been proposed as TI and exists $Z_2$ invariant as its nontrivial Chern number [68]. The edge states and quantum spin Hall effect on a similar candidate for TI, ( monolayer of $WTe_2$), have been found in 2018 [68,69]. The research associated with the bulk electronic structure, edge states in the band structure, ground state of the atomic structure and $Z_2$ invariant has been used to predict the TI in monolayer of 1T'-$MoTe_2$ as shown in figure 1.5.1. Except the possible TI in monolayer $MoT2_2$, the bulk $T_d$-$MoTe_2$ has become the candidate of type-II

WSM. Figure 1.5.1 shows the unique surface Fermi arcs and Weyl nodes in good agreement with the ab-initio calculations in bulk $T_d$-$MoTe_2$ with nontrivial topological nature using ARPES. This work not only leads to the new understandings of the unusual properties discovered in $MoTe_2$ family, interplay between superconductivity and their topological order, but also provides a new platform for the realization of exotic physical phenomena and possible future applications [72]. Furthermore, recently first principle calculation proposed that bulk T'-$MoTe_2$ as a $Z_4$-nontrivial higher-order TI driven by double band inversions. Differentiated from the Weyl Fermi arcs, there exists the helical pairs of surface hinge states in T'-$MoTe_2$ while it is insulating in bulk [73]. The fruitful topologies in $MoTe_2$ family motivate novel and interesting studies of their electronic structures, structural transition, topological orders, and superconductivity.

### 1.5.2 Pressure study in type-II Weyl semimetal, $T_d$-$MoTe_2$

The recent pressure study of $T_d$-$MoTe_2$ shows that pressure enhances superconducting temperature and suppresses T'-$MoTe_2$ to $T_d$-$MoTe_2$ structural transition [30]. At ambient pressure, the bulk centrosymmetric T'-$MoTe_2$ phase at room temperature turns into orthorhombic $T_d$-$MoTe_2$ between 240 K and 270 K and becomes superconductor at 0.1 K. The superconducting temperature reaches 7.2 K around 11.4 Gpa and decreases with pressure. This first-order structural transition was gradually suppressed by pressure. The lattice structure changes to $T_d$-$MoTe_2$ at 1.3 Gpa and 135 K through X-ray diffraction under pressure. The $H_{c2}$ sug-

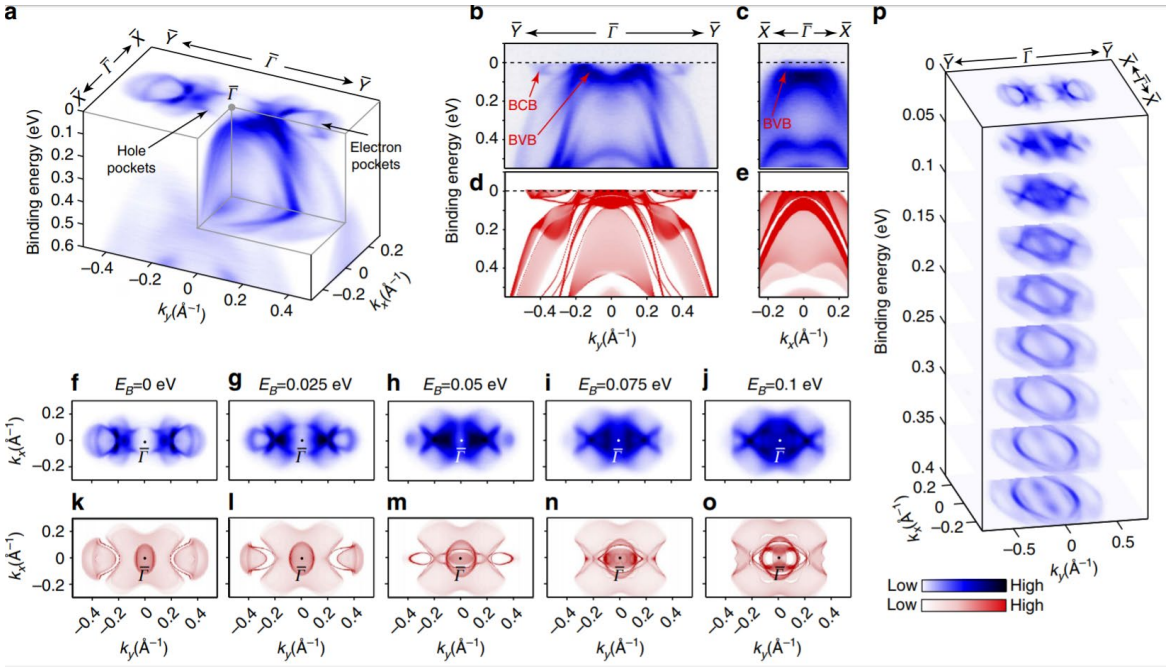


Figure 1.7: Observation of Weyl nodes and Fermi arcs in $MoTe_2$ through ARPES. (a) The 3D intensity plot of the photoemission spectra with the electron and hole pockets. (b - e) High symmetry cut and corresponding first-principle calculations along the Bulk Conducting Band (BCB) and Bulk valence Band (BVB). (f - o) Photoemission spectral intensity map in experiments and the relative DFT calculations showing the constant energy contours of bands. (p) Stacking plots of constant-energy contours in broader binding energy range show the band structure evolution. Adapted from [72].

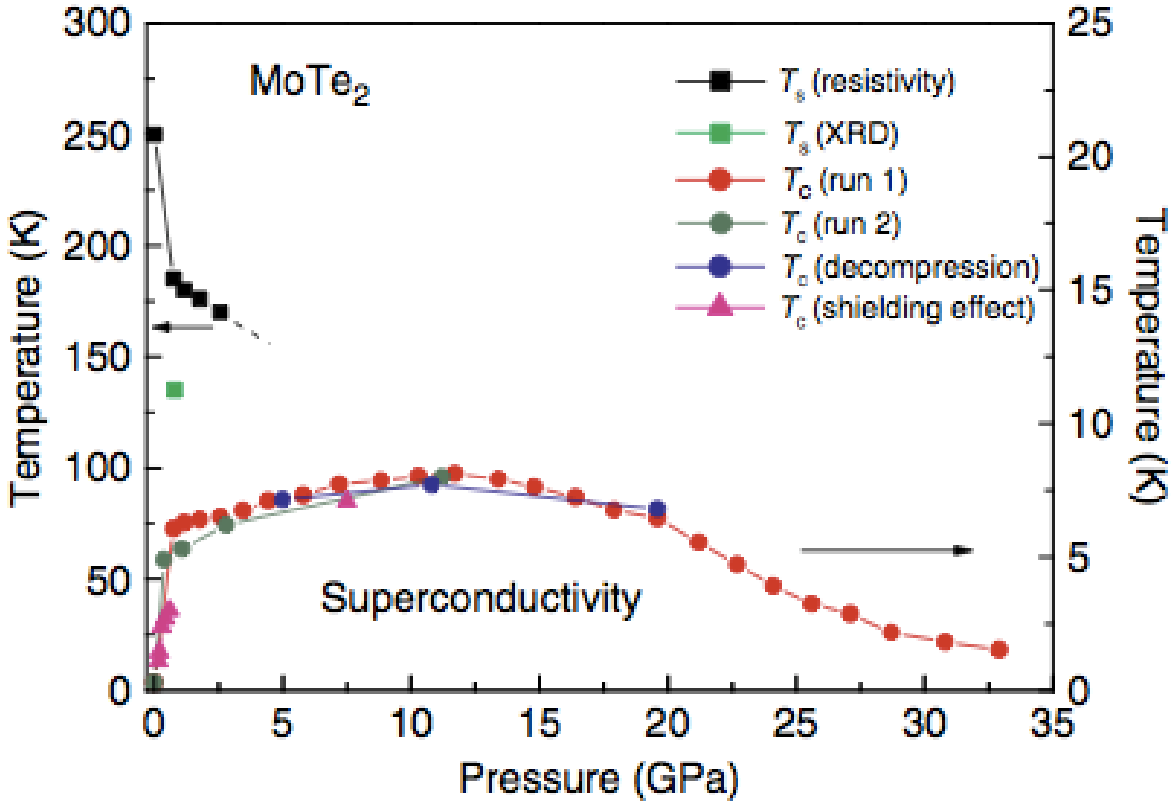


Figure 1.8: $MoTe_2$ electronic phase diagram under pressure. Adapted from [30].

gests that superconductor of $T_d$-$MoTe_2$ is an unconventional superconductor. The superconducting temperature suddenly rises and structural transition temperature simultaneously drops around 1.5 GPa. This behavior raises several interesting questions: (I) whether the structural transition is associated with the superconductivity transition; (II) whether $T_d$-$MoTe_2$ or T'-$MoTe_2$ drives superconducting transition; or (III) any other hidden phase induces the superconducting transition. The superconducting phase is cross $T_d$-$MoTe_2$ breaking lattice inversion symmetry and centrosymmetric T'-$MoTe_2$. Meanwhile, $T_d$-$MoTe_2$ is proposed as type-II WSM and potential topological superconductor. Furthermore, T'-$MoTe_2$ is claimed as a possible higher-order topological phase. The pressure range of clamp cell can be fine tuned below 2 GPa which is very applicable to study evolution of structures and

superconductivity in this pressure region. This would further reveal the relationship between the superconductivity, the structure transition and their relative topologies under pressure.

# Chapter 2: Methods

## 2.1 Sample growth and characterization

### 2.1.1 $Au_2Mn$

Au2Mn was prepared by arc melting of the high purity (6N) starting materials in an argon environment $Au_2Mn$ were prepared by arc melting of the high purity (6N) starting materials in an argon environment. They were homogeneously melting and further annealed for four days at 690 °C to yield polycrystals with higher crystallinity. The magnetic susceptibility measured with a SQUID magnetometer confirmed the Neel temperature at 363 K [56] of $Au_2Mn$.

### 2.1.2 $MoTe_2$

Powder samples were prepared using the standard solid state synthesis method using high purity Mo powder (5N metals basis excluding W, Alpha Aesar), and Te shot (6N, Alpha Aesar). Large single crystals were grown using the Te self flux method as described in using the same source metals as for the powder samples. High sample quality has been confirmed by x-ray and neutron diffraction, stoichiometry has been confirmed by wavelength dispersive spectroscopy, and the

samples measured have residual resistivity ratios greater than 1000.

## 2.2 Pressure Experiments

High pressure techniques can be combined with x-ray scattering, neutron scattering, heat capacity, thermal power, magnetization and transport measurements for multiple experimental purposes. The majority of these measurements can only be done with bulk samples, and hydrostaticity of the pressure varies with different pressure media such as small polymers, oil, or liquid helium. For high pressure transport measurements, the main difficulties are different designs, samples space, and contact issues.

### 2.2.1 Pressure cell design

Figure 2.1(a) shows the overview of the CTP-HHPC50 piston clamp pressure cell, which is usually used for transport measurement such as proximity detector oscillator, tunnel diode oscillator and resistance under pressure. The pressure range of the clamp cell below 30 K is typically below 3 Gpa and might push up to 6 Gpa with potential risks of damage of pressure cell and sample. We attach a sample with two pressure gauges on top of a feedthrough and seal it into the white telfon cap filled with pressure medium. All of inner piston, back plug and disk piston are used for the rigorous support and to secure the feedthough in cylinder cell. While we apply pressure through its outer piston, the inner piston pushes its telfon cap and whole volume of cap decreases. We lock the upper screw to fix the telfon capsule

and apply high pressure to our sample in cell. There are several choices of pressure mediums such as Daphne oil, polymer particles, and organic solvents. The liquid Helium provides the best hydrostatistics pressure, which is impossible in this system. Alternatively, alcohol and Daphne oil are relatively good selections. Several tests are required such as sample bahavior at ambient pressure and any chemical interactions between pressure medium and samples in our experimental temperature and field ranges.

### 2.2.2 Preparation of feedthrough

First of all, we design the feedthrough for different experiments as shown in figure 2.2(a). For regular four-point contact resistance measurement, we prepare eight to twelve wires. Each sample requires at least four copper wires. To get large enough variance of resistance in manganin wire under pressure, the resistance of manganin requires more than 30 $\Omega$ at room temperature. It is necessary to increase the number of wires and to arrange the sample space when considering multiple samples measurement or both MR and Hall measurements. Increasing the numbers of samples and wires also increases the possibility of contact shorting. For CTP-HHPC50 pressure cell, eight twisted pairs of copper wires are acceptable to measure four samples under pressure simultaneously. We use roughly 10 $cm$ long and thinner than 38 gauge copper wires and twist them to avoid improper inductance during measurements. It is important to keep the twisted pairs of copper wires insulated all the time. Those wires are sealed using black stycast 2850 FT and catalyst with

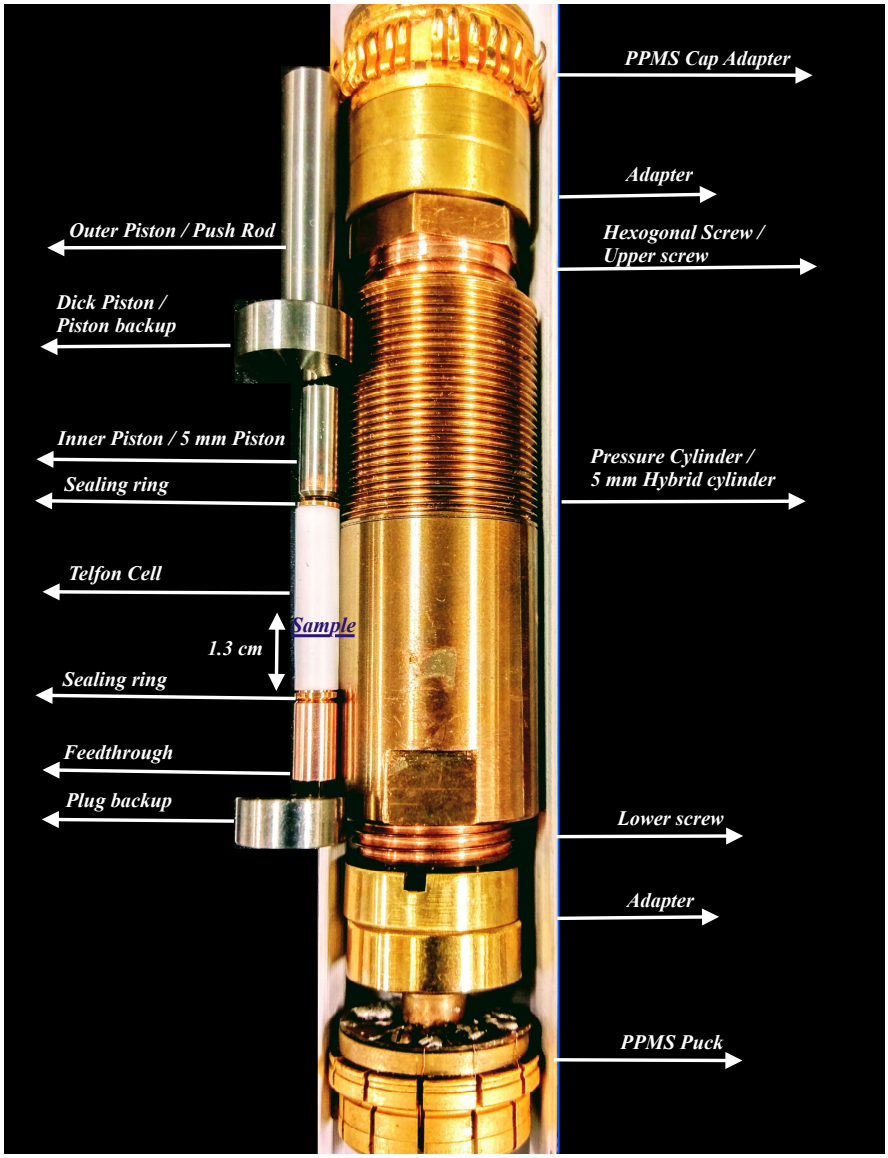


Figure 2.1: Overview of pressure cell structure and adapted to the PPMS puck. The sample and two pressure calibrations would be attached on top of feedthrough and sealed into the white telfon cap filled with pressure medium.

4.5 : 100 ratio by mass for 5 minutes. We air cure the black stycast for two days or cure the stycast 100°C in box furnace for three hours. Its shiny and hard surface will tell the high quality of cured stycast.

The volume of white teflon cap might be reduced and deformed with higher pressure. To keep homogeneous pressure and avoid destroying this white cap, it is best to keep sample 1 *cm* above the top of black stycast. On top of feedthrough, copper wires requires shorter than 6 *mm* to set sample at the best place. We solder a superconducting wire and a manganin wire for pressure calibration at based temperature and room temperature. Multiple choices of contacts for sample are determined by pressure medium. Generally, silver epoxy provides better bounding and is cured at 120 °C for 12 minutes. 1 : 1 ratio n-Pentane mixed with 1-methyl-3-butanol provides homogeneous pressure and its smell shows any leak of pressure medium during measurements. Daphne oil works for homogeneous pressure and silver paste, silver paint and epoxy contacts.

A sealing ring is placed on the neck of feedthrough and telfon capsule is filled with pressure medium using a syringe. No bubbles are allowed in the capsule. One must carefully and slowly seal the feedthrough after insert the sample side of feedthrough into the teflon cap. We push the pressure capsule into the backside of pressure cell and pull all copper wires through back cap and disk piston. To avoid shorting of these wires, it requires an insulating piece such as parts of kapton tape covering the inner wall of the back cap. Those wires were pulled vertically without bending when closing the back cap. We place another sealing ring and disk piston into pressure cell from its top side and close the top part of pressure cell as shown

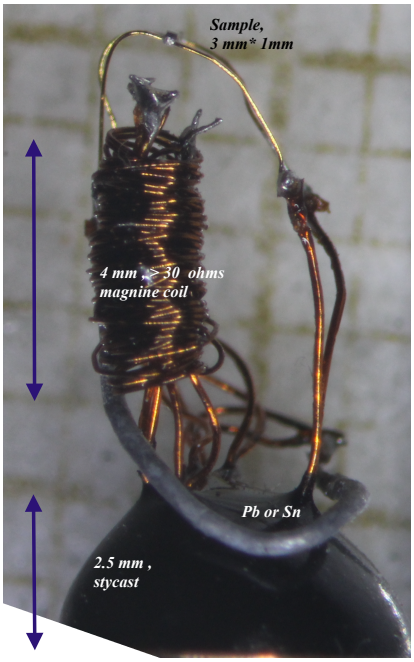


Figure 2.2: Overview of feedthrough structure. Manganin coil and a superconducting wire ($Pb$ or $Sn$) are used for the pressure calibration at room and based temperature. Usually, sample size is around $3mm \times 1mm \times 1mm$.

in figure 2.1(a).

### 2.2.3 Pressure calibration

To obtain the exact pressure at room temperature, we measure the pressure dependent resistance of manganin [36] and calculate its related pressure as,

$$P(kbar) = \frac{1000}{2.48}[\frac{R(P)}{R(P_0)} - 1]. \tag{2.1}$$

Here, $R(P)$ and $R(P_0)$ are the resistance of manganin under pressure and at ambient pressure. The pressure dependence of superconducting temperature ($T_c$) of tin and lead [37, 38]are

$$T_c(P) = 3.27 - 0.4823P + 0.0207P^2(Sn), \tag{2.2}$$

and

$$T_c(P) = 7.1863 - 0.3847P + 0.01769P^2(Pb), \tag{2.3}$$

which is used to calibrate the pressure below 30 K. Here, 3.27 and 7.1863 are the superconducting temperatures of tin and lead at ambient pressure.

The residual field of the PPMS magnet induces a significant error of the superconducting temperature of lead under pressure. At ambient pressure, critical magnetic field and superconducting temperature of lead are 803 $Oe$ and 7.19 $K$. Under 15 $Oe$ residual field, its superconducting temperature shifts 0.15 $K$ shown in Fig. 2.4. Such a tiny residual field results in a 4.1 $kbar$ error. To eliminate the residual field in PPMS, we use R-H curve of $Pb$ to figure the residual field and apply precisely opposite direction of magnetic field. Figure 2.3 shows that superconducting temperature of lead decreases with higher pressure, which can be substituted into Eq. 2.2 for its corresponding pressure below 30 K. Pressure at based temperature decreases by 4 to 5 $kbar$ compared with the one at room temperature because of its thermal contraction of pressure cell upon cooling.

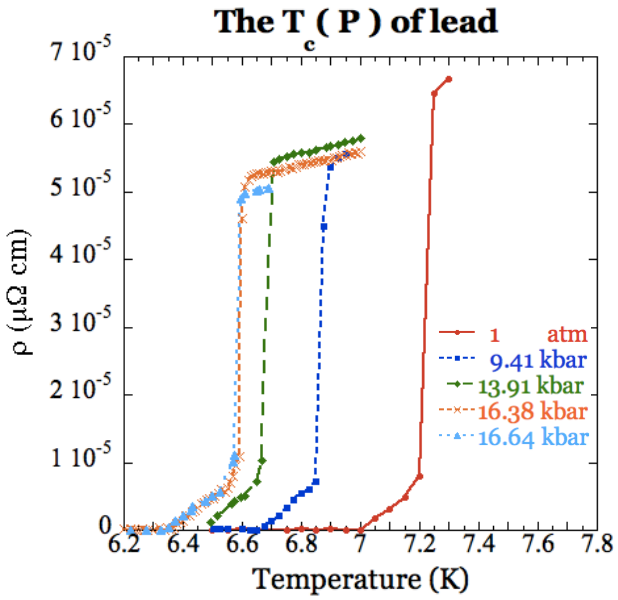


Figure 2.3: The pressure dependence of the superconducting transition temperature of lead below 16.64 kbar.

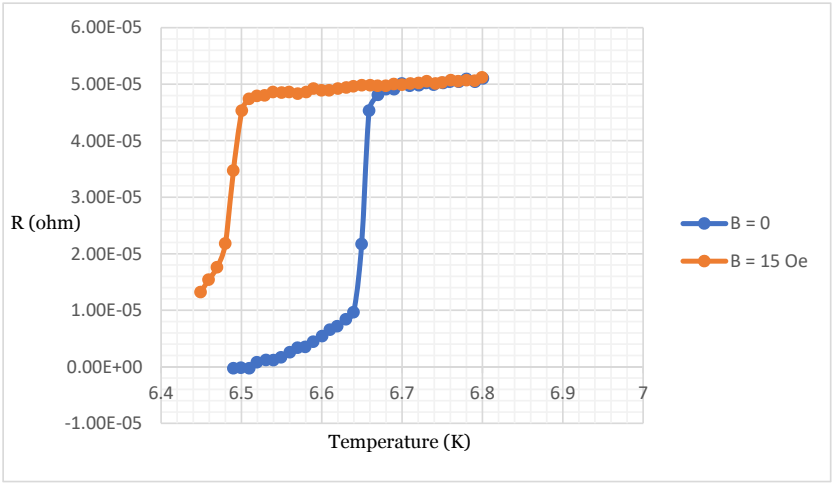


Figure 2.4: The superconducting temperature of lead varies 0.15 K at the residual field between zero field and 15 $Oe$, which is corresponding to 4.1 kbar error in pressure calibration.

## 2.3 Ab-initio calculation

The total energy, structure optimization under pressure were performed by Taner Yildirim at NIST using Quantum Espresso, [97], which is based on density functional theory, using a plane wave basis set and fully relativistic all-electron projected augmented wave (PAW) potentials [98, 99]. The $4s, 4p, 4d$, and $5s$ electrons of Mo and the 4d, 5s, and 5p electrons of Te were treated as valence. We used 0.02 Ry Methfessel-Paxton smearing with wavefunction and charge density cut-off energies of 100 Ry and 800 Ry, respectively. The exchange-correlation interactions were described by the generalized gradient approximation (GGA) with the Perdew-Burke-Ernzerhof exchange-correlation functional [100]. The Brillouin-zone integration were performed using MonkhorstPack grids of special points with $16 \times 8 \times 4$ for total energy and structure optimizations and $32 \times 16 \times 8$ with tetrahedra method for electronic density of states and Fermi surface calculations. The spin-orbit (SO) interactions and the weak inter-layer van der Waals (vdW) interactions were all included in our calculations. We used grimme-d2 [101] vdW correction with parameter $london - s6 = 0.6$. The effect of electron correlations are included within DFT+U method with U = 3.0 eV for the Mo $4d$-states. Including electron-correlation brings the calculated band structure and Fermi-surface into excellent agreement with quantum oscillations and ARPES measurements as found in very recent studies [102,103]. Fermi-surface sheets and SdH orbits are visualized by our custom python code using Mayavi [104]. The quantum oscillations frequencies/orbits and their angle dependence were calculated using the skeaf code [105].

## 2.4 Quantum oscillations

Quantum oscillations in the transport properties of metallic and semiconducting materials arise directly from the magnetic field dependence of the conduction electron energies. It is a powerful experimental probe of the electronic band structure close to the Fermi energy and provides details of electron properties such as Dingle temperature, effective mass and mobility. Magnetic field dependent quantum oscillations in electronic resistivity were first discovered in $Bi$ by Shubnikov and de Haas in 1930 [106]. The SdH effect is a macroscopic manifestation of the inherent quantum mechanical nature of matter occurring at low temperature and high magnetic field. It is often used to decide effective mass of charge carriers (electrons and holes). Angle dependence of SdH oscillations can decide the dimension and shape of Fermi surfaces, which is important to distinguish two-dimensional and three-dimensional Fermi surfaces for topological properties.

For topological systems including DSM, WSM, and TI, the nontrivial Berry's phase, $\pi$ could be obtained for the nontrivial surface states. The Berry's phase is very sensitive to the error bar from multiple band of Lifshitz-Kosevich formula. Here, we applied the global fitting with Markov chain Monte Carlo (MCMC) methods [95] to compute the joint distribution of parameter probabilities and get the expected value and uncertainty of the Berry's phase.

### 2.4.1 Shubnikov-de Haas oscillations

The general form of longitudinal conductivity is $\sigma_{xx} = \frac{\rho_{xx}}{(\rho_{xx}^2+\rho_{xy}^2)}$, here, $\rho_{xx}$ and $\rho_{xy}$ are the longitudinal and transverse resisitivity. In $MoTe_2$, its longitudinal resistivity is always much larger than transverse (Hall) resistivity ( $\rho_{xx} >> \rho_{xy}$, three to four orders larger below 2 Gpa [77]), the oscillatory component of $\sigma_{xx}$ obtained by taking the derivative, $\Delta\sigma_{xx} = \Delta\frac{1}{\rho_{xx}} = -\frac{\Delta\rho_{xx}}{\rho_{xx}^2}$. Quantum oscillations must consider the quantization of motions of electrons under the magnetic field. The modified Lifshitz-Onsager quantization relation describes the closed trajectory of a charge carrier by an external magnetic field B as a function of Berry's phase and Zeeman splitting parameter $S$,

$$A_n\frac{\hbar}{eB} = 2\pi(n + \frac{1}{2} - \frac{\Phi_B}{2\pi} \pm \frac{1}{2}S) = 2\pi(n + \gamma \pm \frac{1}{2}S). \tag{2.4}$$

Here, $A_n$ is the cross-sectional area of the Fermi surface related to the Landau level (LL) n, Berry phase $\Phi_B$, and splitting parameter is defined as $S = \frac{1}{2}g\frac{m}{m*}$. $m$ is the effective mass of charge carrier and $g$ is the Landau g factor.

To analyze the bulk SdH oscillations signal, we adopted the formula of $\rho_{xx}$,

$$\rho_{xx} = \rho_0\{1 + \frac{5}{2}\sum_{r=1}^{\infty} b_r\cos(\theta \pm rS\pi) + R\}, \tag{2.5}$$

where,

$$R = \frac{3}{8}\frac{\hbar\omega_c}{E_F}\{\sum_{r=1}^{\infty} b_r[\alpha_r\cos(\theta \pm rS\pi) + \beta_r\sin(\theta \pm rS\pi)] - ln(1 - e^{-\frac{4\pi\Gamma}{\hbar\omega_c}})\}, \tag{2.6}$$

$$b_r = \frac{1}{r^{\frac{1}{2}}}(\frac{\hbar\omega_c}{2E_F})^{\frac{1}{2}}\frac{2\pi^2k_BT/\hbar\omega_c}{\sinh(2\pi^2k_BTr/\hbar\omega_c)}e^{-\frac{2\pi\Gamma}{\hbar\omega_c}r}. \tag{2.7}$$

$$\alpha_r = 2r^{\frac{1}{2}}\sum_{s=1}^{\infty}\frac{1}{[s(r+1)]^{\frac{1}{2}}}e^{-\frac{4\pi\Gamma}{\hbar\omega_c}s}, \tag{2.8}$$

$$\beta_r = r^{\frac{1}{2}} \sum_{s=1}^{r-1} \frac{1}{[s(r-s)]^{\frac{1}{2}}}, \tag{2.9}$$

and

$$\theta = 2\pi(r(\frac{B_F}{B} + \gamma) + \delta). \tag{2.10}$$

Here, $\rho_0$ is the nonoscillatory component of resistivity at zero field, and other parameters are Dingle temperature $T_D$, cyclotron frequency $\omega_c = eB/m^*$, and Boltzmann's constant $k_B$ and harmonic order $r$. The Landau level-broadening width $\Gamma$ is caused by scattering and associated with Dingle temperature ($\Gamma = \pi k_B T_D$). To extract the Zeeman splitting, we simply the sum of phase term as

$$\cos(\theta+rS\pi)+\cos(\theta-rS\pi) = 2\cos\theta\cos(Sr\pi) = 2\cos(\frac{1}{2}r\pi g\frac{m*}{m_0})\cos(2\pi(r(\frac{B_F}{B}+\gamma)+\delta)) \tag{2.11}$$

$$\sin(\theta+rS\pi)+\sin(\theta-rS\pi) = 2\sin\theta\cos(Sr\pi) = 2\cos(\frac{1}{2}r\pi g\frac{m*}{m_0})\sin(2\pi(r(\frac{B_F}{B}+\gamma)+\delta)) \tag{2.12}$$

Here, $2\cos(\frac{1}{2}r\pi g\frac{m*}{m_0})$ is a reduction factor due to the Zeeman splitting.

Experimentally, oscillatory frequency ($B_F$) and effective mass (m*) are determined through the FFT of quantum oscillations signal and temperature dependent amplitude of oscillation peak in frequency. $\delta$ is the topological phase shift, which is determined by the dimensionality of Fermi surface, $\delta = 0$ ( or $\delta = \pm\frac{1}{8}$ ) for the 2D (or 3D) system [79–81]. Therefore, $|\gamma - \delta| = |1/2 - \phi_B/2\pi - \delta|$ between 0 and 1/8 indicates a nontrivial $\pi$ Berry's phase. Berry's phase determination is very sensitive to the Zeeman effect and the Fermi surface might distort close to the quantum limit. The $R$ term is too small to change analysis ($\frac{3}{8}\frac{B}{B_F} < \frac{1}{16}$ for frequency higher than

100 T). Therefore, the longitudinal resistivity is

$$\rho_{xx} = \rho_0\{1 + \sum_{r=1}^{\infty}[(\frac{\hbar\omega_c}{E_F})^{1/2}\cos(\frac{r\pi gm*}{2m_0})e^{\frac{-2\pi^2 k_B T_D r}{\hbar\omega_c}}\frac{\frac{2\pi^2 k_B T r}{\hbar\omega_c}}{\sinh(\frac{2\pi^2 k_B T r}{\hbar\omega_c})}\cos(2\pi((\frac{B_F}{B}+\gamma)r-\delta))\}. \tag{2.13}$$

These periodic SdH oscillations in MR follows the Lifshitz-Kosevich (LK) formula for three-dimensional system [88–90] as,

$$A(B,T) = \frac{\Delta\rho}{\rho_0} \propto (\frac{\hbar\omega_c}{E_F})^{1/2}\exp(-2\pi^2 k_B T_D/\hbar\omega_c)\frac{2\pi^2 k_B T/\hbar\omega_c}{\sinh(2\pi^2 k_B T/\hbar\omega_c)}. \tag{2.14}$$

The first order harmonic of oscillation signal in 3D LK formula dominates the oscillation signal [88–91], this gives,

$$\rho_{xx} = \rho_0[1 + A(B,T)\cos(\frac{\pi gm*}{2m_0})\cos 2\pi(B_F/B - \delta + \gamma)]. \tag{2.15}$$

If the Zeeman splitting term does not change within the experimental magnetic field (Namely, the g factor is a constant in this field range for each band), this term is decoupled with phase of oscillations, $cos(2\pi(B_F/B - \delta + \gamma))$. In other words,

$$\rho_0 A(B,T)\cos(\frac{\pi gm*}{2m_0}) = A_0, \tag{2.16}$$

g factor only varies the oscillation amplitude ($A_0$) and will not change the phase of oscillations. This results mean that we could decouple Berry's phase and the phase shift $\delta$ from g factor, Zeeman parameter.

### 2.4.2 Angle dependence of Shubnikov-de Haas oscillations

The angle dependence of the SdH oscillations maps out the shape of Fermi surface. For an ellipsoidal Fermi surface, the oscillatory frequency of ellipsoid model

fits $F_{3D}(\theta) = \frac{F_{\theta=0}F_{\theta=90}}{\sqrt[2]{F_{\theta=0}^2\cos^2\theta + F_{\theta=90}^2\sin^2\theta}}$, here, $\theta$ is the angle between the magnetic field and the normal vector of sample surface. This ellipsoid model represents a proportionality of the cross-section of three-dimensional ellipsoidal Fermi pocket. For two-dimensional Fermi surface model, the SdH oscillatory frequency diverges much faster with the increasing of angle, $\theta$, proportional to $F_{2D}(\theta) = \frac{F_{\theta=0}}{\cos\theta}$.

### 2.4.3 Global fitting: *Bumps*

To find the global minimum of multiple bands model in Lifshitz-Kosevich formula, we get the expectation values of effective mass and oscillatory frequency of the charge carriers according to the temperature dependence of oscillation amplitude and Fast Fourier Transform (FFT) of SdH oscillations. First, we apply nonlinear regression to quickly search local minimum and include the real experimental errors for global minimum of LK formula. The consistent results of variables such as Dingle temperature and Berry's phase indicate convergence of the fitting parameters.

*Bumps* is a set of free and public routines for complicated curve fitting, uncertainty analysis and correlation analysis from a Bayesian perspective [95]. To see the distributions of uncertainty and correlation plots, we run *Bumps* for the rest of variables, amplitude of oscillation, Dingle temperature and Berry phase. In general the faster algorithms (Levenberg-Marquardt, Quasi-Newton BFGS) tend to find the local minimum quickly rather than the slower global minimum. *Bumps* provides uncertainty analysis which explores all viable minima and finds confidence intervals on the parameters based on uncertainty from experimental errors.

*Bumps* includes Markov chain Monte Carlo (MCMC) methods [95] to compute the joint distribution of parameter probabilities. The MCMC explores the space using a random walk and requires hundreds of thousands of function evolution to explore the search space. The histogram range represents the 95 % credible interval, and the shaded region represents the 68 % credible interval. For full uncertainty analysis, *Bumps* uses a random walk to explore the viable parameter space near the minimum, showing pair-wise correlations between the different parameter values. The 2D correlation plots indicate the correlation relationship between multiple parameters in the fitting function. With *Bumps*, we could check the convergence of fitting sequence and compare different local minimum to get the global minima.

### 2.4.4 Data analysis of Shubnikov-de Haas oscillations.

Berry's phases of multiple band system are sensitive to oscillatory frequency and Dingle temperature. It is a challenge to analyze the Berry's phases in multiple bands system especially that their Fermi surfaces might become distorted under large field. Possible error sources of analysis might come from Landau limit, Zeeman effect and nonlinear spin splitting. We use the non-linear regression fitting and process the global fitting with *Bumps* to determine Berry's phase. Our data were performed under a relative small magnetic field ( 6 $\sim$ 20 T) assuming a minimal amount of distortion to the Fermi surface and Berry's phase. Table 4.8 indicates oscillatory frequency, Dingle temperature, effective mass of each pockets, the corresponding Berry's phase et al. from ambient pressure to 1.8 GPa. Figure **??** shows the best

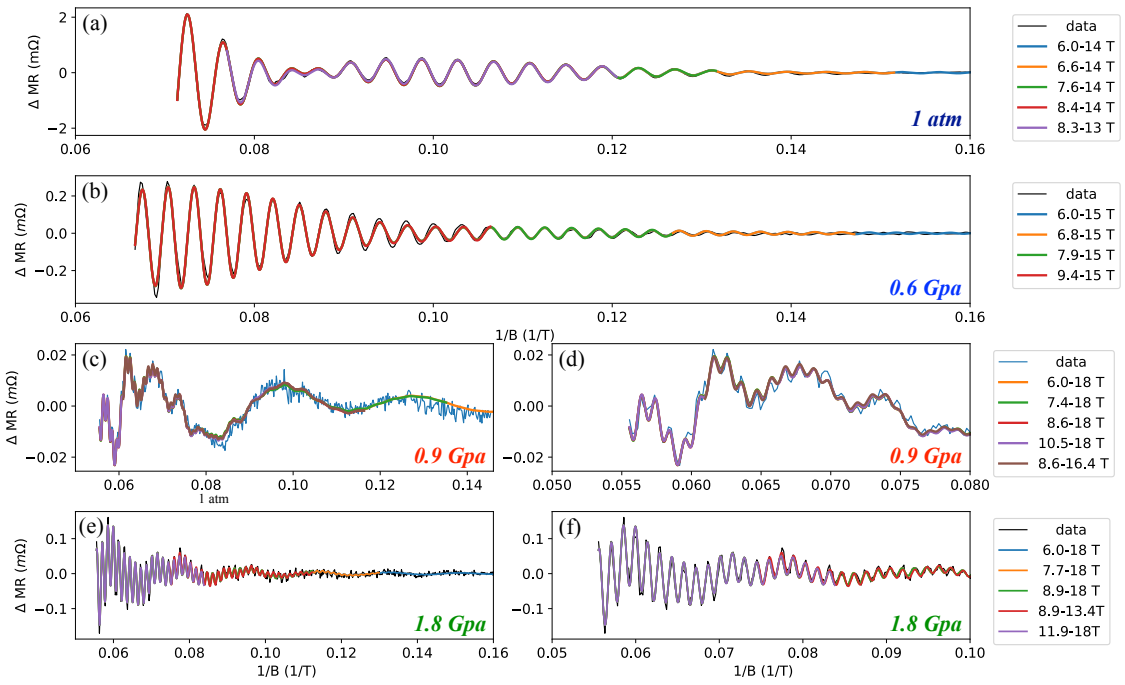


Figure 2.5: LK fits in multiple band system in $MoTe_2$ made at 1.8 K and (a) 1atm through Physical Property Measurement System (PPMS), and (b) 0.6 GPa one is made in a dilution refrigerator were taken using a lakeshore LS370 AC resistance bridge down to 0.1 K. Higher pressure cases such as (c, d) 0.9 GPa at 0.27 K and (e,f) 1.8 GPa at 0.3 K are preformed by Oxford Heliox.

fitting curves of SdH oscillations signal from 1 *atm* to 1.8 GPa in different field range. We show the expectation value and uncertainties for fitting data under 1atm (Fig. 2.6), (0.6 GPa, 0.9 GPa and 1.8 GPa are listed in Appendix.)

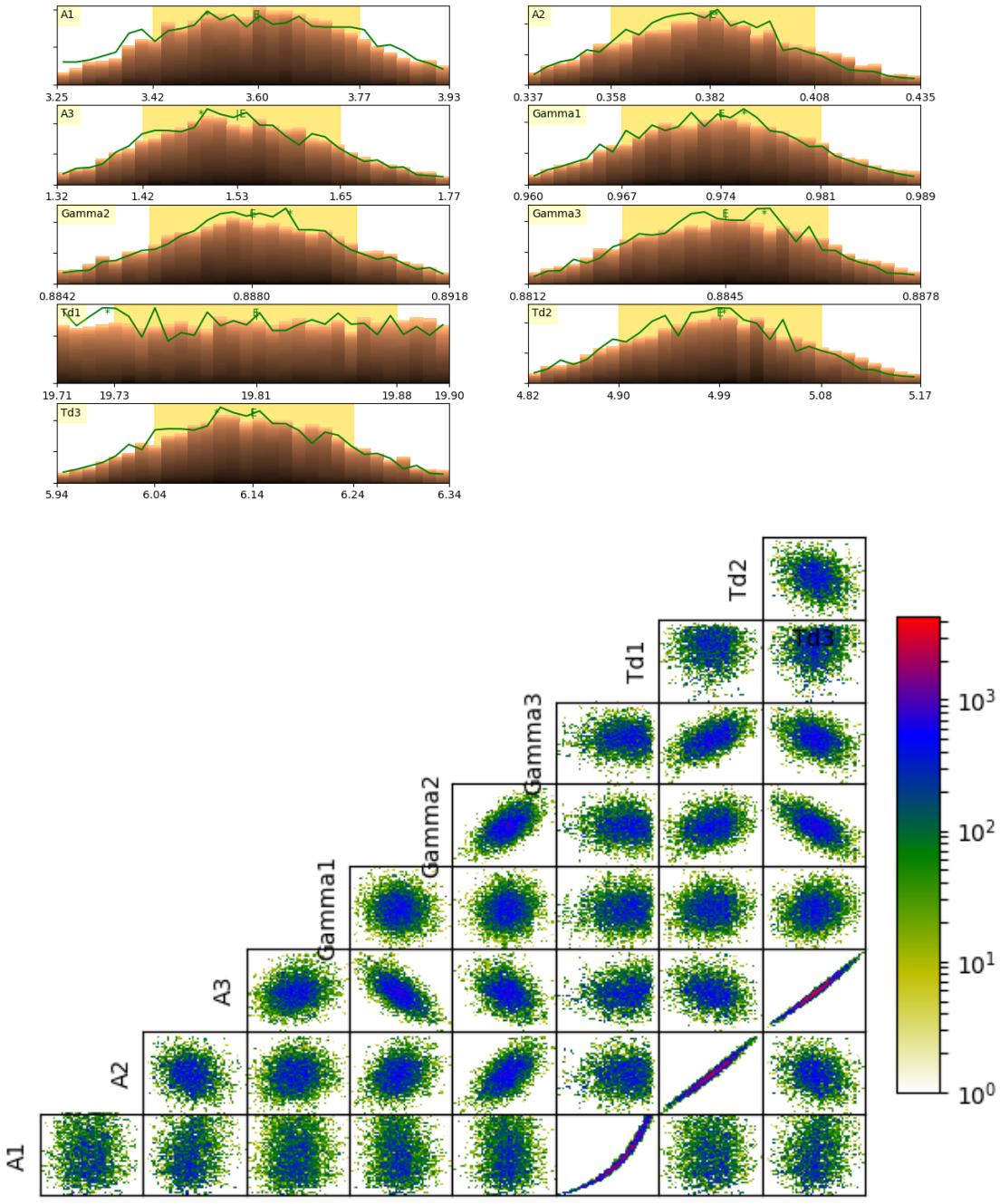


Figure 2.6: This is the (a) uncertainty of Lifshitz-Kosevich formula fitting in $MoTe_2$ made at 1.8 K and 1 atm. The Berry's phase of $F_\gamma$, $F_\alpha$, and $F_\beta$ are $(0.97 \pm 0.02)\pi$, $(0.89 \pm 0.01)\pi$ and $(0.88 \pm 0.01)\pi$. The parameters, B, $\gamma$, $T_d$, and $A$ are oscillatory frequency, Berry's phase, Dingle temperature and maximum oscillation amplitude. (b) The 2D correlation plots between each two parameters in our fitting formulas. There is positive correlation between maximum oscillation amplitude and Dingle temperature. The Berry's phase shows no correlation with Dingle temperature and oscillation amplitude.

## 2.5 Neutron diffraction

### 2.5.1 $Au_2Mn$

Neutron diffraction is a powerful tool to directly investigate the spin angle and spiral magnetic structure. For the study of nuclear and magnetic structures, neutron diffraction experiments were performed on $Au_2Mn$ at the NIST Center for Neutron Research (NCNR, Gaithersburg, USA), on high resolution powder diffractometer BT1 with Ge311 as monochromator and analyzer and wavelength of 2.079 Å. The Bragg diffraction occurs

$$2d \sin\theta = n\lambda, \tag{2.17}$$

where, d is the lattice constant, $\lambda$ and $\theta$ are the wavelength of incident wave and scattering angle. After momentum transfer, $Q$ is a vector that descibes the momentum transfer of scattering, defined as follows:

$$Q = [4\pi \sin\theta]/\lambda, \tag{2.18}$$

, or $Q = 2\pi/d$. The study of magnetic structure as a function of pressure and temperature was undertaken on BT1 (NCNR). The polycrystal samples were placed in HW-03 pressure cell with maximum pressure 10 kbar as well as the expected neutron transmission rate 25 %. To achieve the best hydrostaticity, a helium pressure transmitting medium was used.

### 2.5.2 Structural Measurements in $MoTe_2$

Determinations of the temperature and pressure dependent crystal structure were made using elastic neutron scattering measurements at 14.7 meV on the BT-4 triple axis spectrometer at the NIST Center for Neutron Research using a collimation and filter setup of open-pg-40'-pg-s-pg-40'-120' where pg refers to pyrolytic graphite. Single crystals were mounted in a steel measurement cell aligned in the $H0L_M$ zone and He was supplied as a pressure medium to maintain hydrostatic pressure conditions as described elsewhere [78]. The $T_d$ and T' phases and their volume fractions were identified from the position and intensity of $(201)_M$ reflections, which both split in $2\theta$ and shift in $\omega$ in the T' phase. Rocking curves and $\omega$-$2\theta$ scans were taken at each pressure and temperature. Scans along (00L) from (2 0 0.5) to (2 0 4.5) were also obtained at 0.8 GPa in the all $T_d$ or T' condition, as well as in the mixed region at both 0.8 and 1 GPa to look for possible superstructure . None were observed. Neutron experiments were performed through Colin Heikes at NIST Center for Neutron Research.

# Chapter 3: Helimagnets

To further investigate the phase transition and critical phenomena in $Au_2Mn$, we measure the $H_c$ from SS-FM through magnetization and MR at ambient pressure and take the advantage of $H_c$ to map out the related phase boundary and critical pressure. Pressure drives this system into second order phase transition. The anomalous magnetic peak in MR under low temperature and magnetization are quite similar to another three dimensional skyrmion material, MnGe with simple cube skyrmion structure, however, we did not see the corresponding AHE [46,47].

## 3.1 Temperature dependence of Magnetic measurement

In order to obtain the pressure dependence of magnetic structure in $Au_2Mn$, high-resolution powder diffraction measurements were preformed on the diffractometer BT1 at NCNR, which is particularly ideal for this spiral study by the means of high resolution at low angles. At ambient pressure and 4 K, neutron diffraction pattern of $Au_2Mn$ indicates that the magnetic $000^+$ peak is pure, clean and relative intense because of the contribution of the strong Bessel form factor of $3d$ electrons of Mn at low angle region. In Fig. 3.1(a), the scattering vector of magnetic $000^+$ peak

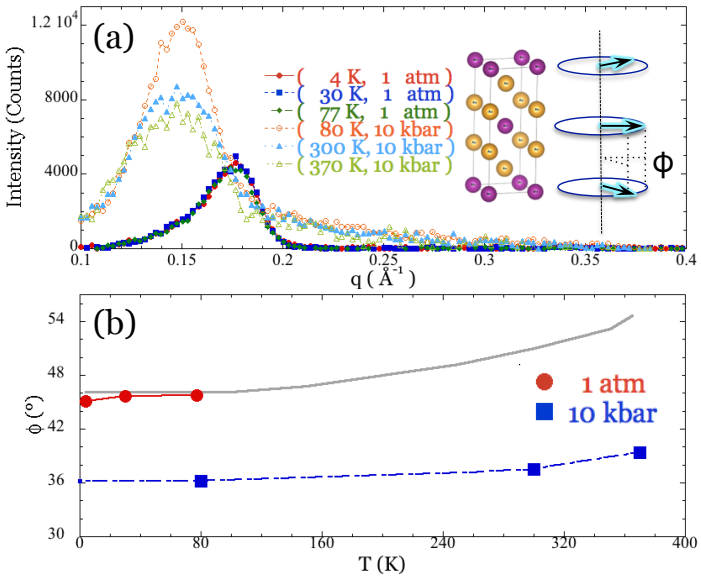


Figure 3.1: ( a ) The scattering vector of magnetic $000^+$ peak moves from 0.18 $\mathring{A}^{-1}$ to 0.15 $\mathring{A}^{-1}$ and spin angle also shrinks to 38° while pressure rises to 10 kbar. ( b ) The comparison of the T-dependence of spin angle measured from $(0,0,0)^+$ peak at ambient pressure (red spot) and 10 kbar (blue square), the gray line follows data from [55]. The error bar is small and within the marker.

moves from 0.18 to 0.15 while pressure rises from ambient pressure and below 77 K to 10 kbar and between 80 to 370 K, which means the period of spiral structure extends from 7 to 8.3 nm. Figure 3.1(b) shows the comparison of corresponding spin angle in $Au_2Mn$ at ambient pressure (red dot) and 10 kbar (blue square), which 0.1° error bars are within maker. The spin angles are 45.8° ± 0.1°, 45.1° ± 0.1° and 45.7° ± 0.1° measured at ambient pressure and 4 K, 30 K and 77 K, which agrees with reference [55]. The consistency of spin angle simultaneously confirms the consistent magnetic property of sample preparation between argon-Arc-melted and melt-spinning.

The scattering vector along c axis remains 0.018 with constant spin angle 45.9° as temperature is below 100 K, which means that the spiral structure is not sensitive

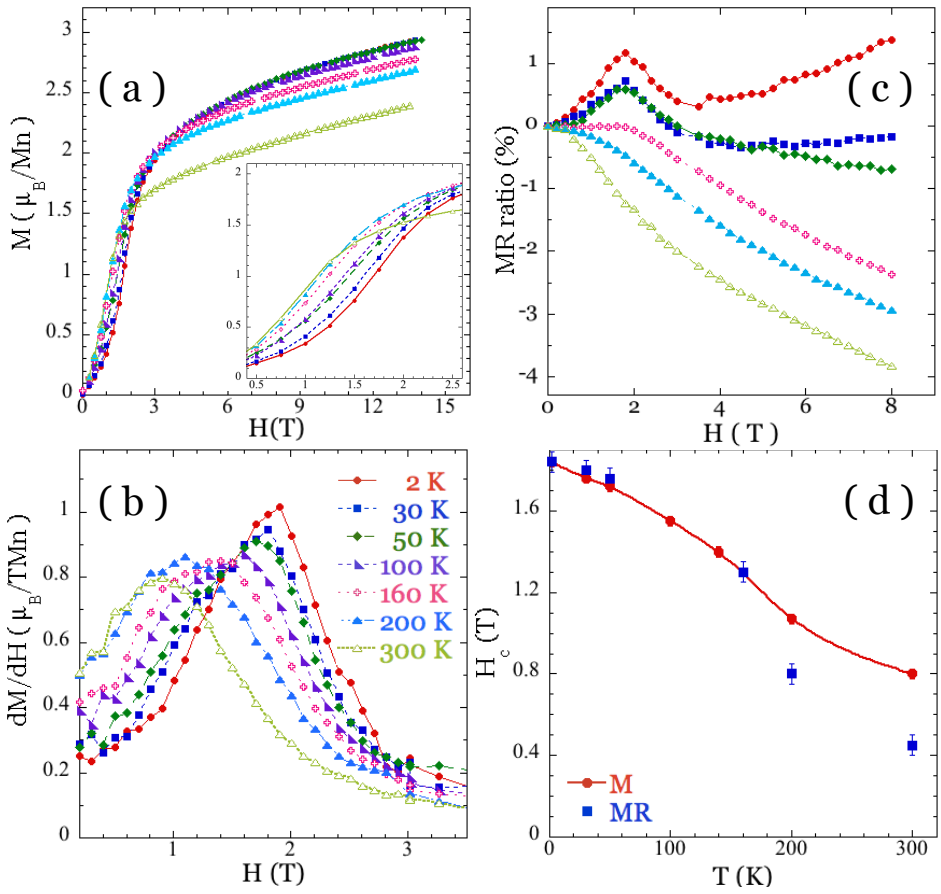


Figure 3.2: ( a ) M and ( b ) The first derivative of M of $Au_2Mn$ polycrystal. Inset is to zoom in the distorted spiral transition. ( c ) The MR ratio of $Au_2Mn$ at ambient pressure. ( d ) The Temperature dependence of $H_c$ obtained from M (red dot line) and MR (blue square) under ambient pressure.

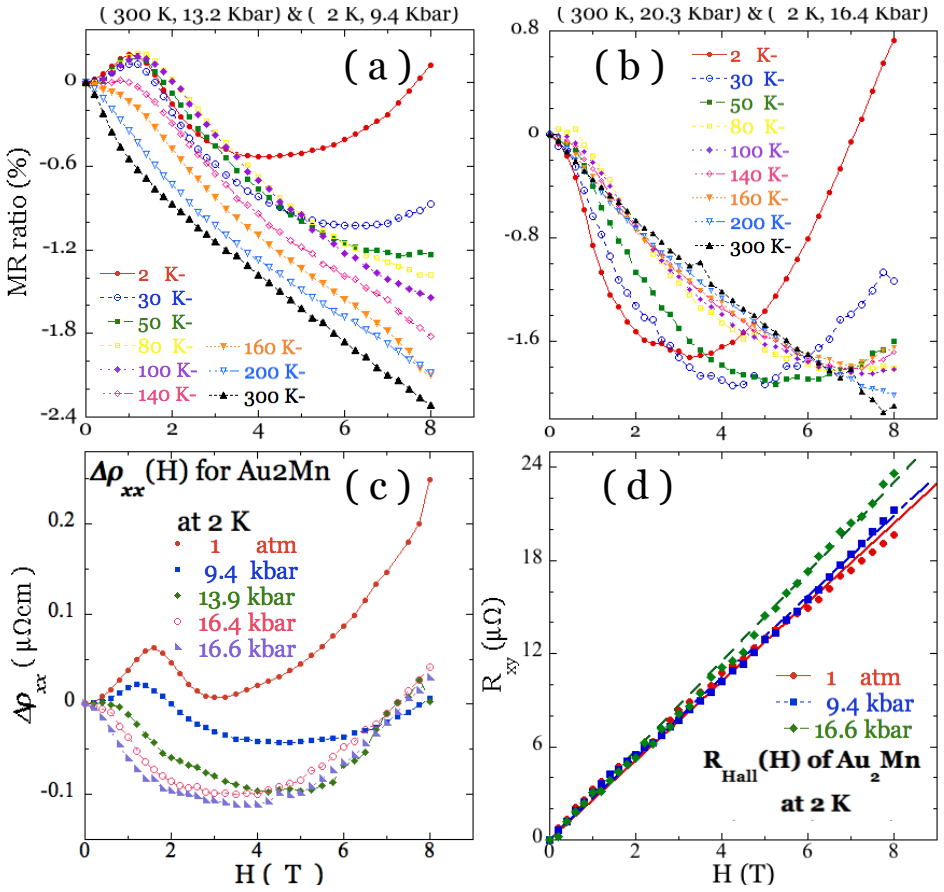


Figure 3.3: Temperature dependence of MR ratio in $Au_2Mn$ under ( a ) 13.2 kbar and ( b ) 20.5 kbar at room temperature. Pressure dependence of ( c ) MR and ( d ) Hall resistance of $Au_2Mn$.

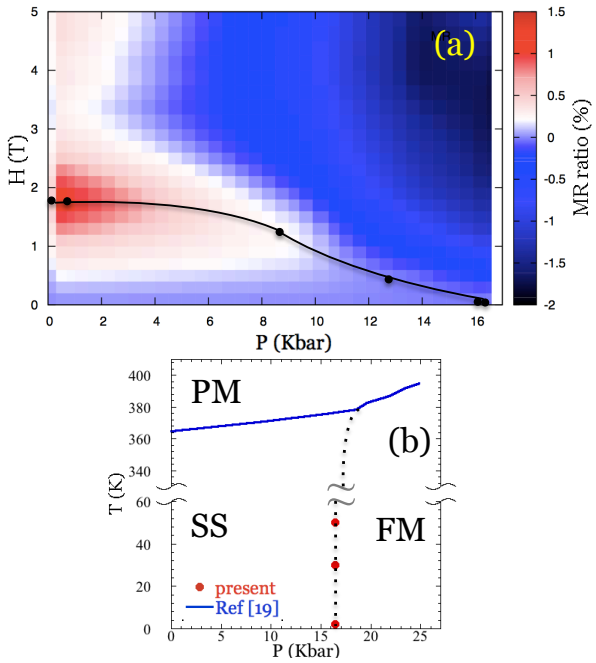


Figure 3.4: ( a ) Contour mappings of MR of $Au_2Mn$ at 50 K in P-H plane. transition metal dichalcogenide( b ) P-T phase diagram of $Au_2Mn$ showing the SS-FM phase boundary (red dots), Neel temperature and curie temperatures(blue square) [58].

to temperature. Under 10 kbar, the spin angles slightly increases from $36.18° \pm 0.1°$, $37.54° \pm 0.1°$ and $39.38° \pm 0.1°$ measured from 80 K, 300 K and 370 K. Between 80 K to Neel temperature, spin angle at 10 kbar only increases 3.2° compared with 10.4° at ambient pressure, which is to say that high pressure enhance the stability of the magnetic structure and its spin angle. Through the 002 structure peak, and c-axis lattice constant decreases from 8.743 Å to 8.732 Å with $1.69 \times 10^{-4}$ Å per K ratio as temperature drops from 77 K to 4 K at ambient pressure. Under 10 kbar, the lattice constant of c-axis drops from 8.7 Å to 8.68 Å with $8.3 \times 10^{-5}$ Å per K ratio from 300 K to 80 K, only half ratio as ambient pressure, and keeps around 8.7 Å at 10 kbar and temperature above 300 K. The larger thermal constraint ratio at ambient pressure results in relative larger change in spin angle.

Temperature dependence of magnetization at ambient pressure shows the SS-FM phase transition and the corresponding $H_c$. The magnetization curves were taken by MPMS (Quantum Design, Inc.) from 2 K to 300 K up to 14 T as shown in Fig. 3.2(a). The magnetic structure is spiral spin at zero field, turns into distorted spiral while applied field less than $H_c$ and finally polarizes to FM above critical filed. The inserted figure is to zoom in transition zone for each temperature. The red dot line is the magnetization curve of 2 K, indicating that the transition zone between 1 T and 2.2 T. While temperature increases to 300 K (light-green hollowed-triangle), not only the does $H_c$ drop to 1.2 T but the transition zone shrinks between 0.4 T and 1.2 T. In figure 3.2(b), the first derivative of magnetization presents that the magnetic peaks moves to weaker field as temperature warms up from 2 K to 300 K. While the temperature rises, the $H_c$ declines and the corresponding transition zone shrinks.

## 3.2 Pressure dependence of magnetoresistance

The anomalous magnetic peak in temperature dependence of MR is related to the phase transition from SS-FM and its corresponding $H_c$. Figure 3.2(c) shows the MR ratio ($MR = \frac{\rho(T)-\rho(0)}{\rho(0)}$) of $Au_2Mn$ measured by PPMS (Quantum Design, Inc.) at ambient pressure. The positive MR ratio at 2 K (red solid spot line) to 50 K (green solid diamond line) show that the magnetic peak at 1.8 T indicating SS-FM transition. The transition peak becomes a plateau above 160 K, and the negative MR ratio increases with increasing of temperature. $Au_2Mn$ is well-known as its giant

MR ratio, $7-10\%$ from 100 K to 300K. Although the MR ratio is relative lower, we confirmed the Neel temperature of Neel temperature and the spiral magnetic structure through magnetization and neutron scattering. The degree of disorder, type of disorder and grain boundaries would be possible reasons to change the MR. We set the maximum of this magnetic field-induced peak as the $H_c$ of the phase transition, which declines while temperature rises.

The temperature dependence of $H_c$ made by magnetization (red dot line) and MR (blue square) agree with each other below 160 K and kept the same tendency with 0.4 T above 200 K as shown in figure 3.2(d), which also indicates that MR could be a precursor to study the phase boundary under high pressure and low temperature. Above 160K, the correspondence between MR and magnetization becomes worse, possibly because the spin scattering is complicated by thermal excited magnons or phonons. According to high resolution powder diffraction pattern of $Au_2Mn$ under from 1 atm to 10 kbar, we notice that higher pressure compresses lattice constant of c-axis and induces smaller spin angle, $\phi$. The spiral spin magnetic structure might become distorted spiral and eventually turn into FM while pressure increases.

Tuning pressure dependence of the anomalous magnetic peak in MR and its related corresponding $H_c$ is conducive to mapping of pressure dependence of transition between SS-FM. The temperature dependence of MR in $Au_2Mn$ under 13.2 kbar at room temperature is presented in figure 3.3(a). The $H_c$ at 2 K drops to 1.2 T and the transition zones below 300 K shrink narrower and narrower due to higher and higher pressure. In figure 3.3(b), while pressure goes above 16.4 kbar at 2 K,

the magnetic peak is totally suppressed and MR totally turns negative. As pressure increases, the magnetic peaks gradually weaken and are finally suppressed. The transition zone of distorted spiral phase simultaneously narrows with increasing of pressure and temperature. The positive monotonic-increasing MR shows at based temperature and pressure lower than 10 kbar. Whenever temperature increases over 160 K or pressure rises above 10 kbar, we only observe negative MR and the transition peak become tiny.

Figure 3.3(c) presents the pressure dependence of MR in $Au_2Mn$ at 2 K, a hump at low-field region showing the spiral spin to ferromagnetic phase transition. If the area under magnetic-induced peak is proportional to magnetic ordering, magnetic ordering does gradually suppress by pressure. While pressure is below than 10 kbar, MR at 2 K in spiral spin phase keeps positive monotonic-increasing and shows the field-induced peak. When pressure is close to 16.4 kbar, the transition peak was suppressed and gradually changes to negative MR.

## 3.3 Absence of anomalous Hall effect

The ambiguity of absence of AHE and existence of anomalous MR captures our attentions. The linear normal Hall resistance dominates the Hall resistance under pressure and 2 K as shown in figure 3.3(d). Indeed, the carrier density decreases smoothly from $6.144 \times 10^{28} m^3$ to $5.447 \times 10^{28} m^3$ when pressure rises from 1 atm to 16.6 kbar. The longitudinal resistivity of $Au_2Mn$ decreases from 313.8 $n\Omega cm$ to 52.3 $n\Omega cm$( conductivity $\sigma_{xx}$ increases from 3.19 $\times 10^6 (\Omega cm)^{-1}$ to 19.1 $\times 10^6 (\Omega cm)^{-1}$

at 2 K and when pressure increases from 1 atm to 16.6 kbar. This is one to two order higher than the conductivity limit. Although Au2Mn becomes ferromagnetic above a critical pressure of 16.4 kbar, we do not see any qualitative changes in the Hall resistance as a function of pressure. In particular, we do not observe the expected AHE from itinerant FM under pressure. These large order of carrier density and conductivity minimized the scattering effect. Actually this region is also very challenging for experiment, as the magnetic field required for saturating magnetization and ordinary Hall effect is extremely large.

The high conductivity of Au2Mn appears to be the main reason why we do not detect the AHE. The Hall conductivity in the high-purity regime with high conductivity $\sigma_{xx} > 5 \times 10^5 (\Omega cm)^{-1}$ [42] is very challenging to investigate experimentally. In a high-conductivity region with a relatively long mean free path $l$, the ordinary Hall effect contribution dominates $\sigma_{xy}$ and is proportional to $l^2$, while skew scattering which leads to AHE is proportional to l. Indeed, the conductivity xx in our sample is larger than $10^6 (\Omega cm)^{-1}$ at low temperature, which is at least 1 order higher than the high-purity limit. The large carrier density and conductivity minimize the scattering, leading to the AHE. This high conductivity may also be related to the smaller giant MR ratio in our sample relative to literature values, which can be ascribed to larger grain size in our annealed samples.

Its $H_c$ and magnetic structure are identical below 50 K, here we display contour mapping of MR at 50 K in P-H plane as shown in figure 3.4(a). This red burst is relative large positive MR occurring magnetic transition from 1.8 T at ambient pressure and the corresponding transition zone represented as surrounding pink

region is compressed with pressure. The black dotted line is the $H_c$ determined by field-induced peak in MR, which indicates the second-order phase transition between SS-FM in pressure and field plane. Figure 3.4(b) shows SS-FM transition as red dot in the pressure versus temperature phase diagram of $Au_2Mn$. Another blue line showing Curie and Neel temperature [58], the kink around 18 kbar is determined by their intersection of two slope of pressure dependence of Neel and Curie temperature. The black dashed line shows the expected sharp phase boundary between SS-FM, which means this SS-FM phase transition is more sensitive to pressure than temperature.

At ambient pressure, Hamiltonian of $Au_2Mn$ is dominated by exchange energy proportional to $(\cos\phi)$ so the corresponding $H_c$ is roughly proportional to $(\cos\phi)$, which means that spin angle increases and $H_c$ decreases with temperature. However, spin angle at 10 kbar only expends three degrees from 80 K to 370 K and the $H_c$s decreases simultaneously. It is worth mentioning that thermal constraint ratio for lattice constant of c-axis at 10 kbar is only half of the ambient pressure value. Meanwhile, its pressure dependent thermal constraint ratio at 80 K is $6.23\times10^{-3}$ Å/ kbar, which is much more efficient than temperature variation. This also supports that Spiral structure collapses in a narrow pressure and broad temperature region. These external magnetic field and high pressure might induce the distorted spiral and break the inversion symmetry resulting in the competition between exchange energy, DM interaction including anisotropy and high order four-spin interaction terms. Therefore, the variation of spin angle of helimagnets becomes complicated.

## 3.4 Conclusion

We presented the SS-FM phase boundary by the means of MR and its corresponding critical pressure is 16.4 kbar below 50 K. Neutron diffraction confirmed that spin angle decreases from 45° to 36.18° while pressure increases to 10 kbar. The $H_c$ decreases as temperature rises at ambient pressure. This field-induced peak in MR is a great indicator of its SS-FM transition as a function of pressure. Its $H_c$ decreases, and the transition zone also simultaneously shrinks as pressure rises. Below 50 K, $H_c$ is 1.8 T at ambient pressure and drops to 0 T at 16.4 kbar.

# Chapter 4: Quantum oscillations from networked topological interfaces in $MoTe_2$

Layered TMDCs are promising hosts of electronic Weyl nodes and topological superconductivity. $MoTe_2$ is a promising case that hosts both noncentrosymmetric $T_d$ and centrosymmetric T' phases, both of which have been identified as topologically nontrivial. Applied pressure tunes the structural transition separating these phases to zero temperature, stabilizing a mixed $T_d$-T' matrix that entails a unique network of interfaces between the two non-trivial topological phases. Here, we show that this critical pressure range is characterized by unique coherent quantum oscillations, indicating that the change in topology between two phases give rise to a new topological interface state. A rare combination of topologically nontrivial electronic structures and locked-in transformation barriers leads to this counterintuitive situation wherein quantum oscillations can be observed in a structurally inhomogeneous material. These results open the possibility of stabilizing multiple topological superconducting phases.

## 4.1 Potential topological superconductivity in $T_d$-$MoTe_2$

Topologically protected electronic states at material interfaces are attractive because they cannot be destroyed by many types of perturbations. This feature of topological states has suggested an appealing strategy to achieve promising spintronics and quantum computation. The topological edge states lead to high electron mobility and long diffusion length, strong MR and efficient spin filtering. Topological superconductivity is such a protected quantum state, stable to local noise and disorder, that is being considered as a platform for decoherence-free, universal quantum computation [65–67]. An especially fruitful host of this exotic state is $MoTe_2$, which has had both its bulk orthorhombic $T_d$ phase, and hole-doped monolayer specimens identified as possible topological superconductors [30, 68, 70]. In addition, a topological superconducting phase was recently identified in sulfur-substituted samples, with novel $S_{+-}$-wave pairing [71]. These unusual superconductors all emerge from topologically nontrivial normal states: the $T_d$ phase has been identified as a type-II WSM [10, 72], whereas the monoclinic T' phase is predicted to be a higher-order topological material [73]. In this work, we demonstrate experimentally how pressure drives $MoTe_2$ into three different regimes having nontrivial electronic topology, all of which host superconductivity. These nontrivial states are particularly robust and survive under significant structural disorder.

## 4.2 Topology in $MoTe_2$

Recently, TMDCs have garnered great interest as topological materials, for example $WTe_2$ and $T_d$-$MoTe_2$, which have been identified as type-II WSM. Monolayer of T'-$MoTe_2$ and bulk T'-$MoTe_2$ were characterized as topological insulator and higher-order topological insulating phase [68, 73]. The type-II WSM $T_d$-$MoTe_2$ has been proposed as possible topological superconductivity for it topological state and superconductivity. To figure out its anomalous Hall effect and topological properties, noncentersymmetric $T_d$-$MoTe_2$ has been studied by tuning temperature, strain, magnetic field, chemical doping, pressure. This unique and novel electronic structure coincides with the abrupt enhancement of the superconducting temperature between two topological phases and might pioneer the topology and the unconventional superconductivity in $MoTe_2$ family.

Beyond the time reversal(TR) invariant topological superconductors, the TR breaking topological superconductors have also attracted plenty of interests because its potential application of topological quantum computation [66]. In $MoTe_2$ family, type-II WSM and topological insulator with unconventional superconductivity are great candidates for topological superconductivity [70, 85]. Here, we demonstrated an unusual Fermi surface from networked interface between $T_d$ and T' only found by mean of SdH oscillations. Remarkably, this unique electron structure only occurs cross the first-order structural transition between nonmagnetic $T_d$ and T' system. These evolution of nontrivial surface states in $MoTe_2$ might be a breakthrough to study the evolution of topological phases and the origin of its superconductivity.

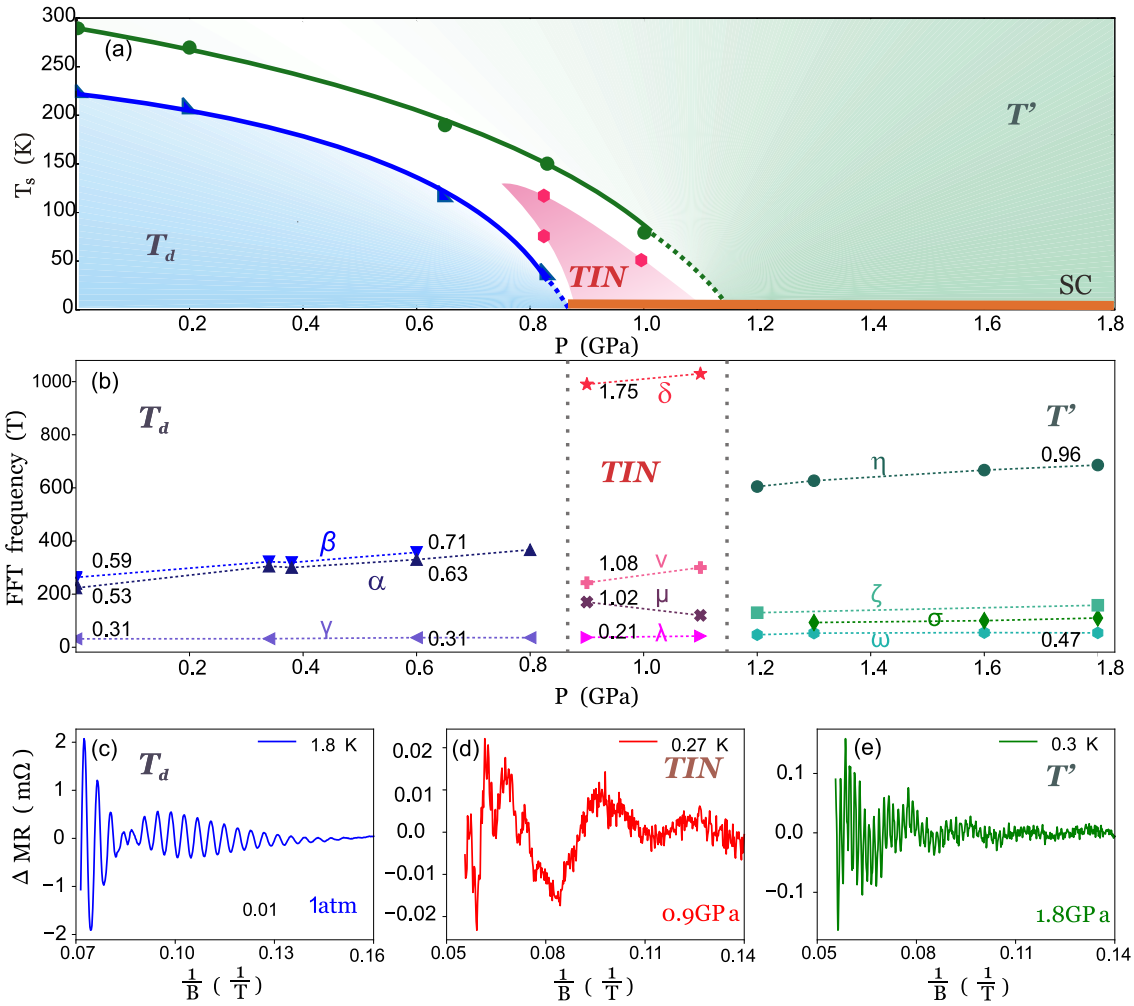


Figure 4.1: (a) Pressure-temperature phase diagram of $MoTe_2$. (b) Pressure dependence of FFT spectrum of oscillatory MR. The number index the effective mass close to their markers under different pressure. The representative SdH oscillations of $MoTe_2$ recorded (c) Weyl structure in $T_d$, (d) TIN, and (e) higher-order topology in T'.

## 4.3 Pressure dependence of structural transition in $MoTe_2$

The first-order structural transition separating the T' and $T_d$ phases in $MoTe_2$ has a distinct pressure dependence (figure 4.1(a)). At ambient pressure, the inversion-symmetric T' phase is stable at room temperature, only transforming into the non-centrosymmetric $T_d$ phase when cooled below roughly 250 K [30, 78]. Neutron diffraction allows the determination of the relative volume fraction of these phases under different conditions, which is not determinable through electrical transport measurements [78]. Neutron experiments were performed by Colin Heikes at NIST Center for Neutron Research. At constant pressure, a finite width in temperature separates full volume fraction T' and $T_d$ phases, shown as green and blue regions in figure 4.1(a). The temperature width of the transition increases at pressures higher than 0.8 GPa. At these pressures, a qualitatively new phenomenon emerges, namely that a roughly balanced mixture of the T' and $T_d$ phases stabilizes over an appreciable temperature range, shown in magenta in figure 4.1(a), and crucially, extends to the lowest measured temperatures. The existence of this unique frozen mixed-phase region implies that there is insufficient entropy at these suppressed temperatures for atoms to move to their lowest-energy configuration, which results from the unusual combination of having a first-order transition between two energetically nearly-degenerate structures (Fig. 4.1(a)).

## 4.4 Band structure study in $MoTe_2$ at ambient pressure

The mixed region serves as the foundation for a new type of electronic system in $MoTe_2$: a natural topological interface network (TIN). The existence of the TIN is exposed via the measurement of quantum oscillations in magnetoresistvity, known as SdH oscillations, whose frequency is proportional to the size of closed Fermi surfaces. In fact, SdH oscillations are evident in every region of the phase diagram; bulk $T_d$, bulk T', and the mixed region; the oscillation frequencies are summarized in Figure 4.1(b). Examples of the respective SdH oscillations are shown in figures 4.1(c)- 4.1(e). Vast differences in frequency and amplitude are immediately apparent between all three cases. These variations reflect the symmetry difference between $T_d$ and T' phases, and the completely distinct TIN state. Before addressing the TIN, we first focus on the more familiar $T_d$ and T' phases.

### 4.4.1 Electronic structure of $MoTe_2$ at ambient pressure

The basic components underlying the type-II WSM state of the $T_d$ phase are a large hole pocket centered on the Brillouin zone and two neighboring electron pockets along the $\Gamma - X$ direction [72,96]. The hole pocket is observed in ARPES, but is not apparent in SdH measurements. The most prominent SdH oscillations observed in the $T_d$ phase arise from orbits of the electron pocket. Figure 4.2(a) and figure 4.2(b) show background-subtracted MR and SdH oscillations at ambient pressure. As the FFT explicitly shows (figure 4.2(c)), the beating seen in figure 4.2(b) is due to two nearly-identical frequencies, $F_\alpha = 240.5$ T and $F_\beta = 258$ T, the result of spin-orbit

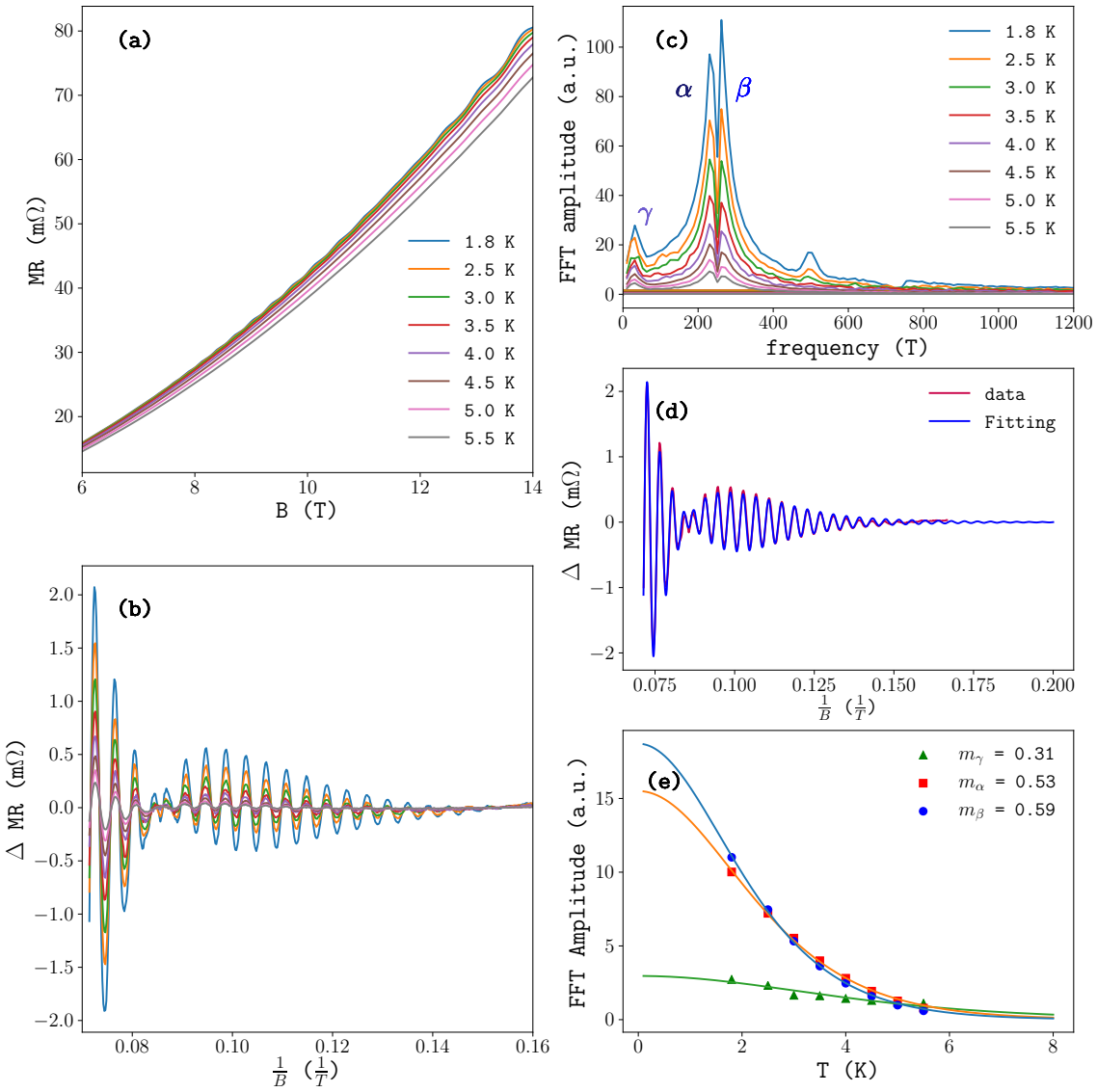


Figure 4.2: (a) The longitudinal MR of the bulk $T_d$-$MoTe_2$ measured at ambient pressure with magnetic field parallel to c axis. (b) The corresponding SdH oscillations were observed by second-order polynomial background subtraction of normal MR. (c) The FFT spectrum show three Fermi surfaces with oscillation frequencies at $F_\gamma = 32.5$ T, $F_\alpha = 240.5$ T and $F_\beta = 258$ T. (d) Best fitting of SdH oscillations at 1.8 K. (e) The effective masses are obtained by the temperature dependence of LK fitting.

band splitting allowed by the lack of inversion symmetry. A third, low frequency $F_\gamma$ = 32.5 T corresponds to the handle part of the electron pockets in density functional calculations.

Modeling of the SdH oscillations yields a remarkably good fit (figure 4.2(d)) to the experimental SdH oscillations, allowing the reliable determination of the phase shift for each frequency (all parameters in Table 4.8 ). In fact, all of the oscillations feature a nontrivial Berry's phase, consistent with a Weyl topology. The effective band masses are light, and slightly less than previously reported [82,83] as shown in figure 4.2(f). As a function of pressure, the electron pockets increase modestly in size due to lattice compression, but the nontrivial phase shift is maintained throughout the $T_d$ phase. The 1.8 K SdH oscillations data were fitted by the multiple bands of three dimensional LK formula and got the corresponding Berry phases, ($\phi_\gamma = \pi$, $\phi_\alpha = 0.88\pi$, and $\phi_\beta = 0.88\pi$), indicating that $T_d$-$MoTe_2$ at ambient pressure is a possible three dimensional topological semimetal with 3D topological phase shift, $\delta = -\frac{1}{8}$ [80,81] for electron pocket in equation (2.15).

### 4.4.2 Angle dependence of Shubnikov-de Haas oscillations

Here we show angular MR measured at ambient pressure and 1.8 K when magnetic field rotates from $c$ axis to $b$ axis as the insert figure in Fig. 4.3(a). The beat frequency increases with the increasing of $\theta$, the angle between magnetic field and $c$ axis as shown in Fig. 4.3(b). The cross section areas of two electron bands, $F_\alpha$ and $F_\beta$ slightly increase with increasing of $\theta$ at 1.8 K.

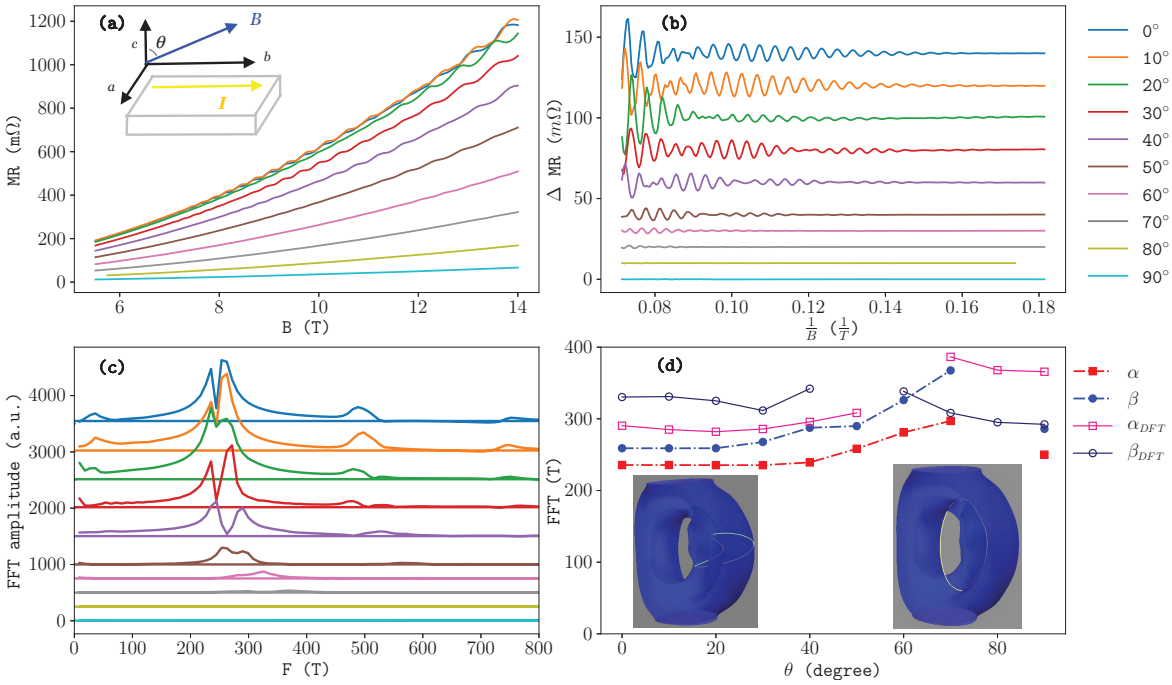


Figure 4.3: (a) The angular longitudinal MR of the bulk $MoTe_2$ sample measured at ambient pressure and 1.8 K when magnetic field moves from $c$ axis to $b$ axis. (b) The SdH oscillations. (c) The FFT spectrum of SdH oscillations as a function of the frequency. (d) The extracted angle-dependence of the oscillation frequencies along with DFT-calculations.

In order to understand this weak angle dependence of the SdH oscillations, we have calculated the extreme orbits as the magnetic field is turned as in our measurements. The results are summarized in Figure 4.3(d). The calculated angle dependence is also very weak up to 40°. Due to spin-orbit splitting, near 40°-60°, the calculated orbit frequency is suddenly almost doubled with a resulted complicated orbit which involves both the cup surface and the interior of the mug-shape surface. After this sudden increase, a new orbit is obtained as the interior of the mug-shape surface (see Fig. 4.3(d) which has, interestingly almost the same magnitude as original frequency. Hence, the overall angle dependence is very weak, as we

found in our measurements. Because of the two Fermi surface near each other due to spin-orbit splitting and complicated orbit shape, it is unlikely for the electrons to oscillate around such a complicated orbit coherently and therefore one may expect small intensity, which is consistent with decreasing intensity in our measurements.

The angle dependence of SdH oscillations at ambient pressure maps out two 3D topological Fermi surfaces of two electron pockets from multiband model applied with LK fit in equation (2.15). From the raw data of MR at ambient pressure, we subtract the second order polynomial background. The FFT spectra shows three bands, $F_\gamma = 32.5$ T, $F_\alpha = 240.5$ T, $F_\beta = 258.0$ T and their second and third order harmonic oscillations. The higher harmonic peaks of $F_\alpha$ and $F_\beta$ indicate high quality and homogeneity of the single crystal. The 1.8 K SdH oscillations data were fitted by the multiple bands of three dimensional LK formula and got the corresponding Berry phases, ($\phi_\gamma = \pi$, $\phi_\alpha = 0.88\pi$, and $\phi_\beta = 0.88\pi$), indicating that $T_d$-$MoTe_2$ at ambient pressure is a possible three dimensional topological semimetal with 3D topological phase shift, $\delta = -\frac{1}{8}$ [79–81] for electron pocket in equation (2.15).

## 4.5 Fermiology in $T_d$-$MoTe_2$ under pressure

The pressure dependent phase diagram features the frozen first-order structural transition zone in temperature. The T' phase with lattice inversion symmetry is stable at room temperature and ambient pressure and turned into noncentrosymmetric $T_d$ phase, the candidate of type-II WSM, at based temperature. One in which the system displays filamentary superconductivity in a $T_d$ ground state, and

another where the T' phase is preferred at lowest temperature, and superconductivity is a bulk phenomenon [78]. Breaking the lattice inversion symmetry leads two different band structure in bulk $T_d$-$MoTe_2$ and bulk T'-$MoTe_2$ and their nontrivial Berry's phases support their individual topological system, WSM and higher-order topology [73]. The electronic band structure of bulk T' and bulk $T_d$ slightly and continuously expand and keep the similar trends with increasing of pressure. In figure 4.4(c), the Fermi surfaces at 0.6 GPa in bulk $T_d$-$MoTe_2$ phase gently expand with pressure and maintain the nontrivial Berry's phase and topological phase shift, $\delta = -\frac{1}{8}$. The stable nontrivial Berry's phase of electron pocket and the continuity and similar tendency of electronic structure below 0.6 GPa suggest that Weyl structure might be maintained below hydrostatic pressure 0.6 GPa in bulk $T_d$-$MoTe_2$.

Because the T' phase of $MoTe_2$ does not persist to low temperature, quantum oscillations are inaccessible at ambient pressure, making it difficult to assess whether its band structure is topologically nontrivial. Applied pressure makes it possible for the first time to measure the topological band structure in the bulk T' phase ( figure 4.4(i)). Throughout the T' phase, instead of two frequencies, a single frequency $F_\eta$ is observed, increasing from 600 T to 700 T over the measured range of pressure (Figure 4.1(b)). The T' phase has been predicted to harbor an unusual type of nontrivial topological state called a higher-order topological insulator [73]. Although ARPES is ambiguous about whether the T' phase is topologically nontrivial [96], it is clear in the SdH oscillations that a nontrivial $\pi$ Berry's phase exists also in the T' phase (Table 4.8). Measuring the SdH oscillations at different field angles under pressure could offer a detailed confirmation of the correspondence of the electronic

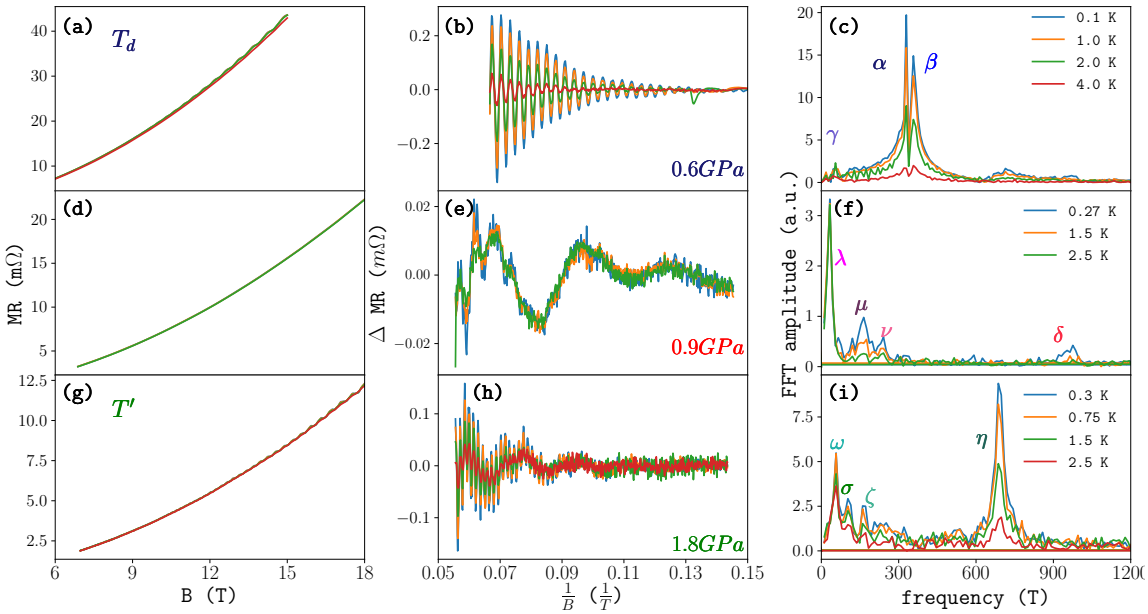


Figure 4.4: Temperature dependence of the MR of $MoTe_2$ measured at (a) $T_d$-$MoTe_2$, (d) surface state, and (g) T'-$MoTe_2$. Their corresponding SdH oscillations are shown in (b), (e) and (h). FFT spectrum at (c) $T_d$ and (i) T' shows that cross-section of their Fermi surfaces expand with increasing of pressure.

structure of the T' phase to that of the higher-order topological insulator will be possible. This find also raises the fascinating possibility that superconductivity in the T' phase is also inherently topologically nontrivial.

In T'-$MoTe_2$, two main bands $F_\omega$ = 43 T and $F_\eta$ = 605 T pop at 1.2 GPa and smoothly increase to 54 T and 689 T with their corresponding effective mass 0.47 $m_e$ and 0.96 $m_e$, and nontrivial Berry phases at 1.8 GPa. Two subtle bands at $F_\sigma$ = 110 T and $F_\zeta$ = 158 T could only be identified above higher magnetic field above 14 T. The stable tendency and continuity of band structure, effective mass, enhancement of oscillations signal and expansions of Fermi surfaces of charge carrier pockets indicate that electronic structure of bulk monoclinic phase extends

with pressure. Bulk T' has been predicted as higher-order topological insulator if it were bulk-insulating with existence of pairs of hinge states. If the SOC is neglected, the T' would become the nodal-line semimetal with $Z_2$ invariant monopole nodal-line [73]. To advanced study in potential topological superconductivity and the evolution of these surface states between T' and $T_d$, pressure would be an appropriate approach to tune the system. It is really helpful to scratch the band structure and 3D Fermi surface of this higher-order topology candidate in bulk T'-$MoTe_2$ by the mean of angle dependence of quantum oscillations under pressure as the refined measurement.

## 4.6 Density Functional theory in $T_d$-$MoTe_2$ and T'-$MoTe_2$

In this section, we discuss the details of our first-principles electronic structure calculations of $MoTe_2$ as a function of pressure for both $1T'$- and $T_d$-phases, respectively.

### 4.6.1 Effect of Electron Correlations on the Band Structure and Fermi Surface of $MoTe_2$

Recent studies [102, 103] found that electron correlations are essential for a precise description of the bulk electronic structure of $T_d$-$MoTe_2$ as revealed by ARPES [102] and the angular dependence of the Fermi surface by quantum oscillations experiments [103]. Hence, in our study we adopted DFT+U scheme to describe the electron correlations within the Mo $4d$-states. The overall best agree-

ment with ARPES and quantum oscillations data is obtained for U = 3 eV [102,103], which was also used in our calculations in this study.

Figures 4.5 and 4.6 show the effect of the Hubbard U (taken as 3.0 eV) on the band structure and the Weyl-points in the $T_d$- and $1T'$-phases of $MoTe_2$, respectively. We note that the biggest effect is to shift the bands near Y-point so that we do have any electron pocket at the Fermi surface as shown in Fig.4.7. The other main effect is to lower some of the bands further below Fermi level which does not have any effect on the Fermi surface. It is important to note that the Weyl point near Fermi level remains unaffected with the inclusion of the Hubbard correlation term $U$ in our calculations. However, as we shall see below, including U is critical to explain the pressure dependence of the quantum oscillations frequencies that we have measured in this study.

In our calculations, besides the Hubbard term $U$, there are other parameters such as lattice constants and atomic positions that we need to determine. One way is to use experimental parameters or to determine them self consistently within the DFT+U structural optimization at any given pressure. Figure 4.7 shows the Fermi surface of $T_d$- and $1T'$ phases of $MoTe_2$ for both experimental and DFT optimized structures with and without electron correlation effects (i.e. U). We note that the Fermi surface is very sensitive to the lattice parameters and the atomic positions. Our optimized lattice parameters and atomic positions are within 1% the experimental values as shown in Tables 4.1 and 4.2. The biggest variation is in the a-axis for the $T_d$ phase and it's 1.4%. Despite this excellent agreement between experiment and calculations, the difference in the Fermi surface between experimental and

| Experimental Structure<br>a=3.46464 Å, b=6.30716 Å | | c=13.84310 Å | $90^o$ $90^o$ $90^o$ |
|---|---|---|---|
| Mo | 0.000000000 | 0.606100004 | 0.497243989 |
| Mo | 0.500000000 | 0.393899996 | 0.997243989 |
| Mo | 0.000000000 | 0.029300001 | 0.014242000 |
| Mo | 0.500000000 | 0.970700018 | 0.514242010 |
| Te | 0.000000000 | 0.865899961 | 0.653545972 |
| Te | 0.500000000 | 0.134100020 | 0.153545972 |
| Te | 0.000000000 | 0.641099962 | 0.112019999 |
| Te | 0.500000000 | 0.358900000 | 0.612019999 |
| Te | 0.000000000 | 0.287699989 | 0.857258999 |
| Te | 0.500000000 | 0.712299993 | 0.357259033 |
| Te | 0.000000000 | 0.214699994 | 0.401510016 |
| Te | 0.500000000 | 0.785300043 | 0.901509982 |
| DFT+U Optimized Structure<br>a=3.51242 Å, b=6.33797 Å | | c=13.80214 Å | $90^o$ $90^o$ $90^o$ |
| Mo | 0.000000000 | 0.596570039 | 0.499028659 |
| Mo | 0.500000000 | 0.403429961 | 0.999028659 |
| Mo | 0.000000000 | 0.043489108 | 0.012956972 |
| Mo | 0.500000000 | 0.956510911 | 0.512956982 |
| Te | 0.000000000 | 0.854056153 | 0.653752430 |
| Te | 0.500000000 | 0.145943828 | 0.153752430 |
| Te | 0.000000000 | 0.649980885 | 0.109058347 |
| Te | 0.500000000 | 0.350019077 | 0.609058347 |
| Te | 0.000000000 | 0.302836245 | 0.858321051 |
| Te | 0.500000000 | 0.697163737 | 0.358321085 |
| Te | 0.000000000 | 0.203297619 | 0.402703515 |
| Te | 0.500000000 | 0.796702418 | 0.902703481 |

Table 4.1: Lattice parameters and fractional atomic positions of $T_d$ $MoTe_2$ ($Pmn2_1$).

| Experimental Structure a=6.3281 Å, b= 3.4770 Å | | c=13.021 Å | $90^o$ $93.882^o$ $90^o$ |
|---|---|---|---|
| Mo | 0.182799990 | 0.250000000 | 0.008300000 |
| Mo | 0.817199966 | 0.750000017 | 0.991700002 |
| Mo | 0.319399986 | 0.750000017 | 0.506199997 |
| Mo | 0.680599966 | 0.250000000 | 0.493799979 |
| Te | 0.587999989 | 0.250000000 | 0.106399996 |
| Te | 0.411999994 | 0.750000017 | 0.893599938 |
| Te | 0.096600004 | 0.750000017 | 0.149299988 |
| Te | 0.903399993 | 0.250000000 | 0.850699971 |
| Te | 0.557100023 | 0.750000017 | 0.351300002 |
| Te | 0.442900004 | 0.250000000 | 0.648699974 |
| Te | 0.056299998 | 0.250000000 | 0.395299983 |
| Te | 0.943700035 | 0.750000017 | 0.604699925 |
| DFT+U Optimized Structure a=6.3422 Å, b=3.5106 Å | | c=13.8292 Å | $90^o$ $93.8907^o$ $90^o$ |
| Mo | 0.181248302 | 0.250000000 | 0.007402050 |
| Mo | 0.818751654 | 0.750000017 | 0.992597952 |
| Mo | 0.320793055 | 0.750000017 | 0.506405748 |
| Mo | 0.679206897 | 0.250000000 | 0.493594228 |
| Te | 0.589309059 | 0.250000000 | 0.103197530 |
| Te | 0.410690924 | 0.750000017 | 0.896802404 |
| Te | 0.097660263 | 0.750000017 | 0.147835158 |
| Te | 0.902339734 | 0.250000000 | 0.852164801 |
| Te | 0.559332448 | 0.750000017 | 0.352629203 |
| Te | 0.440667579 | 0.250000000 | 0.647370773 |
| Te | 0.057121356 | 0.250000000 | 0.396415521 |
| Te | 0.942878677 | 0.750000017 | 0.603584387 |

Table 4.2: Lattice parameters and fractional atomic positions of $T'$ $MoTe_2$ ($P2_1/m$).

the optimized structures is quite large. In order to be self-consistent, we decided to use optimized lattice parameters and atomic positions for a given pressure as obtained from our DFT+U calculations. In this way, we are able to determine the pressure dependence of the Fermi Surface and determine the quantum oscillations orbits and frequencies. The only free-parameter in our DFT+U calculations is the Hubbard U, which was shown to be around U = 3 eV for $MoTe_2$ to match the ARPES measurements as well as the angle dependence of the quantum oscillations frequencies [102, 103].

### 4.6.2 Pressure Dependence of the Fermi Surface and Quantum Oscillations

In this section, we present our results related to the pressure dependence of the Fermi surface and quantum oscillations orbits as a function of applied pressure for both phases of $MoTe_2$. In both phases, we have similar Fermi surface and orbits which are summarized in Figure 4.8. Near Γ point, we have a square-box like Fermi surface (red). The orbit around this Fermi surface is shown in Fig.4.8 as 's'. Then, we have an electron-like Fermi surface with a shape of a coffee mug (light blue). This shape has basically three types of extremal orbits as shown in the Figure 4.8. We label the orbits at the opening as 'op'. Then, the orbit near the handle like surface as "h". And, finally we have the orbits near the cup like denoted as 'c'. As we shall see below, this orbit is sensitive to pressure and we identified this orbit as in our quantum oscillations measurements. Finally, we have small pocket of squashed elliptical surface (dark blue), which we call it 'e' orbit. In the case of $T_d$-phase, these

orbits have two counterparts due to SO-splitting.

We have carried out full structure optimization at a given pressure and then calculate the Fermi surface over a dense k-grid to determine the orbit frequencies using skeaf code [105]. Our results are summarized in Tables 4.3 and 4.4. We note that most of the orbit-frequencies do not change much with applied pressure but the cup-orbit increases with increasing pressure. As discussed in the main text, the slope of the frequency increase with pressure is in excellent agreement with the observed shifts in the experimental measurements. Hence, we identified this orbit as the one probed in our quantum oscillations measurements.

| Orbits | 0 kbar | 2 kbar | 4 kbar | 6 kbar | 8 kbar | 10 kbar | 12 kbar | 14 kbar | 16 kbar | 18 kbar | 20 kbar |
|---|---|---|---|---|---|---|---|---|---|---|---|
| h1 | 0.14 | 0.15 | 0.15 | 0.155 | 0.16 | 0.163 | 0.167 | 0.17 | 0.174 | 0.17 | 0.17 |
| h2 | 0.1 | 0.10 | 0.10 | 0.11 | 0.11 | 0.104 | 0.11 | 0.12 | 0.116 | 0.12 | 0.18 |
| op1 | 0.235 | 0.23 | 0.21 | 0.22 | 0.21 | 0.22 | 0.21 | 0.21 | 0.210 | 0.204 | 0.19 |
| op2 | 0.22 | 0.22 | 0.21 | 0.207 | 0.20 | 0.20 | 0.19 | 0.19 | 0.196 | 0.186 | 0.18 |
| c1 | 0.33 | 0.37 | 0.405 | 0.44 | 0.470 | 0.506 | 0.57 | 0.57 | 0.601 | 0.653 | 0.684 |
| c2 | 0.294 | 0.33 | 0.36 | 0.395 | 0.426 | 0.455 | 0.51 | 0.51 | 0.542 | 0.600 | 0.626 |
| e1 | 0.08 | 0.06 | 0.06 | 0.055 | 0.06 | 0.05 | 0.046 | 0.045 | 0.05 | 0.056 | 0.04 |
| e1 | 0.08 | 0.08 | 0.08 | 0.07 | 0.07 | 0.07 | 0.06 | 0.06 | 0.06 | 0.056 | 0.06 |
| s1 | 1.90 | 1.9 | 1.98 | 2.01 | 2.04 | 2.07 | 2.10 | 2.13 | 2.15 | 2.21 | 0.26-2.24 |
| s2 | 2.16 | 2.2 | 2.24 | 2.27 | 2.30 | 2.33 | 2.36 | 2.39 | 2.41 | 2.42 | 0.29-2.5 |

Table 4.3: Quantum oscillations Frequencies (kT) in $T_d$-$MoTe_2$ phase as a function of pressure (kbar). The orbit labels are defined in Figure 4.8.

The topology of the Fermi surface pretty much stays the same with applied pressure up to 16 kbar (i.e. 1.6 GPa). Due to smaller lattice constants the band overlap gets larger with increasing pressure which in turn increases the orbit frequencies.

| Orbits | 0 kbar | 2 kbar | 4 kbar | 6 kbar | 8 kbar | 10 kbar | 12 kbar | 14 kbar | 16 kbar | 18 kbar | 20 kbar |
|---|---|---|---|---|---|---|---|---|---|---|---|
| h | 0.14 | 0.132 | 0.136 | 0.14 | 0.144 | 0.147 | 0.150 | 0.151 | 0.152 | 0.154 | 0.153 |
| op | 0.33 | 0.29 | 0.293 | 0.291 | 0.294 | 0.294 | 0.295 | 0.291 | 0.291 | 0.292 | 0.292 |
| c | 0.26 | 0.36 | 0.392 | 0.425 | 0.457 | 0.489 | 0.520 | 0.556 | 0.5854 | 0.616 | 0.646 |
| s | 1.896 | 2.027 | 2.030 | 2.10 | 2.130 | 2.160 | 2.185 | 2.245 | 0.24-2.25 | 0.47-2.27 | 0.63-2.3 |

Table 4.4: Quantum oscillations Frequencies (kT) in $T'$-$MoTe_2$ phase as a function of pressure (kbar). The orbit labels are defined in Figure 4.8.

However at pressures larger than 1.6 GPa, due to strong inter-layer interaction, the hole-band with the square box shape starts to have an opening at the top/bottom of the box-surface as shown in Figure 4.9. For comparison, we show Fermi Surface at 20 kbar for both phases in Fig. 4.9 but we note that at these pressures, the main phase is the $1T'$ phase where we have inversion symmetry. Interestingly the new orbit at the top of the hole-square band has about the same oscillatory frequency as the cup-orbit near 0.65 kT.

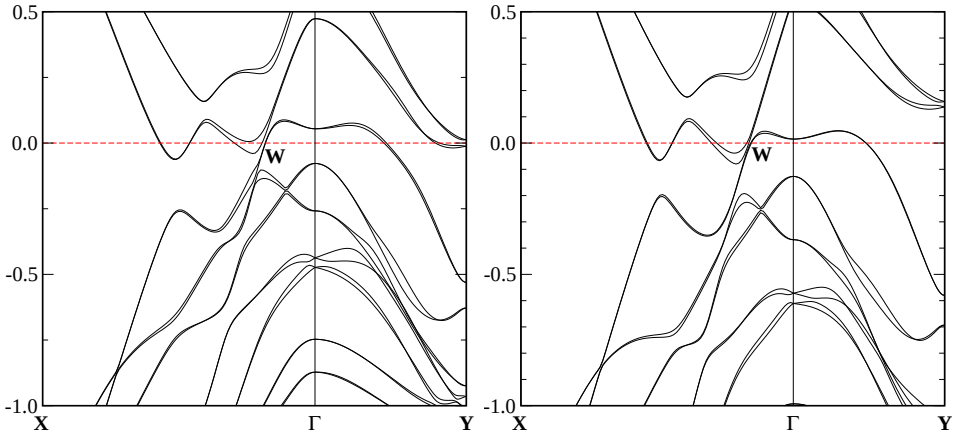


Figure 4.5: Electronic band structure without (left) and with Hubbard $U$ (right), showing the effect of the electron correlations on the band structure. The main effect is to shift up the bands near Fermi level around Y-point while the Weyl point (shown as "w") was not effected by $U$. The small splitting of the bands are due to Spin-Orbit (SO) coupling and the lack of inversion symmetry in the $T_d$ phase.

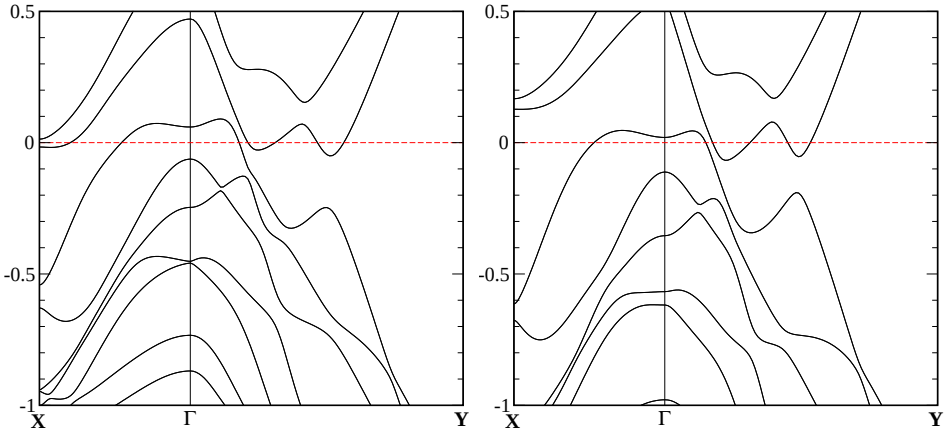


Figure 4.6: Band structure with (right) and without $U$ term (left) in $1T'$-phase of bulk $MoTe_2$. The effect of SO coupling is still important even though it does not split the bands (but shift them around to effect the Fermi Surface).

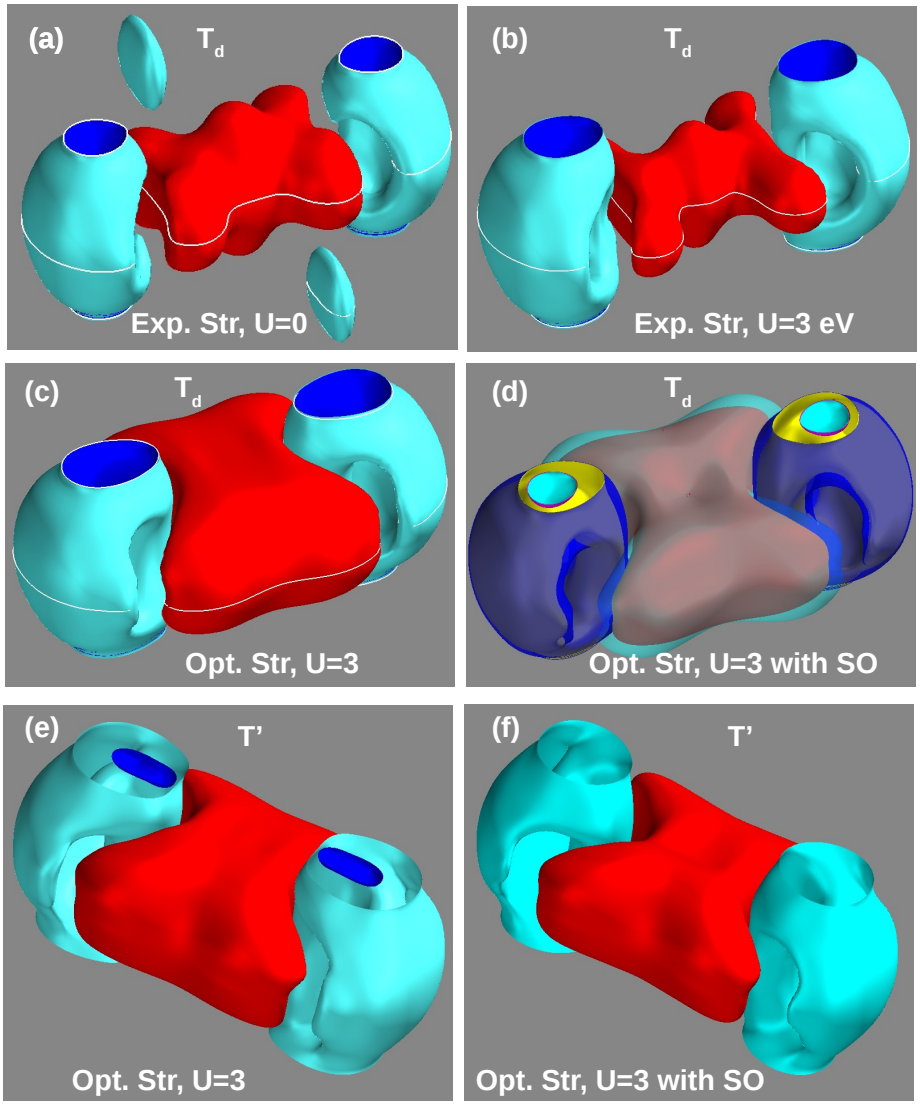


Figure 4.7: Fermi surface plots of $MoTe_2$ for various cases; (a) Experimental structure and without U term; (b) Experimental structure with U=3 eV; main effect of which is to remove the states near Y-point; (c) Fully optimized structure with U=3 eV. Note that it is quite different than one from experimental structure shown in b. (d) Fully optimized structure with U=3 eV and also with SOC. The main effect of SOC is to shrink and expand the surfaces so that they split; Note the significant shrinkage of the surface shown as dark blue color; (e-f) shows the Fermi surface in the $1T'$ phase with optimized structure and U=3 eV. Due to inversion symmetry, there is no splitting of the Fermi surface in $1T'$-phase but the bands are shifted around and the resulting Fermi surface is different. Also note that the small electron packet (dark blue in (e)) is removed with the inclusion of SOC (f).

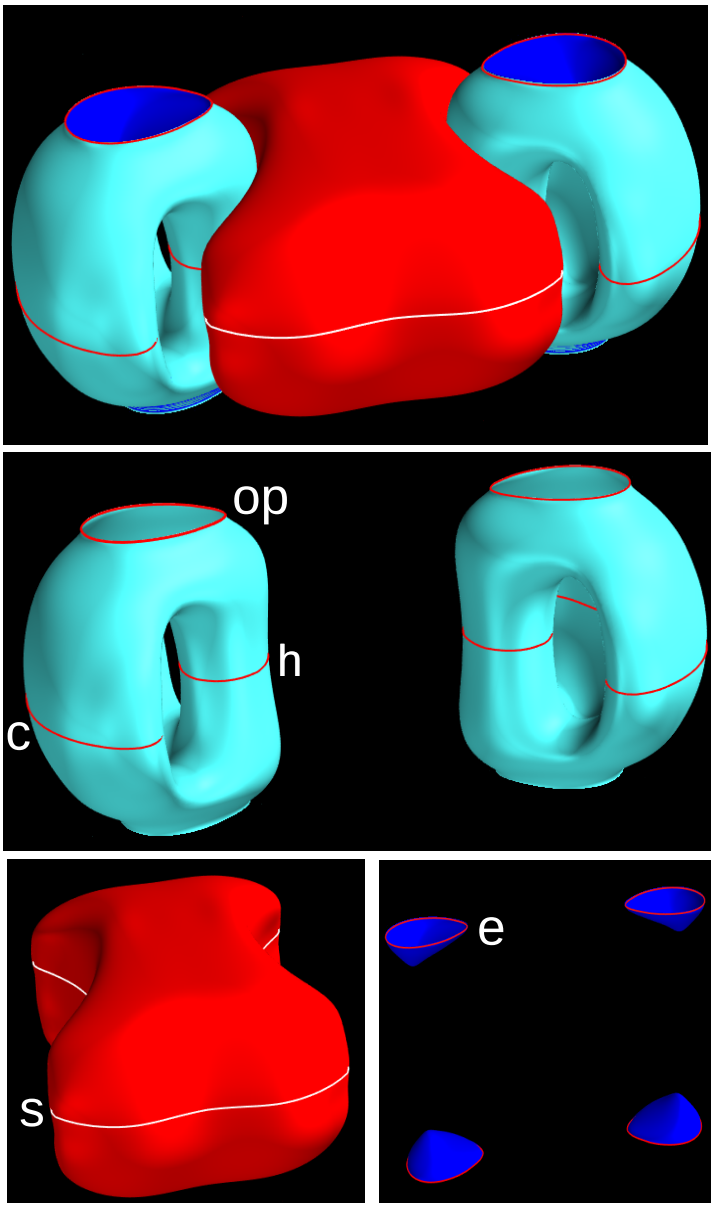


Figure 4.8: Top panel shows the main shape of the Fermi surface in both phase of $MoTe_2$ which consists of three types of bands; The red one is a **s**quare like box shape with mainly hole-character. We denote the orbits around this surface as "**s**". The main portion of the Fermi surface is electron-like and has the coffee mug shape (light blue). This shape supports three possible extreme orbits as shown as "**op**" (which is at the **op**ening of the surface), as "**h**" which is the orbit around the **h**andle like shape, and "**c**" which is the orbit around the **c**up portion of the Coffee Mug-shape Fermi surface. Interestingly, this cup-like shape is the most sensitive to the pressure and the frequency of this orbit increases with increasing pressure, in excellent agreement with our measurements. Finally, we have small pocket of electron Fermi surface (dark blue), which has the **e**llipsoidal shape and therefore denoted as "**e**".

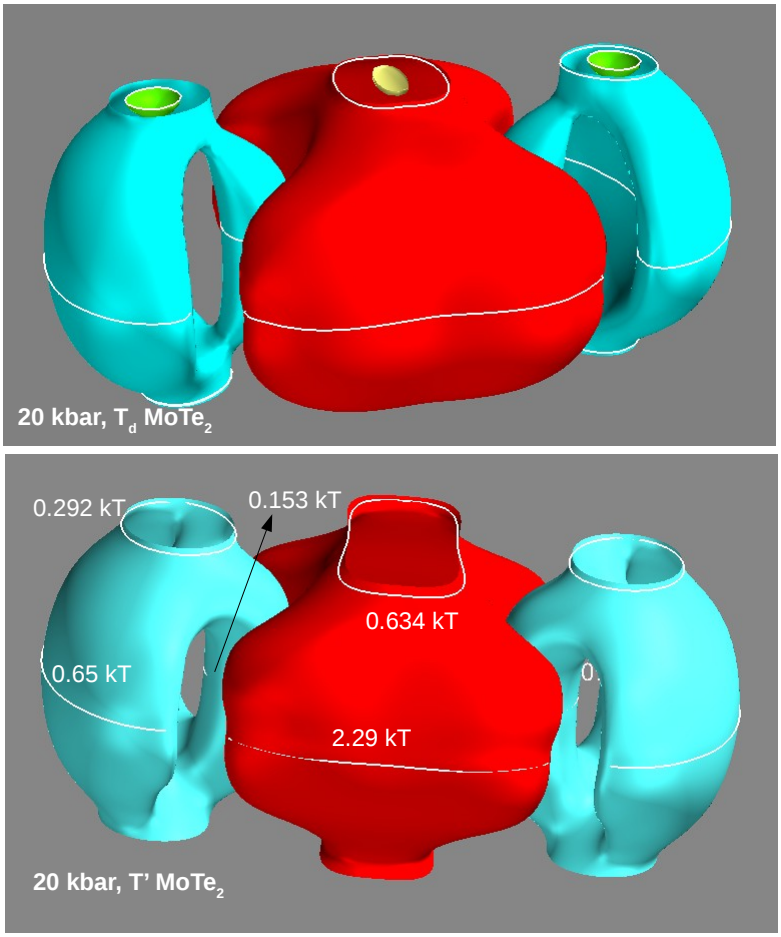


Figure 4.9: Fermi surface of $MoTe_2$ at 20 kbar pressure for $T_d$ phase (top) and for $1T'$-phase (bottom). Note that the center square-box like Fermi surface start to have opening at the top with orbit frequencies near 0.65 kT, which is similar to the cup-site orbit.

## 4.7 Networked topological interfaces in $MoTe_2$

The mixed region exists in a range of pressures and temperatures between the bulk $T_d$ and T' phases (figure 4.1(a)). Attempts to identify other structural phases or ordered superstructures via neutron diffraction measurements were unsuccessful. Naively, it might be expected that any measured SdH oscillations in the mixed region would consist of a superposition of $T_d$ and T' signals. However, both of these appear to be absent. A natural explanation is that increased scattering typically weakens

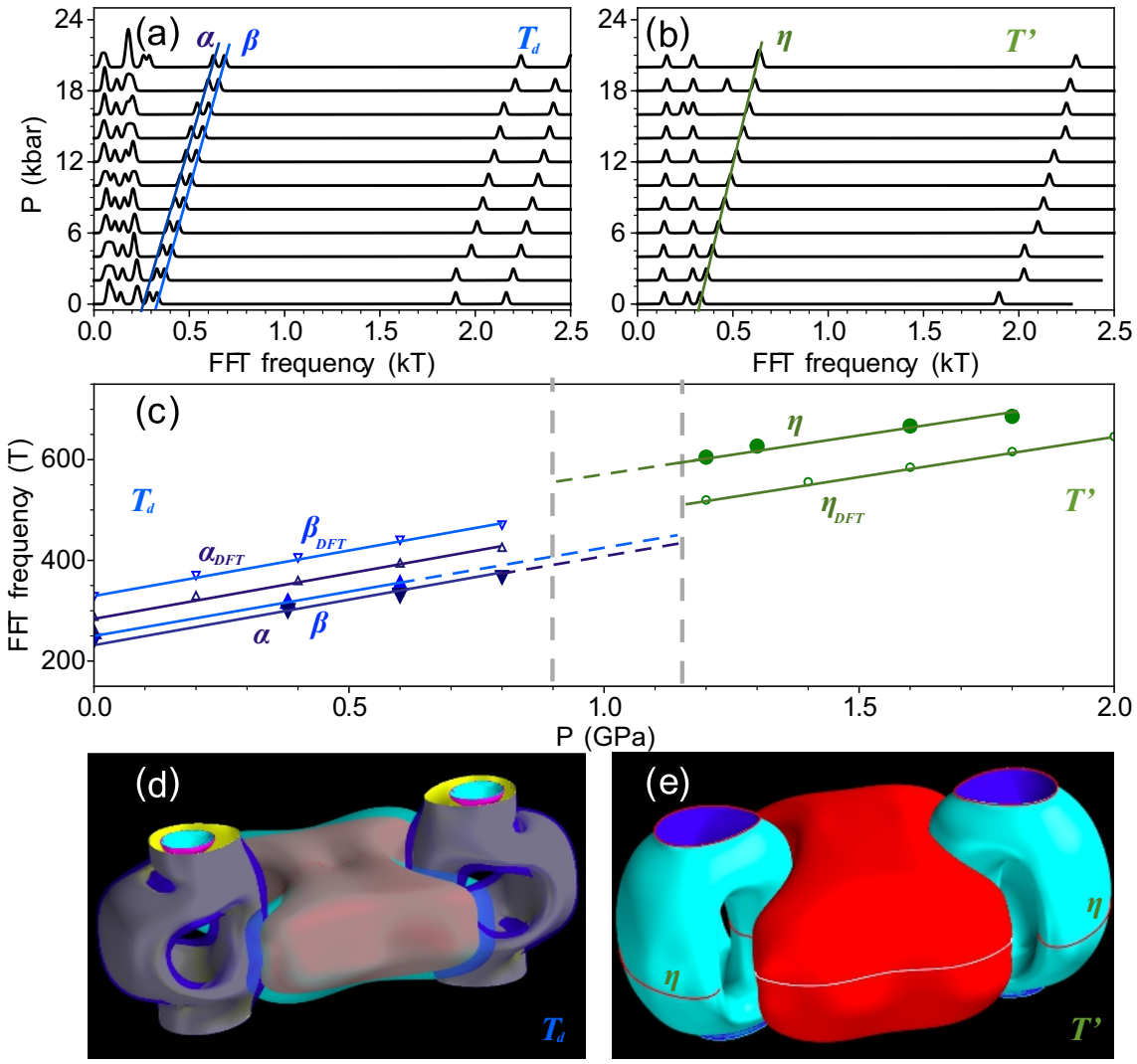


Figure 4.10: (a,b) Calculated in-plane quantum oscillations frequencies of the $T_d$ and T' phases, showing that the SdH oscillations arising from the electron pockets, increase with increasing pressure in both phases. (c) A comparison between calculated and measured frequencies shows excellent quantitative agreement. (d, e) Calculated Fermi Surfaces of the $T_d$ and T' phases

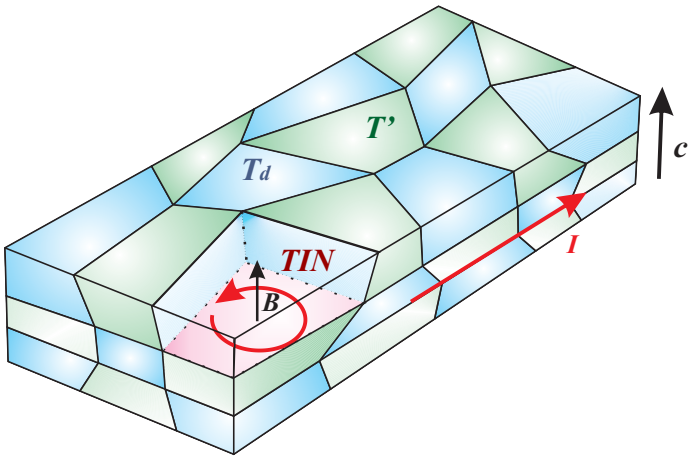


Figure 4.11: Schematic of natural topological interface network (TIN). The quantum oscillations of bulk $T_d$ and T' were limited within the local grain boundaries and suppressed by the disorders. The networked interfaces between multilayer of two topological structures as WSM and higher-order of topology can effectively screen the interaction between adjacent layers of TMDCs MX2, inducing the novel topologically protected edge states. The relative weak and coherent signals are robust under the small system perturbation and only come from the connected interfaces. This TIN heterostructure can parametrically increase the number of edge channels and thus significantly enhance the signal-to-noise ratio in practical applications.

quantum oscillations. The mixed region is heterogeneous and sufficiently disordered that SdH oscillations from both the $T_d$ and T' phases are suppressed. In light of this, it is completely unexpected that a new set of unique SdH oscillations appears (Fig. 4.4(a)). Aside from the presence of new frequencies corresponding to new Fermi surfaces, a new band structure in the mixed region is inferred from a change in effective mass and much weaker oscillation amplitude relative to bulk $T_d$ and T', as shown in fig.4.4(f). In addition to the survival of these electronic states in the presence of disorder, the SdH oscillations from the mixed region feature nontrivial Berry's phases (Table 1), features typical of a topologically protected state. This explains why no new structural phases characterize the mixed region - the topological states are surface states of the bulk phases, in this case, their interfaces.

Essential to the TIN state is the coexistence of two bulk phases with different topological invariants. The mixed region provides a natural framework for this coexistence. As the $T_d$ phase is a WSM, its surface Fermi arcs have been much studied. However, the TIN differs potentially in one key aspect, namely, that unlike the vacuum, which is topologically trivial, the T' phase is topologically nontrivial. In order for edge states to exist at the interfaces, there must be a change in topology between $T_d$ and T' phases, as might be expected of the WSM and HOTI states. No calculations exist to describe this interface, and in general, interfaces between two different topological bulk states have not received much theoretical attention. Our discovery suggests that this is a rich area for future exploration.

In the TIN, due to the layered structure of both $T_d$ and T' phases, the *ab* plane is preserved, and the largest grain boundaries fall along the *ab* plane, which is the orientation probed by the SdH measurements. This picture is schematically illustrated in Fig 4.7. A conductive path across the sample spans multiple interfaces allows coherent oscillations to be measured in transport measurements. Whereas measurements of transport coherence often requires laboratory-engineered structures, in the case of $MoTe_2$, nature provides a naturally generated heterostructure in the mixed region. Recently, the twisted bilayer graphene become superconducting and TEM indicates that topological protected states exist in the breaking inversion symmetric system by the twisted AB stacking. The band structure become dramatically different within 1 degree and flat bands showing at the second magic angle. This unconventional superconducting state is a very possible topological superconducting state and twisted bilayer TMDCs without the inversion symmetry are proposed to

find the similar effects. The increasing effective mass of $F_\eta$ emerges the flat band in the TIN and all nontrvial states in the TIN breaking the inversion symmetry might be induced from natural fine twisted interfaces. To further study in the band structure and the related edge states in TIN, artificial multilayered superstructure tuning with magic angle would be a good approach.

## 4.8 Conclusion

The pressure-tuned progression of different topological states raises the exciting possibility of studying several different types of topological superconductivity. Whereas superconductivity of the $T_d$ WSM has received most attention, it is filamentary, and it has only recently been realized that bulk superconductivity exists in the T' phase. The topological classification of this superconducting state has not yet been explored. Additionally, the exact nature of the interfacial electronic states is a rich new direction of study, including possible new classes of superconductor. As we have demonstrated that the TIN can be readily stabilized, we can look forward to making use of these states in future topological quantum computation schemes and other applications.

Our results pioneer three topological band structure that the unique pressure induced nontrivial surface state is enhanced in abundant networked interfaces and is robust under disordered system between two topologically protected phases T'-$MoTe_2$ and $T_d$-$MoTe_2$. The positive chemical pressure associated with disorder system is helpful to confirm the sources of nontrivial surface states in the interfaces and approachable for ARPES and STM. $MoTe_2$ under pressure potentially hold-

ing three topological phases and evolution of topological superconducting phases deserves further study for its possible quantum computing application. The co-existence of two structures system could be a much approachable for search edge state and might possible to artificial fabricate the similar structures for quantum computing application.

| P(GPa) | F(T) | $A_k(10^{-5}nm^{-2})$ | $k(10^{-3}nm^{-1})$ | E(meV) | $T_D$(K) | $\tau$(ps) | $\mu(cm^2/v_S)$ | $l$(nm) | $m^*(m_e)$ | $\phi(\pi)$ |
|---|---|---|---|---|---|---|---|---|---|---|
| | | | | | | | | | | |
| ~0 | 32.5 | 309.91 | 31.41 | 6.07 | 19.81 | 0.06 | 348.30 | 3.85 | 0.31 | 1.00 |
| | 240.5 | 2293.37 | 85.44 | 26.19 | 4.99 | 0.25 | 809.90 | 24.38 | 0.53 | 0.88 |
| | 258.0 | 2460.25 | 88.49 | 25.18 | 6.14 | 0.19 | 557.77 | 17.39 | 0.59 | 0.88 |
| | | | | | | | | | | |
| 0.6 | 35.0 | 333.75 | 32.59 | 6.73 | 18.20 | 0.08 | 456.46 | 5.24 | 0.30 | 0.96 |
| | 330.3 | 3149.69 | 100.13 | 26.85 | 4.16 | 0.29 | 720.95 | 25.44 | 0.71 | 0.88 |
| | 355.0 | 3385.22 | 103.81 | 32.52 | 9.16 | 0.13 | 372.41 | 13.62 | 0.63 | 0.88 |
| | | | | | | | | | | |
| 0.9 | 37.0 | 352.83 | 33.51 | 10.34 | 7.91 | 0.19 | 1635.88 | 19.32 | 0.21 | 0.95 |
| | 170.0 | 1621.09 | 71.83 | 9.65 | 5.12 | 0.25 | 436.44 | 11.05 | 1.02 | 0.95 |
| | 245.0 | 2336.28 | 86.24 | 13.07 | 2.97 | 0.39 | 629.26 | 19.12 | 1.08 | 0.87 |
| | 966.0 | 9211.62 | 171.24 | 31.85 | 3.54 | 0.35 | 350.83 | 21.17 | 1.75 | 1.02 |
| | | | | | | | | | | |
| 1.8 | 53.0 | 505.40 | 40.11 | 6.45 | 3.48 | 0.36 | 1324.20 | 18.71 | 0.47 | 0.97 |
| | 110.0 | 1048.94 | 57.78 | 11.18 | 8.48 | 0.14 | 438.90 | 8.94 | 0.57 | 0.76 |
| | 158.0 | 1506.66 | 69.25 | 11.23 | 6.88 | 0.18 | 381.37 | 9.31 | 0.81 | 1.19 |
| | 690.0 | 6579.73 | 144.72 | 41.13 | 3.94 | 0.31 | 558.02 | 28.46 | 0.97 | 1.11 |

Table 4.5: The fitting parameters of LK formula in $MoTe_2$ under pressure P.

# Chapter 5: Summary

## 5.1 Summary of Main Results

For the SS materials, $Au_2Mn$, the corresponding spin angle and Q vector decreases with pressure and become ferromagntic-like with pressure. The phase boundary between SS and FM phases in $Au_2Mn$ at a critical pressure of 16.4 kbar, is determined by neutron diffraction, magnetization, and MR measurements. The temperature-dependent critical field at a given pressure is accompanied by a peak in MR and a step in magnetization. The critical field decreases with increasing temperature and pressure. Separating the SS phase and FM by the critical pressure coincides with the disappearance of the MR peak, where the critical field goes to zero. The notable absence of an AHE in the ferromagnetic phase is attributable to the high conductivity of this material. This is a well-known experimental obstacle to overcome in the future.

For topological materials, $MoTe_2$, we demonstrate the (I) pressure dependence of superconducting transition, (II) structural transition as a function of pressure, (III) band structure of $T_d$, T' and TIN phases, and (IV) the discovery of new TIN phase. In $T_d$-$MoTe_2$, superconductor behaves as a filamentary superconductor for its partial volume of superconductor below 0.8 Gpa and turns into a bulk superconductor in T'. The superconducting temperature in $T_d$-$MoTe_2$ increases under pres-

sure with different linear slope compared with T'-$MoTe_2$. Its structural transition from centrosymmetric monoclinic structure, T' to noncentrosymmetric, orthorhombic phase, $T_d$ is gradually suppressed from 260 K at ambient pressure to 70 K at 0.82 Gpa. Through SdH oscillations and ab initio calculations, we observe the band structure of $T_d$, T' and TIN. The nontrivial Berry's phase and the phase shift in $T_d$ suggest that $T_d$-$MoTe_2$ has two three-dimensional Fermi surfaces from electron pockets due to SOC, which agrees with our Fermi surface models by DFT. These results support that $T_d$-$MoTe_2$ is a type-II WSM. The Fermi surface in the T' phase resembles that of the $T_d$ phase, although the inversion symmetry of the T' phase removes the SOC of the bands contributing to the electron pockets. The nontrivial Berry's phase in T' is in good agreement with the prediction of higher-order topology in T'-$MoTe_2$. In $T_d$ and T', their band structure qualitatively are consistent with our DFT calculation except for the discontinuity due to the first-order structure transition. Surprisingly, there exists a novel discovery of the new TIN phase in the mixed T' and $T_d$ region. Only $T_d$ and T' phases coexist in this phase without any evidence for the new structure or superlattice through neutron scattering. Its different band structure, effective mass, and much weaker oscillation are distinct from the $T_d$ and T' phases. The disappearances of $T_d$ and T' in quantum oscillation imply that disorder destroys the coherent oscillation signals from bulk $T_d$ and bulk T'. Such an appearance of TIN phase shows that TIN survives under disorder and implies that the nontrivial topology in TIN is protected from the disorder in this system. The interfacial signal has been amplified by suppressing the bulk $T_d$ and bulk T' SdH oscillations through grain boundary scattering, and increasing the in-

terface volume. Our discovery suggests that this is a rich area for future exploration and exploitation.

## 5.2 Future Directions

There are several potential directions to further study in TIN phase. The initial question is to seek the pressure dependence of carrier density in $MoTe_2$ by its Hall effect. Possible AHE might indicate the quantum topological transition in TIN region. Both edge states and domain boundaries of the interfaces between $T_d$ and T' might be observed through transmission electron microscopy. Through S-doped system ($MoTe_{2-x}S_x$ ), chemical pressure enhances higher superconducting temperature and is possible to stabilize the surface states in TIN phase at ambient pressure. Therefore, ARPES and scanning tunneling microscope could be sensitive to observe its nontrivial surface states. Its corresponding superconducting temperature is simultaneously enhanced with chemical pressure, hence, we may study the Chern numbers and the different types of superconducting transitions through thermal conductivity and spin-polarized scanning tunneling microscope.

Furthermore, the thickness of crystal is related to the total numbers of interfaces in TIN. The thicker the crystal the more it is expected to enhance the TIN signal. This property is totally opposite compared with other topological systems, preferred monolayer materials. To clarify the disorder and SOC effects on topological superconductors, $MoTe_2$ is a good candidate that harbors different types of topologies and superconductors associated with breaking and conservation of lattice inversion symmetry and time reversal symmetry.

# Appendix A: Data analysis of SdH oscillation in $MoT2_2$

## A.1 Uncertainty and correlation plots in LK fits above 0.6 Gpa

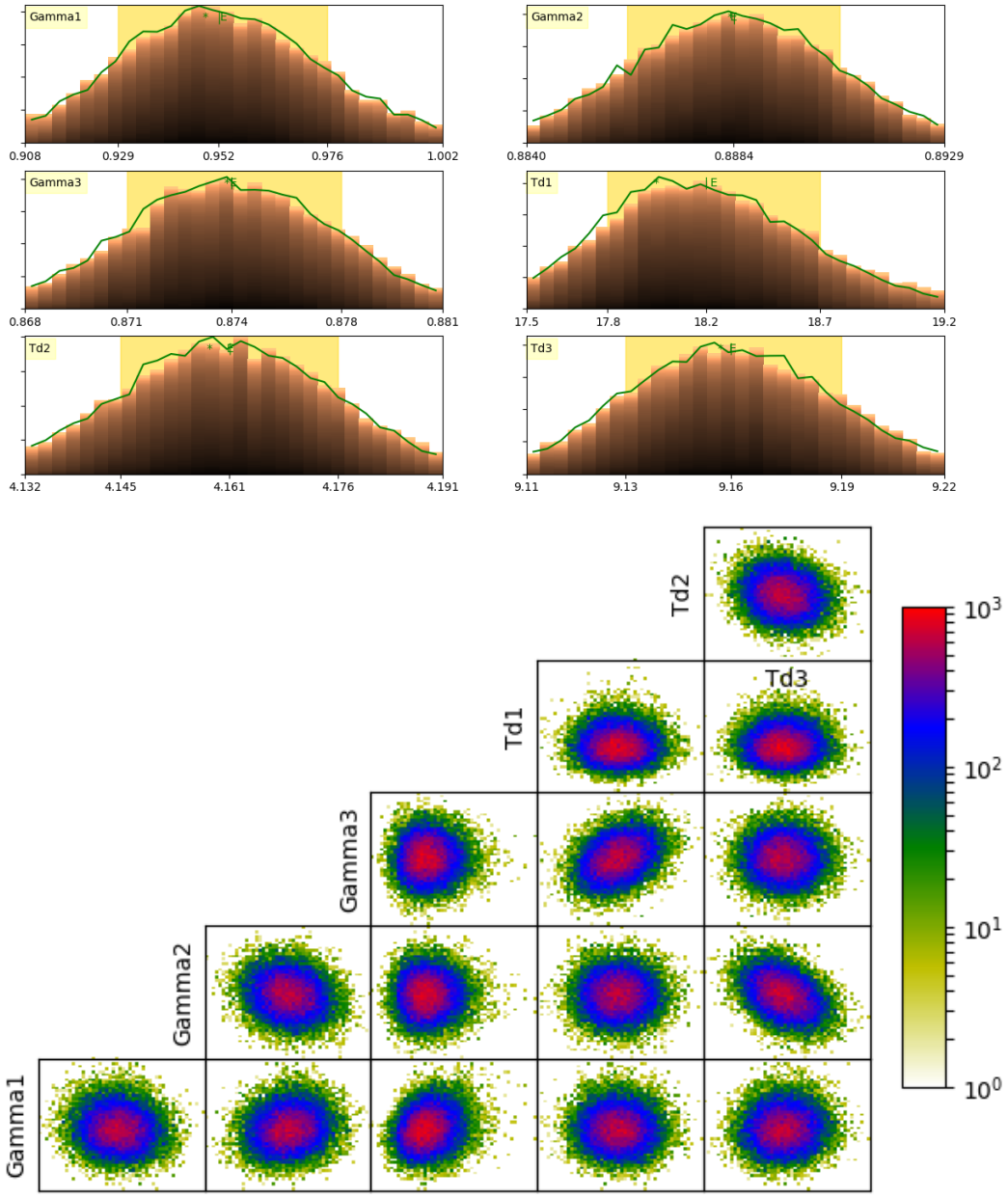


Figure A.1: This is the (a) uncertainty of LK formula fitting in $MoTe_2$ made at 0.1 K and 0.6 GPa. The Berry's phase of $F_\gamma$, $F_\alpha$, and $F_\beta$ are $(0.95 \pm 0.05)\pi$, $(0.89 \pm 0.01)\pi$ and $(0.87 \pm 0.01)\pi$. (b) The 2D correlation plots between each two parameters in our fitting formulas.

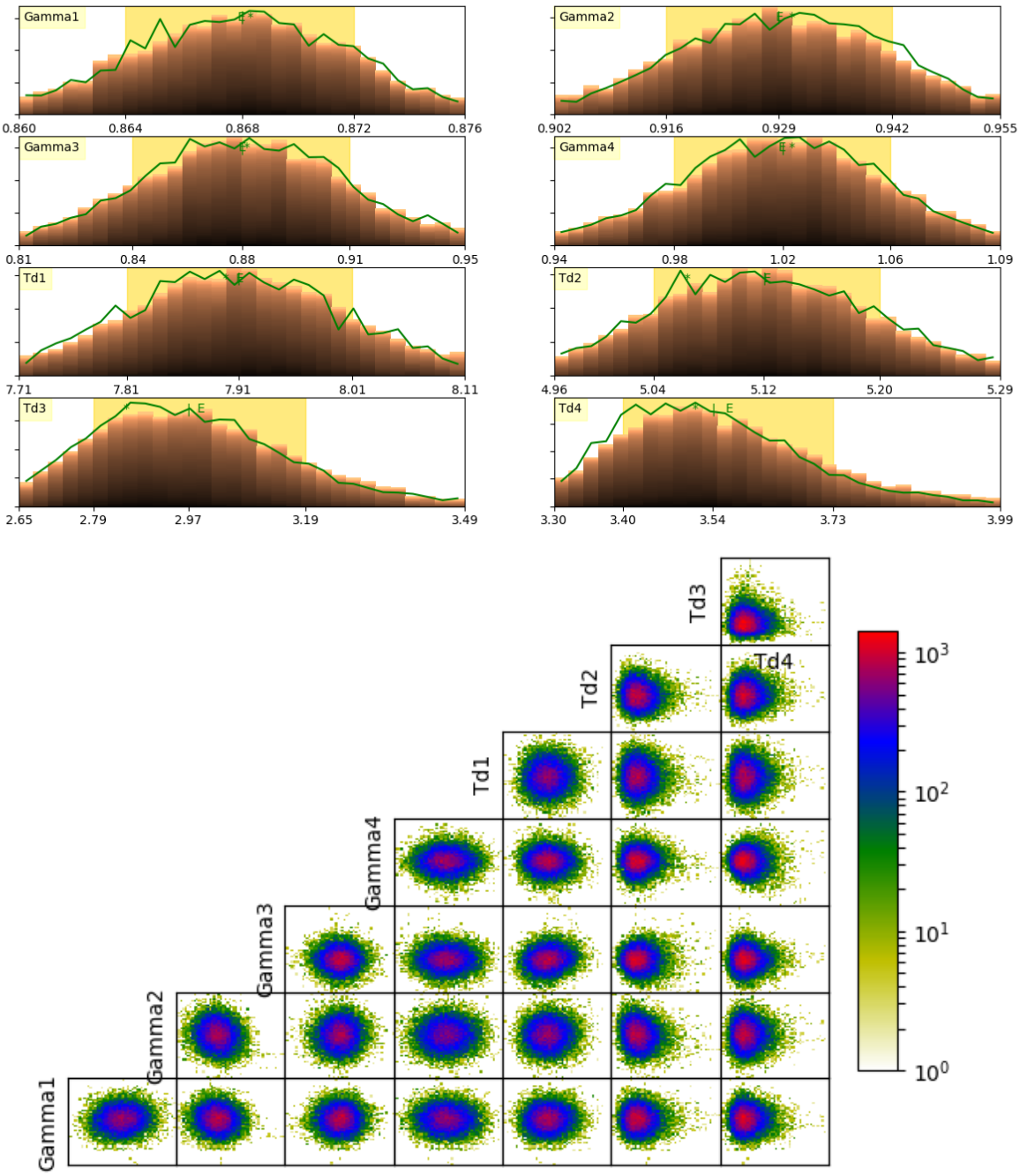


Figure A.2: This is the (a) uncertainty of Lifshitz-Kosevich formula fitting in $MoTe_2$ made at 0.27 K and 0.9 GPa. The Berry's phase of $F_\lambda$, $F_\mu$, $F_\nu$, and $F_\delta$ are $(0.87 \pm 0.01)\pi$, $(0.93 \pm 0.02)\pi$, $(0.88 \pm 0.07)\pi$, and $(1.02 \pm 0.08)\pi$. (b) The 2D correlation plots between each two parameters in our fitting formulas.

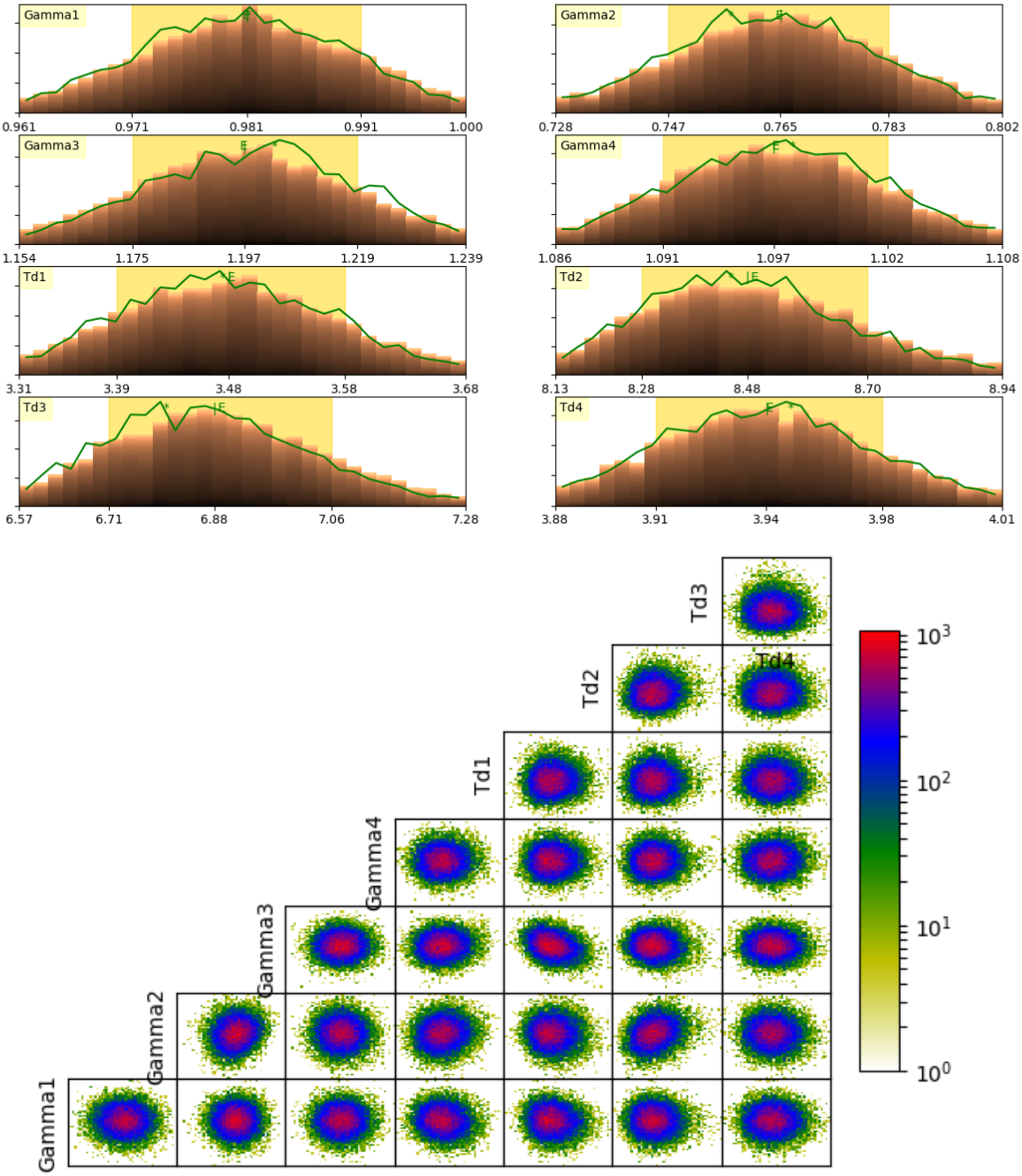


Figure A.3: This is the (a) uncertainty of Lifshitz-Kosevich formula fitting in $MoTe_2$ made at 0.3 K and 1.8 GPa. The Berry's phase of $F_\lambda$, $F_\mu$, $F_\nu$, and $F_\delta$ are $(0.98 \pm 0.02)\pi$, $(0.77 \pm 0.03)\pi$, $(1.20 \pm 0.03)\pi$, and $(1.10 \pm 0.01)\pi$. (b) The 2D correlation plots between each two parameters in the fitting formula.

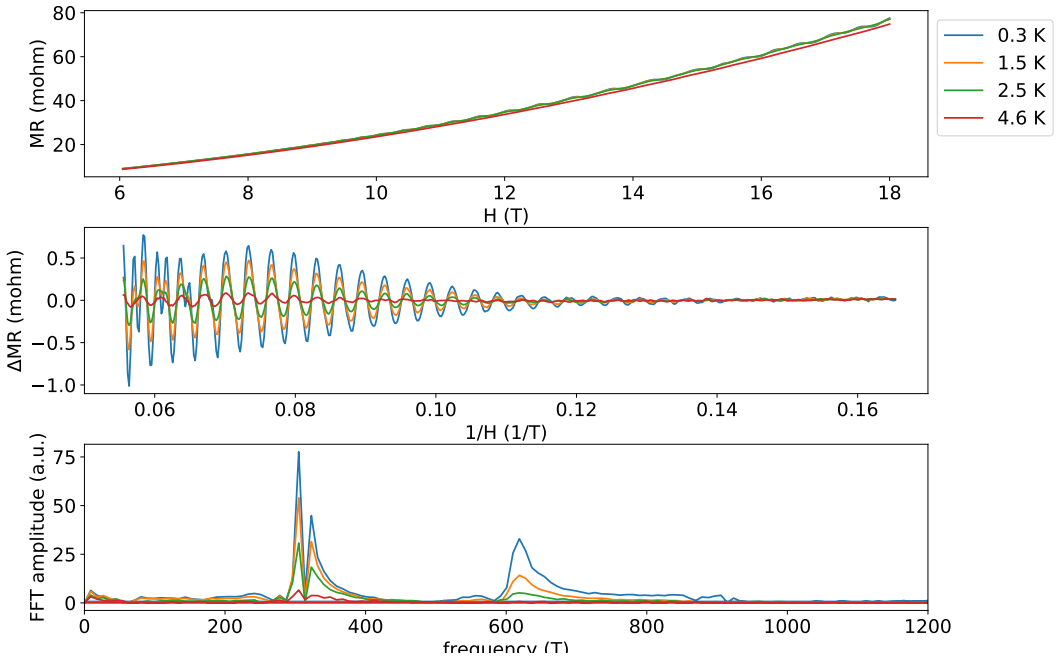


Figure A.4: (a) The longitudinal MR, (b) SdH oscillations and (c) its FFT of the bulk $MoTe_2$ sample measured at 0.34 GPa with magnetic field parallel to $c$ axis.

## A.2 SdH oscillation in $MoTe_2$ under pressure

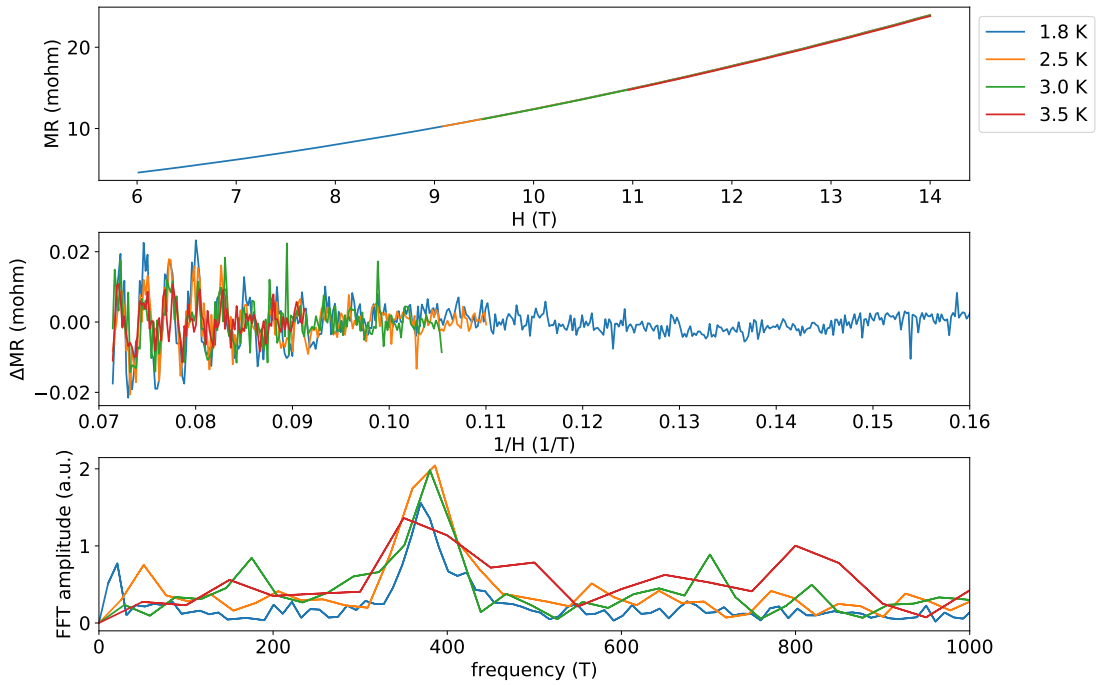


Figure A.5: (a) The longitudinal MR, (b) SdH oscillations and (c) its FFT of the bulk $MoTe_2$ sample measured at 0.8 GPa with magnetic field parallel to $c$ axis.

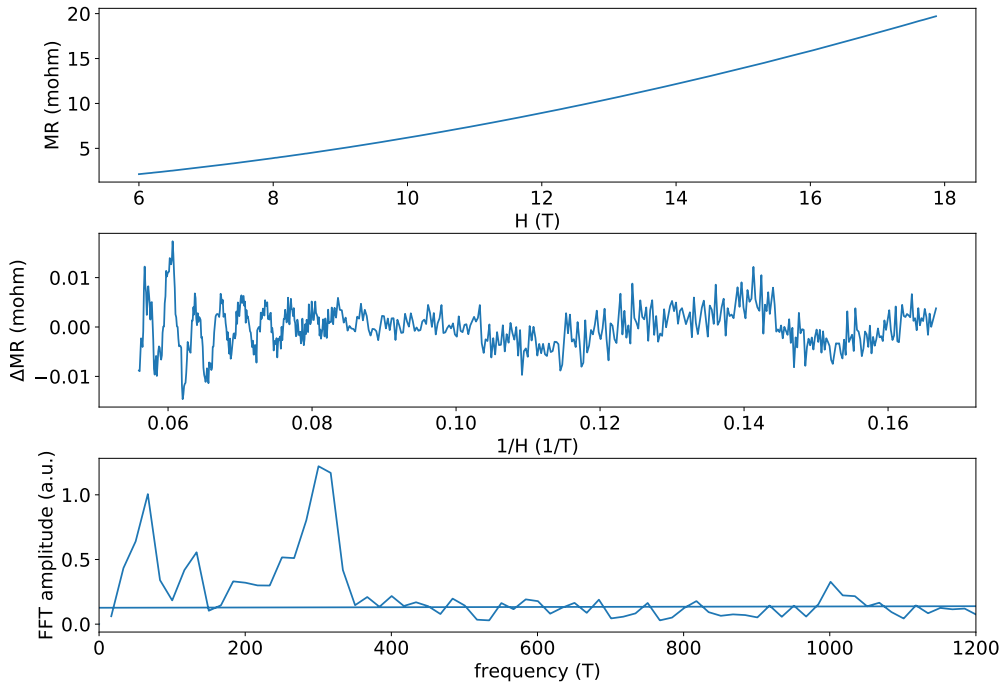


Figure A.6: (a) The longitudinal MR, (b) SdH oscillations and (c) its FFT of the bulk $MoTe_2$ sample measured at 0.3 K and 1.1 GPa with magnetic field parallel to $c$ axis.

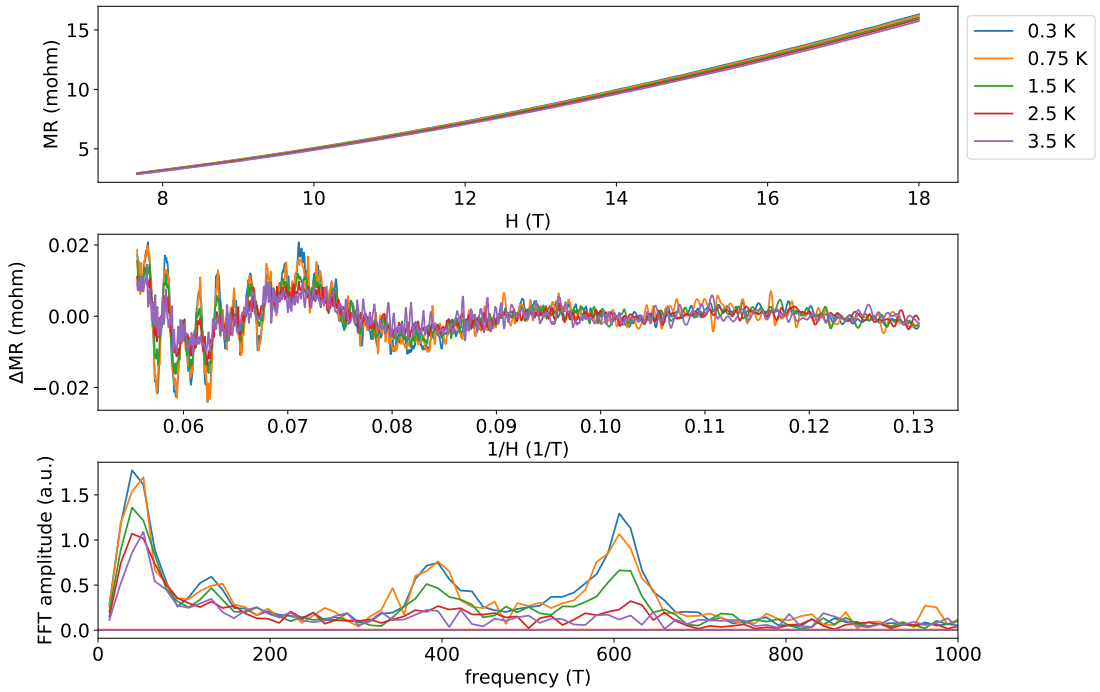


Figure A.7: (a) The longitudinal MR, (b) SdH oscillations and (c) its FFT of the bulk $MoTe_2$ sample measured at 1.2 GPa with magnetic field parallel to $c$ axis.

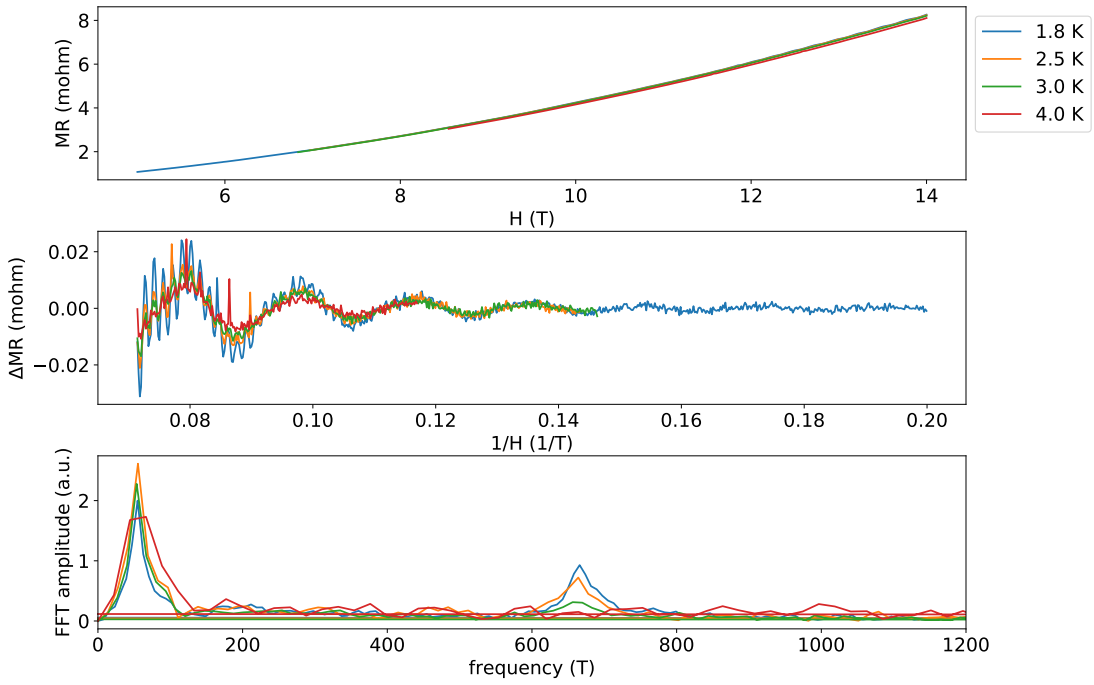


Figure A.8: (a) The longitudinal MR, (b) SdH oscillations and (c) its FFT of the bulk $MoTe_2$ sample measured at 1.3 GPa with magnetic field parallel to $c$ axis.

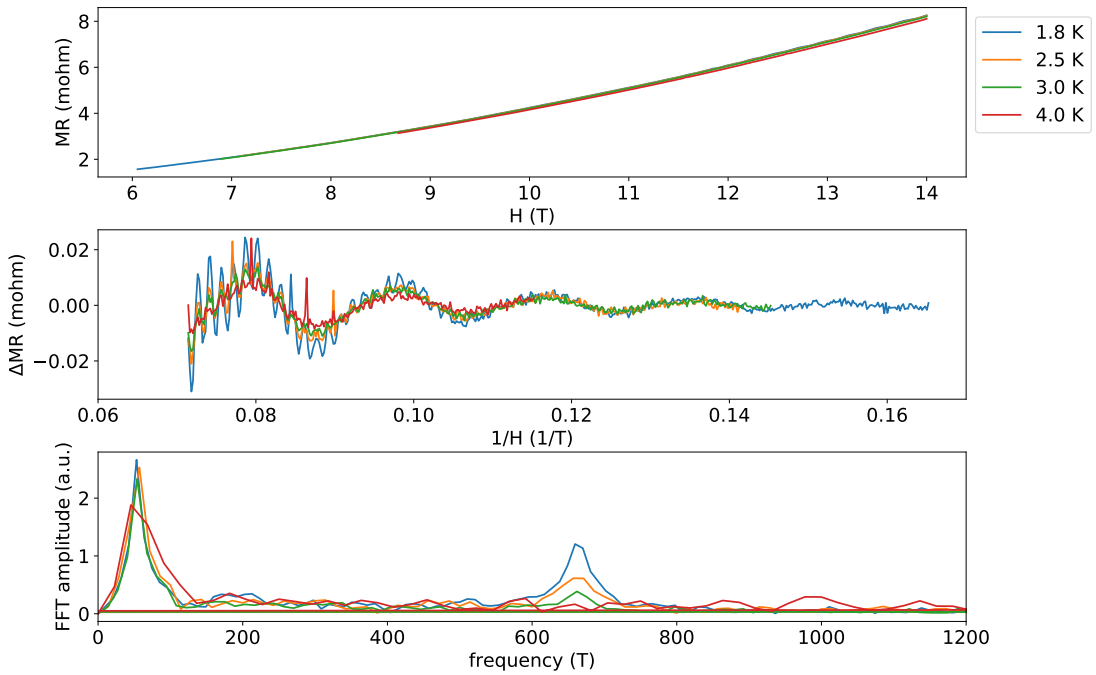


Figure A.9: (a) The longitudinal MR, (b) SdH oscillations and (c) its FFT of the bulk $MoTe_2$ sample measured at 1.6 GPa with magnetic field parallel to $c$ axis.

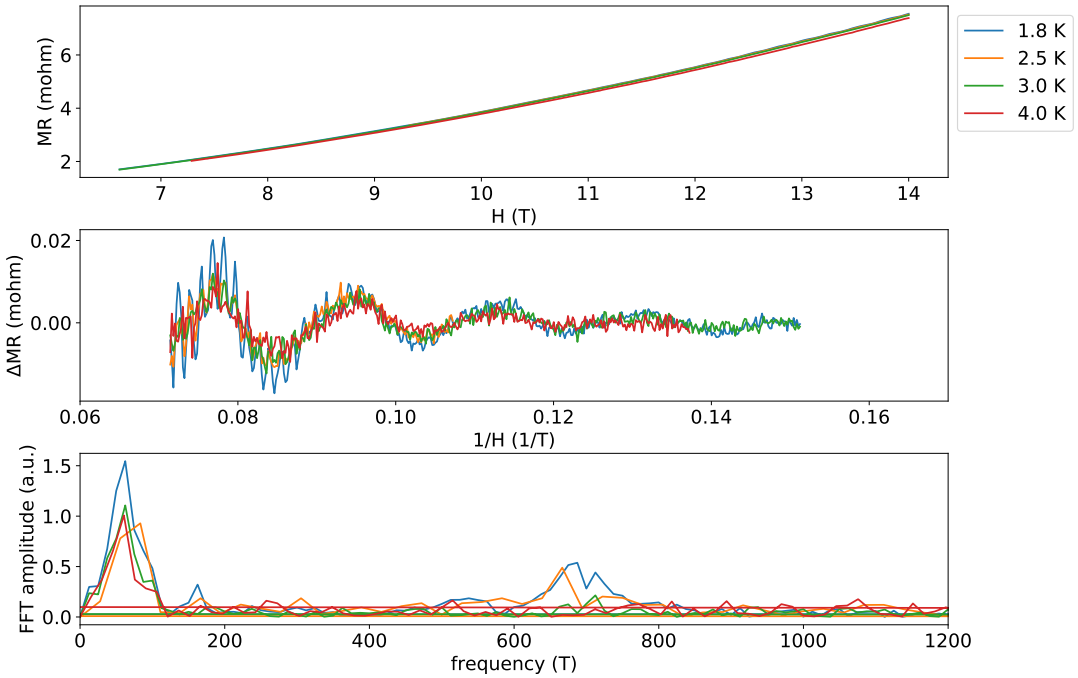


Figure A.10: (a) The longitudinal MR, (b) SdH oscillations and (c) its FFT of the bulk $MoTe_2$ sample measured at 1.8 GPa with magnetic field parallel to $c$ axis.

# Bibliography


[1] Anderson PW. *Basic Notions of Condensed Matter Physics.* Reading, Mass.: Addison Wesley (1984)

[2] M. Zahid Hasan, *et al.*, 'iscovery of Weyl Fermion Semimetals and Topological Fermi Arc States.' *Annual Review of Condensed Matter Physics* **8** (2017)

[3] Geim AK, Novoselov KS. *Nat. Mater.* 6:18391 (2007)

[4] Weyl H. *Z. Phys.* 56:330-52. (1929).

[5] Feynman, R. P., Simulating physics with computers, *Int. J. Theor. Phys.* **21**, 467 (1982)

[6] Knill, E., R. Laflamme, and W. H. Zurek, Resilient quantum computation: Error models and thresholds, *Proc. R. Soc. London*, Ser. A **454**, 365 (1998).

[7] Shor, P. W., Scheme for reducing decoherence in quantum computer memory, *Phys. Rev. A* **52**, R2493 (1995).

[8] Freedman, *et al.*, A modular functor which is universal for quantum computation, *Commun. Math. Phys.* **227**, 605 (2002).

[9] Zhang, P. *et al.*, 'Observation of topological superconductivity on the surface of an iron-based superconductor', *Science* **360**, 182186 (2018).

[10] Alexey A. Soluyanov *et al.*, 'Type-II Weyl semimetals', *Nature* **527**, 495 (2015)

[11] Takeshi Kondo, *et al.*, 'Quadratic Fermi node in a 3D strongly correlated semimetal', *Nature Communications* **6**, 10042 (2015)

[12] M. Z. Hasan and C. L. Kane, 'Colloquium: Topological insulators', *Rev. Mod. Phys.* **82**, 3045 (2010)

[13] Claudia Felser and Binghai Yan, *Nature Materials* **15** (2016)

[14] Su-Yang Xu, *et al.*, 'Discovery of a Weyl fermion semimetal and topological Fermi arcs', *Science* **349** 6248, pp. 613-617 (2015)

[15] Jian Cui, *et al.*, 'Transport evidence of asymmetric spinorbit coupling in few-layer superconducting $1T_d$-$MoTe_2$', *Nature Communication* **10** 2044 (2019)

[16] Nielsen HB, Ninomiya M. *Nucl. Phys. B*, **185**:2040 (1981).

[17] Nielsen HB, Ninomiya M., *Nucl. Phys. B*, **193**:17394 (1981).

[18] Ishikawa, J. J., *et al.*, *Phys. Rev. B* **85**, 245109 (2012).

[19] Tian, Z., *et al.*, *Nat. Phys.* **12**, 134 (2016).

[20] Nakayama, M., *et al.*, *Phys. Rev. Lett.* **117**, 056403 (2016).

[21] Nakatsuji, S., *et al.*, *Phys. Rev. Lett.* **96**, 087204 (2006).

[22] Machida, Y., *et al.*, *Nature* (London) **463**, 210. (2010)

[23] Kondo, T., *et al.*, *Nat. Commun.* **6**, 10042 (2015).

[24] Nakatsuji, S., N. Kiyohara, and T. Higo, *Nature* (London,2015) **527**, 212.

[25] Kiyohara, N., T. Tomita, and S. Nakatsuji, *Phys. Rev. Applied*, **5**, 064009 (2016).

[26] Yang, H., *et al.*, *New J. Phys.* **19**, 015008 (2017).

[27] N. P. Armitage, E. J. Mele, and Ashvin Vishwanath, 'Weyl and Dirac semimetals in three-dimensional solids', *Rev. Mod. Phys.* **90**, 015001 (2018).

[28] Xu, S.-Y., *et al.*, *Nat. Phys.* **11**, 748 (2015).

[29] Yan, B., and C. Felser, *Annu. Rev. Condens. Matter Phys.* **8**, 337 (2017).

[30] Yanpeng Qi *et al.*, Superconductivity in Weyl semimetal candidate $MoTe_2$. *Nat. Commun.* **7**, 11038 (2016).

[31] Smith, A. W., and R. W. Sears, *Phys. Rev.* **34**, 1466 (1929).

[32] Miyasato, T., *et al.*, *Phys. Rev. Lett.* **99**, 086602 (2007).

[33] Fernandez-Pacheco, *et al.*, *Phys. Rev. B*, **77**, 100403 (2008).

[34] Schad, R., *et al.*, *J. Phys.: Condens. Matter* **10**, 6643 (1998)

[35] Murakami S., *et al. New J. Phys.*, **10**, 029802 (2008).

[36] Smith T F, Chu C W and Maple M B, *Cryogenics* **9**, 53 (1969).

[37] Lorenz, B.. & Chu, C. W., *Frontiers in Superconducting Materials* (ed. Narlikar, A. V.) 459497 (Springer, Berlin, 2004).

[38] M. Garfinkel and D. E. Mapother,"Pressure Effect on Superconducting Lead", *Physical Review* **122** 2 (1961).

[39] Sun, Y., *et al.*, *Phys. Rev. B* **92**, 161107 (2015).

[40] I. Dzyaloshinskii, A thermodynamic theory of weak ferromagnetism of antiferromagnetics, *J. Phys. Chem. Solids* **4**, 241 (1958).

[41] T. Moriya, *et al.*, Anisotropic Superexchange Interaction and Weak Ferromagnetism, *Phys. Rev.* **120**, 91 (1960).

[42] Naoto Nagaosa, *et al.*, Anomalous Hall effect, *Rev. Mod. Phys.* **82**, 1539 (2010).

[43] J. H. Kang, D. S. Kim, and Q-Han Park, Local Capacitor Model for Plasmonic Electric Field Enhancement, *Phys. Rev.* **102**, 093906 (2009).

[44] A. Neubauer, *et al.*, Topological Hall Effect in the A Phase of $MnSi$, *Phys. Rev. Lett.* **102**, 186602 (2009).

[45] N. Kanazawa, *et al.*,' Large Topological Hall Effect in a Short-Period Helimagnet $MnGe$', *Phys. Rev.* **106**, 156603 (2011).

[46] N. Kanazawa,*et al.*, 'Critical phenomena of emergent magnetic monopoles in a chiral magnet', *Nature Communications* **7**, 11622 (2016).

[47] Toshiaki Tanigak,*et al.*, 'Real-space observation of short-period cubic lattice of skyrmions in $MnGe$', *Nano Lett.* **15 (8)**,54385442 (2015).

[48] A. J. P. Meyer and P. Taglang, 'Proprits magntiques, antiferromagntisme et ferromagntisme de $Au_2Mn$', *J. Phys. Radium* **17**, 457 (1956).

[49] U. Enz, 'Magnetization Process of a Helical Spin Configuration', *J. Appl. Phys.* **32**, S22 (1961).

[50] H. Samata, *et al.*, *J. Phys. Chem. Sol.* **59**, 377 (1998).

[51] T. Nagamiya, K. Nagata, and Y. Kitano, 'Magnetization Process of a Screw Spin System', *Prog. Theor. Phys.* **27**, 1253 (1962).

[52] J. K. Glasbrenner, K. M. Bussmann and I. I. Mazin, 'Magnetic spiral induced by strong correlations in $MnAu_2$', *Phys. Rev. B* **90**, 144421 (2014).

[53] J. K. Glasbrenner, 'Collapse and control of the $MnAu_2$ spin spiral state through pressure and doping', *Phys. Rev. B* **93**, 184402 (2016).

[54] Par ANDRE, *et al.*, *LE JOURNAL DE PHYSICQUE ET LE RADIUM* **22**, 337 (1961).

[55] A. Handstein *et al.*, 'Change of magnetoresistivity and magnetic structure of $MnAu_2$ by iron substitution', *Journal of Magnetism and Magnetic Materials.* **290**, 1093-1096 (2005).

[56] HERPINA. and M&IEL P., *J. Phys. Radium Paris* **22**, 337 (1961).

[57] R. C. Wayne and T. F. Smith, 'The Pressure Induced Metamagnetic Transition in $Au_2Mn$ and the Pressure Dependence of Ferromagnetic Curie Temperature', *J. Phys. Chem. Solids* **30**, 183-185 (1969).

[58] N. P. GRAZHDANKINA and K. P. RODIONOV, 'Effect of Pressure on the Magnitude of the Threshold Field and Temperature of the Antiferromagnetic Transformation of $MnAu_2$', *Soviet Phys.J.E.T.P.* **16**, 1429 (1963).

[59] T. F. Smith, C. W. Chu, and M. B. Maple, *Cyrogenics* **9**, 53 (1969).

[60] Y. Isikawa, *et al.*, 'Helical spin structure in manganese silicide $MnSi$', *Solid State Commun.*, **19**:525 (1976).

[61] Moriya T, *Solid-State Sciences* **56** (1985).

[62] Yu. A. Izyumov. 'Modulated, or long-periodic, magnetic structures of crystals', *Sov. Phys. Usp*, **27**:845 (1984).

[63] T. Suzuki *et al.*, 'Large anomalous Hall effect in a half-Heusler antiferromagnet', *Nature Physics*, **12** 11191123 (2016).

[64] Ajaya K. Nayak *et al.*, 'Large anomalous Hall effect driven by a nonvanishing Berry curvature in the noncolinear antiferromagnet $Mn_3Ge$', *Science Advances*, **2** e1501870 (2016).

[65] A. Yu. Kitaev. 'Fault-tolerant quantum computation by anyons', *Annals of Physics* **303**, 1 (2003). fault tolerant TQC

[66] Chetan Nayak, *et al.*, 'Non-Abelian anyons and topological quantum computation', *Rev. Mod. Phys.* **80**, 1083 (2008).

[67] Xiao-Liang Qi and Shou-Cheng Zhang, 'Topological insulators and superconductors', *Rev. Mod. Phys.* **83**, 1057 (2011).

[68] Xiaofeng Qian, *et al.*, 'Quantum spin Hall effect in two-dimensional transition metal dichalcogenides', *Science* **346**, 1344-1347 (2014).

[69] Shujie Tang, *et al.*, 'Quantum spin Hall state in monolayer $1T$-$WTe_2$', *Nat. Phys.* **13**, 683 (2017)

[70] Yi-Ting Hsu, *et al.*, 'Topological superconductivity in monolayer transition metal dichalcogenides' *Nat. Commun.* **8**, 14985 (2017)

[71] Li, Yanan *et al.*, 'Nontrivial superconductivity in topological MoTe2-xSx crystals', *National Academy of Sciences* **115**, 38 (2018)

[72] Ke Deng, *et al.*, 'Experimental observation of topological Fermi arcs in type-II Weyl semimetal $MoTe_2$', *Nature Phys.* **7**, 1105 (2016)

[73] Zhijun Wang, *et al.*, 'Higher-Order Topology, Monopole Nodal Lines, and the Origin of Large Fermi Arcs in Transition Metal Dichalcogenides $XTe_2$ (X=Mo,W)', Preprint at http://arxiv.org/abs/1806.11116.

[74] Huang, L. *et al.*, 'Spectroscopic evidence for type II Weyl semimetal state in $MoTe_2$', *Nat. Mater.* **15**, 1155 (2016)

[75] Jiang, J. *et al.* 'Signature of type-II Weyl semimetal phase in $MoTe_2$', *Nat. Commun.* **8**, 13973 (2017)

[76] Tay-Rong Chang, *et al.*, 'Prediction of an arc-tunable Weyl Fermion metallic state in $Mo_xW_{1-x}Te_2$', *Nat. Commun.* **7**, 10639 (2016)

[77] Sangyun Lee, *et al.*, 'Origin of extremely large magnetoresistance in the candidate type-II Weyl semimetal $MoTe_{2x}$', *Scientific Reports* **8**, 13937 (2018)

[78] Colin Heikes, *et al.*, 'Mechanical control of crystal symmetry and superconductivity in Weyl semimetal $MoTe_2$', *Phys. Rev. M.* **2**, 074202 (2018)

[79] I. A. Lukyanchuk, Y. Kopelevich, *Phys. Rev. Lett* **93**, 166402 (2004)

[80] I. A. Lukyanchuk, Y. Kopelevich, *Phys. Rev. Lett* **97**, 256801 (2006)

[81] T. Champel, V. P. Mineev, Philos. *Mag. B* **81**, 55 (2001)

[82] D. Rhodes, *et al.*, 'Bulk Fermi surface of the Weyl type-II semimetallic candidate $\gamma$-$MoTe_2$', *Phys. Rev. B* **96**, 165134 (2017)

[83] X. Luo, *et al.*, '$T_d$-$MoTe_2$: A possible topological superconductor', *Appl. Phys. Lett.* **109**, 102601 (2016)

[84] Yan Sun *et al.* 'Prediction of Weyl semimetal in orthorhombic $MoTe_2$', *Phys. Rev. B* **92**, 161107(R) (2015)

[85] M. Sato and Y. Ando, 'Topological superconductors: a review', *Rep. Prog. Phys.* **80**, 076501 (2017)

[86] Qiong Zhou, *et al.*, 'Hall effect within the colossal magnetoresistive semimetallic state of $MoTe_2$', *Phys. Rev. B.* **94**, 121101(R) (2016)

[87] H. Murakawa *et al.*, 'Detection of Berry's Phase in a Bulk Rashba Semiconductor', *Science* **342**, 1490 (2013)

[88] D. Shoenberg, 'Magnetic Oscillations in Metals', (Cambridge Univ. Press, Cambridge, 1984)

[89] L. M. Roth, P. N. Argyres, in Semiconductors and Semimetals (Academic Press, New York, 1966), vol. **1**, chap. 6, p. 159.

[90] G. Landwehr, E. I. Rashba., in Landau Level Spectroscopy: Modern Problems in Condensed Matter Sciences (North-Holland, Amsterdam, 1991), vol. **27.2**

[91] E. N. Adams, T. D. Holstein, *J. Phys. Chem. Solids* **10**, 254 (1959)

[92] Shuichi Murakami, *et al.*, 'Emergence of topological semimetals in gap closing in semiconductors without inversion symmetry', *Sci. Adv.* **3**, e1602680 (2017)

[93] Hsin Lin, *et al.*, 'Half-Heusler ternary compounds as new multifunctional experimental platforms for topological quantum phenomena', *Nat. Mater.* **9**, 546 (2010)

[94] Zaiyao Fei, *et al.*, 'Edge conduction in monolayer $WTe_2$', *Nat. Phys.* **13**, 677 (2017)

[95] Kienzle, *et al.*, (2011). Bumps (Version 0.7.10). Retrieved Jun 21, (2018)

[96] A. Crepaldi, *et al.*, 'Persistence of a surface state arc in the topologically trivial phase of $MoTe_2$', *Phys. Rev. B* **95**, 041408 (2017)

[97] P. Giannozzi, *et al.*, 'QUANTUM ESPRESSO: a modular and open-source software project for quantum simulations of materials', *J. Phys.: Condens. Matter* **21**, 395502 (2009)

[98] P. E. Blchl, *Phys. Rev. B* **50**, 17953 (1994)

[99] G. Kresse and D. Joubert, *Phys. Rev. B* **59**, 1758 (1999)

[100] J. P. Perdew, K. Burke, M. Ernzerhof, 'Generalized Gradient Approximation Made Simple', *Phys. Rev. Lett.* **77**, 3865-3868 (1996)

[101] S. Grimme, J. *Comp. Chem.* **27**, 1787 (2006)

[102] N. Xu, W. Wang, *et al.*, 'Evidence of Coulomb interaction induced Lifshitz transition and robust hybrid Weyl semimetal in $T_d$ $MoTe_2$', *Phys. Rev. Lett.* **121**, 136401 (2018)

[103] N. Aryal and E. Manousakis, 'Importance of electron correlations in understanding the photo-electron spectroscopy and the Weyl character of $MoTe_2$', *Phys. Rev. B* **99**, 035123 (2019)

[104] Ramachandran, P. and Varoquaux, G., 'Mayavi: 3D Visualization of Scientific Data' *IEEE Computing in Science & Engineering*, 13 (2), pp. 40-51 (2011)

[105] Numerical extraction of de Haas-van Alphen frequencies from calculated band energies, *Comp. Pyhs. Commun.* **183**, 324 (2012), Comp. Phys. Commun. **183**, 324 (2012)

[106] Schubnikow, L.; de Haas, W.J., 'Magnetic resistance increase in single crystals of bismuth at low temperatures' *Proceedings of the Royal Netherlands Academy of Arts and Science* (in German) 33: 130133 (1930).